INTERFERENCE AND LASER FEEDBACK OPTICAL MICROSCOPY

Nigel P Rea

Green College

A Thesis submitted for the Degree of

Doctor of Philosophy

at

The University of Oxford

Department of Engineering Science

Parks Road

Oxford

OX1 3PJ

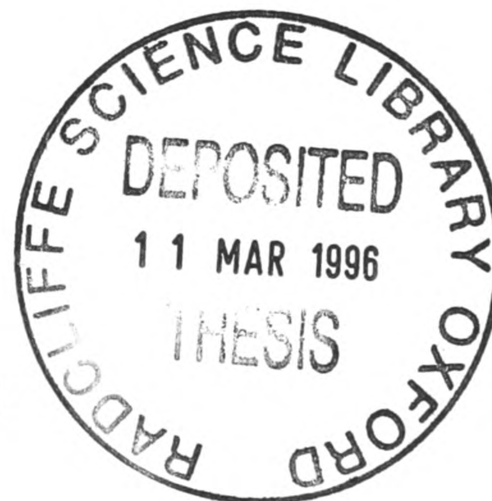

Michaelmas Term 1995

Nigel Rea
Green College
Michaelmas Term 1995

Thesis for the degree of Doctor of Philosophy
Laser Feedback and Interference Optical Microscopy

Abstract

This thesis concerns the development of simple, compact scanning optical microscopes which can obtain confocal and interference images. The effects of feeding the reflected signal back into the laser cavity of a confocal microscope are investigated and exploited. Monomode optical fibres are used to perform the spatial filtering required for confocal microscopy and, later, as the source of reference beams for interferometry.

The theory describing the basic operation of the microscopes is developed. The optical systems are modelled using scalar diffraction theory and the effects of optical feedback into the laser cavity are described, with the practical implications emphasised.

A fully reciprocal arrangement of the microscope is developed, in which a single mode optical fibre both launches the signal towards the object and then collects the reflected signal. The fibre is shown to exhibit the spatial filtering properties required for the source and detector in a confocal microscope.

It is shown that a semiconductor laser can be used as a detector of the amplitude of the object signal. This is first demonstrated by directing the microscope signal back into the laser cavity and measuring the variation of the optical intensity in the cavity itself. Comparable results are obtained when the variation of the junction voltage across the cavity is measured. It is also shown that the optical fibre is redundant in this system, since the lasing mode of the cavity itself is sufficiently small to adequately spatially filter the reflected signal.

When a Helium–Neon laser is used as the source of illumination the effect of the feedback on the laser is seen to be very different, resulting in interferometry. It is shown that high frequency modulation techniques can be used to obtain both confocal images and surface profiles from the same system. This is first demonstrated using an optical feedback scheme in which the modulation of the optical path length of the object beam is controlled electro–optically. In an alternative scheme the images are obtained by calculation, rather than by using a control loop system. In this case the modulation is achieved mechanically.

The theoretical limits for the resolutions of the systems described are discussed. It is shown that the lateral resolution of the surface profile systems is inherently non–linear with feature height.

Finally, a semiconductor laser based microscope is developed which can obtain confocal images and surface profiles independently. The dependence of the wavelength on the injection current is exploited as a convenient means of introducing a phase shift into the feedback signal by which profilometry can be achieved.

All the systems are described theoretically and demonstrated experimentally.

Now we see but a poor reflection; then we shall see face to face.
Now I know in part; then I shall know fully, even as I am fully known.

1 Corinthians 13 : 12

To my Father and Mother

Acknowledgments

It is my great pleasure to thank my supervisor, Dr Tony Wilson, for his consistent encouragement and invaluable direction throughout my research. It is primarily due to his patient guidance that this research has been completed at all. I also particularly wish to thank Dr Rimas Juškaitis for his guidance and forebearance thoughout this time. His helpful advice and assistance were greatly appreciated.

In addition, my thanks go to Dr Douglas Hamilton for his immense contribution to the design and implementation of the electronic circuits shown in Appendices 3 and 4. Without him they would never have worked. I also gratefully acknowledge the assistance with the computers rendered by Dr Mark Neil and Mr Grahame Faulkner.

My time as a research student has been made much more pleasurable by the friendships I have enjoyed, particularly with Boon Tan and Diana Ulrich. I am also very grateful for the many stimulating conversations I have enjoyed with Dr Steve Elston and Mr Mike Cherrill.

Finally, my thanks extend to the others in the lab who made my time so rewarding.

Contents

1. Introduction 1

1.1 A Brief History of Optical Microscopy 1

1.2 The Development of the Scanning Optical Microscope 4

1.3 Introduction to the Confocal Scanning Optical Microscope 5

1.4 Detection Schemes 9

1.5 Experimental Arrangement 11

1.5.1 General Layout 11

1.5.2 The Scanning Mechanism 12

1.6 Summary of Research in this Thesis 13

2. Optical Theory for a Confocal Scanning Microscope 15

2.1 Introduction 15

2.2 Imaging by a Lens 15

2.3 The Effect of Defocus 18

2.4 Imaging by the CSOM Optical System 20

2.5 The Effect of Finite Area Detectors 21

2.5.1 Axial Responses 22

2.5.1 .1 Pinhole Detectors 23

2.5.1 .2 Small Finite Area Detectors 23

2.6 Spatial Frequencies 25

3. Laser Theory for Optical Feedback 28

3.1 Introduction 28

3.2 Reflectivity Model of the Compound Laser Cavity 29

3.3 Dynamical Laser Theory 32

3.3.1 Theoretical Basis 32

3.3.2 Phase Variation and Introduction of Parameter C 35

3.3.3 The Physical Meaning of C 36

3.3.4 The Experimental Significance of C 37

3.3.5 The Effect of Varying the External Cavity Length 38

3.3.5.1 Frequency Variation 38

3.3.5.2 Intensity Variation 41

3.4 Conclusions 43

4. Laser Feedback: Optical Intensity Variation 44

4.1 Introduction 44

4.2 Simplified Semiconductor Laser Theory 45

4.2.1 Introduction to Simplified Feedback Theory 45

4.2.2 Laser Intensity 45

4.2.3 Predictions from the Model 48

4.3 Experimental Results for the Semiconductor Laser Microscope 52

4.3.1 Characteristics of the Laser with Feedback 52

4.3.2 The Response of the Microscope 54

4.3.3 Noise Characteristics 55

4.3.4 Imaging Capability 58

4.4 Conclusions 59

5. Laser Feedback: Junction Voltage Variation 60

5.1 Introduction 60

5.2 The Optical System 61

5.3 Theory 62

5.3.1 Laser power 62

5.3.2 Specimen Reflectivity 64

5.3.3 Junction voltage 66

5.4 Experimental Results 68

5.4.1 Semiconductor Laser Characteristics 68

5.4.2 Optical Characteristics 71

5.5 Conclusions 72

6. Profilometry using Laser Feedback 73

6.1 Introduction 73

6.2 Simplified HeNe Laser Theory 74

6.3 Introduction to Profilometry 79

6.4 Profilometry Theory 80

6.5 Experimental Technique and Results 81

6.5.1 Experimental Arrangement 81

6.5.2 Experimental Approaches 83

6.5.2.1 Interferometry 83

6.5.2.2 Direct Feedback Profilometry 83

6.5.2.3 Lock–In Profilometry 83

6.5.3 Preliminary Results 85

6.5.4 Images ... 87
6.5.5 Noise Considerations ... 91
6.6 Conclusions ... 92

7. Profilometry by Calculation ... 93

7.1 Introduction ... 93
7.2 Theory ... 93
7.2.1 Theoretical Basis ... 93
7.2.2 Theoretical Results ... 97
7.3 Experimental Technique and Results ... 100
7.3.1 Arrangement ... 100
7.3.2 Microscope Characteristics ... 101
7.3.3 Images ... 104
7.4 Conclusions ... 107

8. Spatial Resolution ... 108

8.1 Introduction ... 108
8.2 Depth Resolution ... 108
8.3 Confocal Lateral Resolution ... 109
8.4 Lateral Resolution for Profilometry ... 110
8.4.1 The Basic Theory ... 111
8.4.2 Experimental Conclusions ... 113
8.5 The Limit of Lateral Resolution ... 114
8.6 The Effect of Numerical Aperture ... 117
8.7 Conclusions ... 120

9. Semiconductor Laser Confocal and Interference Microscopy ... 121

9.1 Introduction ... 121
9.2 Theoretical Basis ... 122
9.3 Experimental Technique and Results ... 127
9.3.1 Experimental Details ... 127
9.3.2 Confocal Imaging ... 127
9.3.3 Surface Profilometry ... 130
9.4 Conclusions ... 134

10. Conclusions and Suggested Further Research **135**

Appendix 1 Introduction to Fresnel Diffraction **141**

Appendix 2 The Modelling of Lenses **144**

Appendix 3 Differential Amplifier with Offset **146**

Appendix 4 High Frequency Lock–In Amplifier **147**

References **149**

Publications Resulting From This Research **154**

1. Introduction

1.1 A Brief History of Optical Microscopy

The use of optical technology can be traced far into antiquity. Mirrors are mentioned four times in the Bible, of which the first reference is to their recycling by the Israelites in Exodus 38:8 (c 1200BC). Among the writers of classical antiquity there are a number of references to "burning glasses" [1], the earliest of which is in the comic play *The Clouds* by Aristophanes. In some cases this seems to refer to a solid crystal and in others to a glass globe full of water. The clearest reference to their magnifying power is given by Seneca who wrote around AD63

> 'Letters, however small and dim, are comparatively large and distinct when seen through a glass globe filled with water'

Others, such as Cleomedes (in his *Cyclical Theory of Meteors* which includes a crude study of refraction) and Hero of Alexandra (who showed in his *Catoptrika* and his *Dioptra* that light is reflected from a surface at an angle equal to the angle of incidence) developed some basic concepts in geometrical optics. Despite this, however, the ancients display no definite evidence of knowledge of lenses apart perhaps from the lens of the eye. But even had lenses been known they could hardly have been properly understood. This is because of the prevalent view of vision at the time, popularized by Plato, that regarded it as something emanating from the eye.

For the first hint of a real appreciation of the action of a lens we have to wait until the Arabian scholar Ibn al Haitham (Alhazen) from Basra, who lived 962–1038. His work was based on that of the Greeks but, significantly, he considered that vision resulted from rays coming to the eye from the object, and opposed the Greek view of vision involving emanations from the eye. He clearly predicts that in a simple optical arrangement, which he de-

scribes, the image will definitely be larger than the object itself. However he does not discuss any practical applications of his observation.

Roger Bacon (1215–1294) made significant advances in the knowledge of optics and is distinguished from his predecessors by his clear appreciation of the value of experiment. There is evidence in his works that he made a serious and continuous effort to discover the laws of refraction and reflection and that he sought to apply this knowledge to the improvement of the power of vision. In this sense he has a valid claim to the title of the "Father of Microscopy". Though there is no evidence that he made any but simple microscopes, he did advance the understanding of lenses and suggest their use in aiding vision.

The first practical breakthrough in optics is now attributed to a glass–worker of Pisa around 1286 [2] who is credited with having invented the first eye–glasses. The oldest extant record mentioning spectacles is a series of regulations of the Venetian guild of workers in rock crystal and glass in 1300. This development coincided with the height of Venice's greatest economic prosperity. For a literate trading power it was clearly valuable to be able to retain the services of a skilled book–keeper whose eyesight was deteriorating.

Perhaps surprisingly, it was a further 300 years before the compound microscope was invented. The actual combination of lenses in the form of a microscope is first attributed to Giovanni Battista Della Porta (1540–1615) in the 1588 edition of his *Magia Naturalis.* However there is no real evidence that he recognised any effective practical application of his idea. It is extremely difficult to identify when and where the first working microscope was built but credit for it is usually given to Zacharias Janssen (born 1580) and his father Hans, who were spectacle makers in Middelburg, Holland. Their first microscope is considered to have been made some time between 1591 and 1608. Perhaps significantly, Middelburg (the capital of Zeeland) was going through a period of rapid expansion at this time!

Galileo Galilei (1564–1642) was the first to popularize the new microscope. He first heard a rumour about it from Holland in 1609 and quickly built his own, grinding the lenses him-

self by hand. It was Kepler (1571–1630) who gave the first satisfactory theoretical analysis of the operation of a microscope in his "*Dioptrice*" of 1611.

Though initially called an "occiale", the new instrument 'for viewing minute objects' was first given the name "microscope" in 1625.

Throughout the 17th century there were major drawbacks to the use of a compound microscope, primarily because of the poor quality of the lenses then available. The main problems were chromatic aberration, spherical aberration and the poor quality of the glass. Indeed, so serious were these problems, that simple, single–lens microscopes could often achieve better results. It was not until the 19th century that these problems were satisfactorily overcome and as a result the simple and compound microscopes developed along separate paths, and throughout the 18th century the simple microscope was much the more popular amongst scientists. During this time however there was continual development in the design and quality of construction of microscopes, for example in their illumination and adjustment mechanisms.

Progress with the development of improved lenses was delayed until the beginning of the 19th century because it was not until then that furnaces of sufficiently high temperatures became available to produce high quality optical glass. Shortly thereafter the first achromatic lens became available commercially, which was soon to be followed by correction for spherical aberration. As a result, the performance of the compound microscope improved markedly and throughout the 19th century it was the focus of the main developments in microscopy.

However it was not until the 1870s that the modern theory behind the formation of the image in a microscope was eventually formulated by Ernst Abbe (1840–1905). Abbe was formerly a lecturer at the University of Jena, but in 1866 he accepted an invitation to join the microscope manufacturer, Carl Zeiss (1816–1888), to establish a more scientific approach to microscope design. This new theoretical understanding soon led to the development of

the apochromatic lens and oil immersion techniques. Towards the end of the 19th century the optics of the light microscope reached a peak of quality. Since then the major developments have been in imaging techniques and other forms of microscopy, such as phase contrast microscopy (during the Second World War) and interference microscopy which was first developed into a practical system by F H Smith in 1947.

1.2 The Development of the Scanning Optical Microscope

The first scanning optical microscope of which we have record was reported in 1951 by Young and Roberts [3]. They scanned a finely focussed spot of UV light (from the face of a flying spot scanner tube) in a raster pattern over a specimen and measured the transmitted intensity. The resulting electrical signal was amplified and displayed on a VDU screen which was scanned in synchrony with the "flying spot". Although this system could produce adequate images of thin biological specimens, the brightness of the light source limited its ability to be used in a reflection system or with moderately absorbing or reflecting specimens. Also such a system was limited to a relatively small band of wavelengths (UV) which could be used for illumination.

In the following years a variety of other scanning microscope configurations were proposed. Deeley, for example, used a conventional microscope but scanned a small aperture across the image plane and used a photomultiplier to detect the intensity of each point [4].

It was not until 1957, however, that what is now called the confocal scanning microscope was first described. Marvin Minsky applied for a patent [5] for a scanning microscope which used a stage–scanning confocal optical system, and a Zirconium arc for illumination. He was the first to describe its superior image formation properties and its ability to perform optical sectioning.

The problems mentioned earlier regarding illumination brightness and the limited range of available wavelengths were not overcome until the invention of the laser in 1960. The laser

was the direct descendant of the maser (a low–noise microwave amplifier) which was developed during the 1950s. In 1958 Schawlow and Townes derived the conditions required for light to be amplified [6] using the same quantum mechanical interaction of matter and radiant energy and in July 1960 Maiman announced the first operational laser, as it became known. Within a few years a wide variety of lasers were developed including the Helium–Neon laser in 1961 and the semiconductor laser in 1962. At last a suitable light source was available, which was sufficiently intense, collimated and monochromatic to enable acceptable imaging to be possible in scanning optical microscopes.

Since then lasers have become the standard (though not exclusive) source of illumination for confocal scanning microscopes. The imaging capabilities of the microscopes have also been significantly improved with the advent of low cost high–speed digital computers with image processing capabilities. Finally, confocal scanning optical microscopes first became commercially available in 1987.

We look now at the significant features of these microscopes and introduce the form of the microscope which forms the basis of the research in this thesis, including a brief overview of the practical details of the system used for the experimental work. We finish this chapter with a summary of the contents of this thesis.

1.3 Introduction to the Confocal Scanning Optical Microscope

In a conventional microscope all points of the object within the field of view are imaged simultaneously to produce the image. This requires extended illumination and an extended detector, and more problematically, uniform imaging properties across the whole field of view of the lens system being employed. These problems are eased if the lens system has to image only a single point on the specimen at any one time. To increase the field of view it is simply necessary to scan the point of observation across the desired area: this is the basis of a scanning microscope.

We limit the field of view, to image one point at a time, either by placing a small aperture in front of the object or, more feasibly for visible frequencies, using a point detector focussed onto a diffraction limited spot on the object while focussing the illumination from a point–like source (usually a laser) onto the same spot. To achieve this optically an objective lens is used to focus the light onto the object and a collector lens is used to refocus the transmitted or reflected light onto a detector. If both the source and detector are point–like and both lenses are focused on the same point of the object this arrangement is known as *confocal.* This is shown schematically in Fig. 1.

Such a confocal scanning system is capable of achieving a higher resolution than is otherwise possible using a conventional system. This is explained by a principle described by Lukosz [7]. He states that the resolution of an imaging system may be improved at the expense of the field of view.

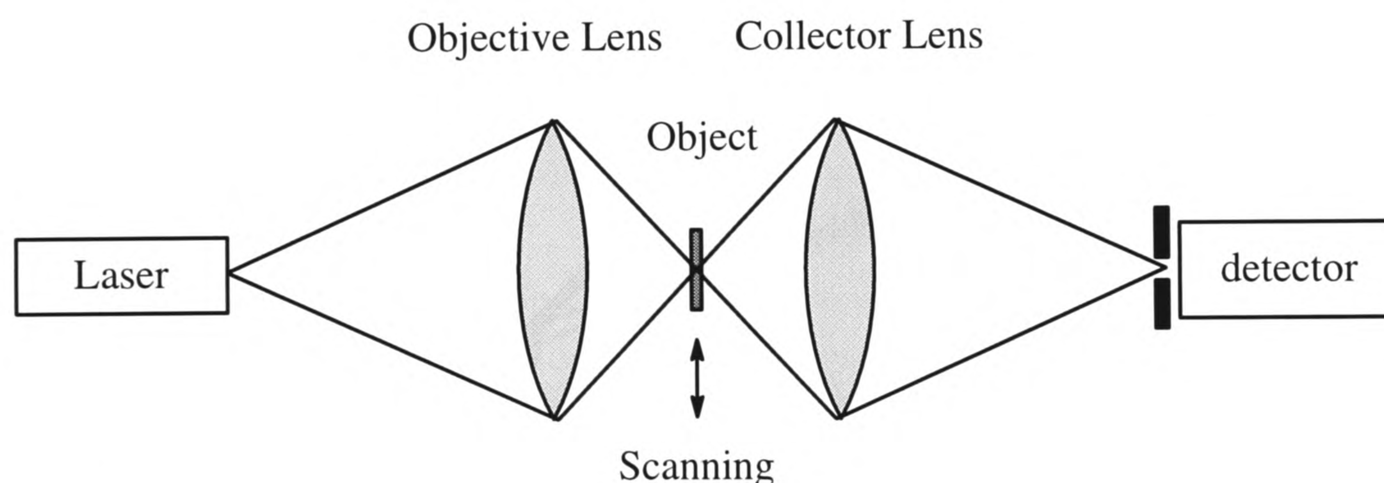

Fig. 1 Schematic diagram of the optics of a transmission Confocal Scanning Optical Microscope (CSOM).

It is also possible to have a reflection scheme in which the same lens acts as both the objective lens and the collector lens, and a beam splitter is used to direct some of the reflected signal towards a detector which measures the reflected intensity from the spot on the object being 'observed', as shown in Fig. 2. The object is then scanned and the intensity of the detected signal corresponding to each point on the object is displayed on a monitor. It is then possible to achieve 3d–imaging by combining 2d images taken at different axial positions of the object.

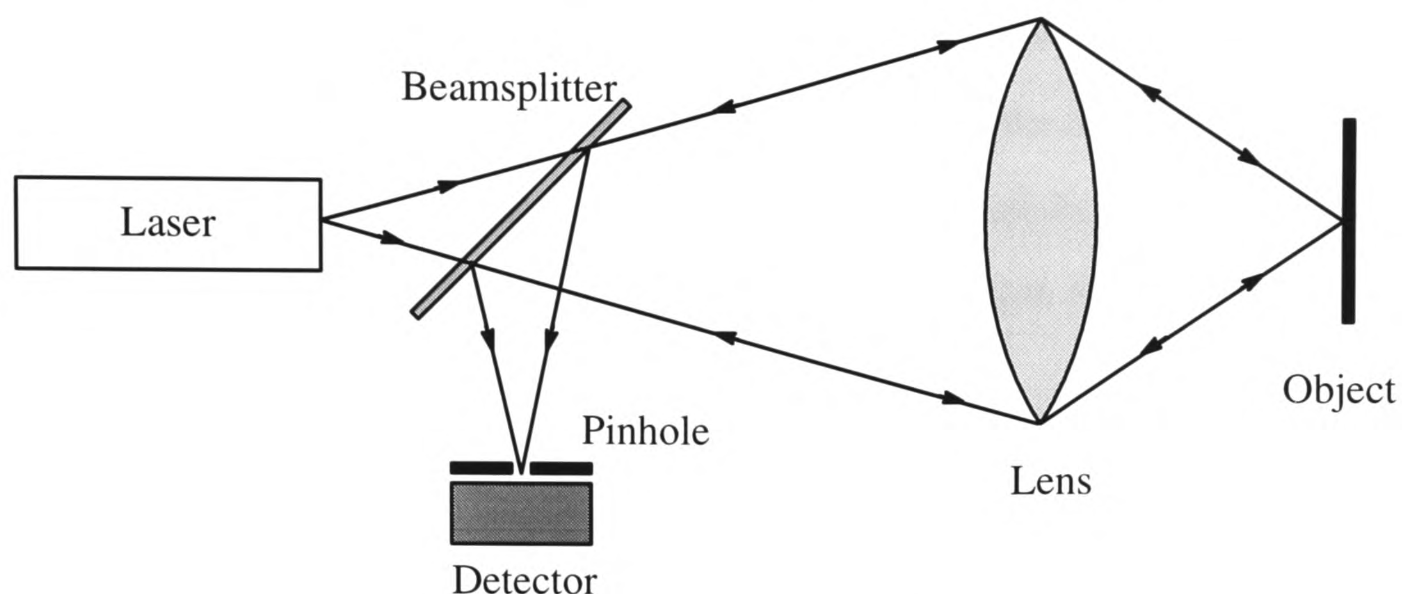

Fig. 2 A schematic diagram of the optics of a basic SOM in reflection mode.

If either an extended detector or extended source is used (in either the transmission or reflection scheme) the resulting imaging properties are the same as those for conventional microscopy. However, as well as reducing the achievable resolution, such a system also sacrifices an important property of the confocal microscope known as optical sectioning, or depth discrimination. [8,9]

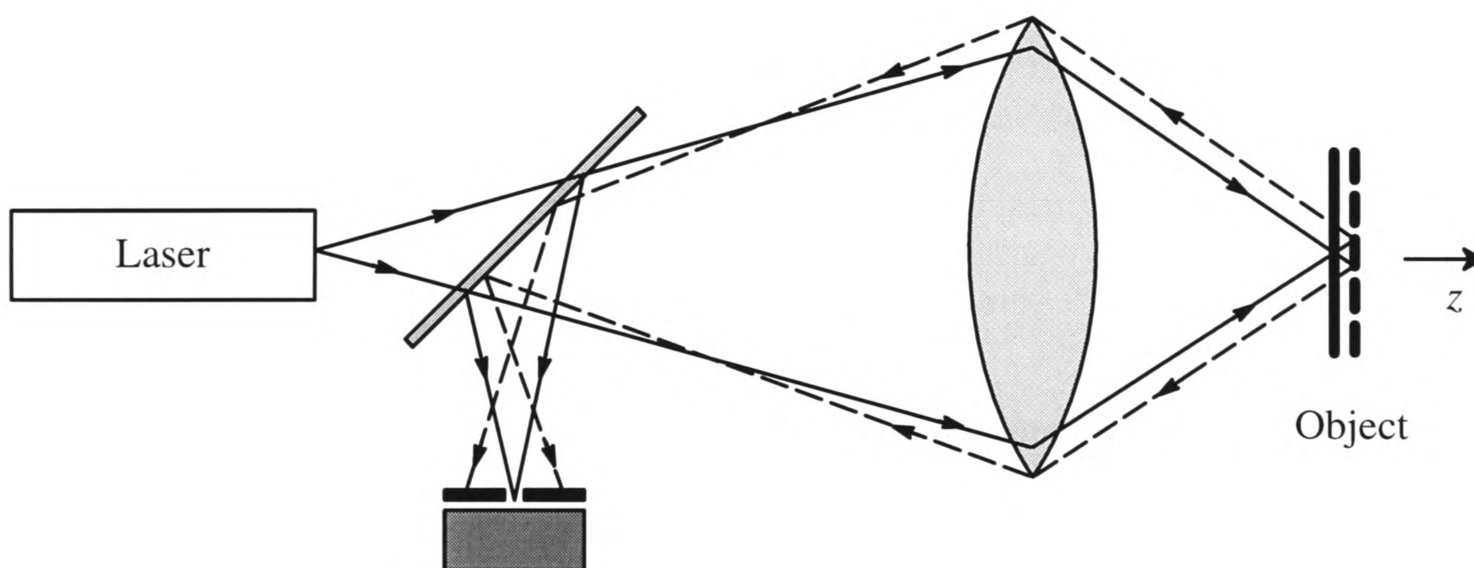

Fig. 3 Illustration of depth discrimination in the confocal microscope.

This property stems directly from the confocal arrangement of the lenses, in which a point source is focussed onto a diffraction limited point on the specimen and this same point is focussed onto a point detector. Clearly, as illustrated in Fig. 3, if this point on the object is moved out of focus the light reflected back to the detector is a defocussed patch and there is a dramatic reduction in the measured intensity. In this way the confocal arrangement great-

ly attenuates features which are not in or very near the focal plane of the objective lens. To demonstrate this property a plane mirror can be scanned along the optical axis, through the focal plane. The variation in intensity resulting from such axial displacement is shown in Fig. 4. A typical value for the full width half maximum is 2μm for an objective lens of numerical aperture 0.5 and a laser wavelength of 633nm.

This confocal arrangement also has the beneficial effect of reducing the deterioration of image quality resulting from stray light in the system due to multiple reflections of the illumination at any of the optical components in the microscope. As we have seen, any of the illumination which is scattered and then reflected back to the detector is discriminated against, and this results in improved image contrast.

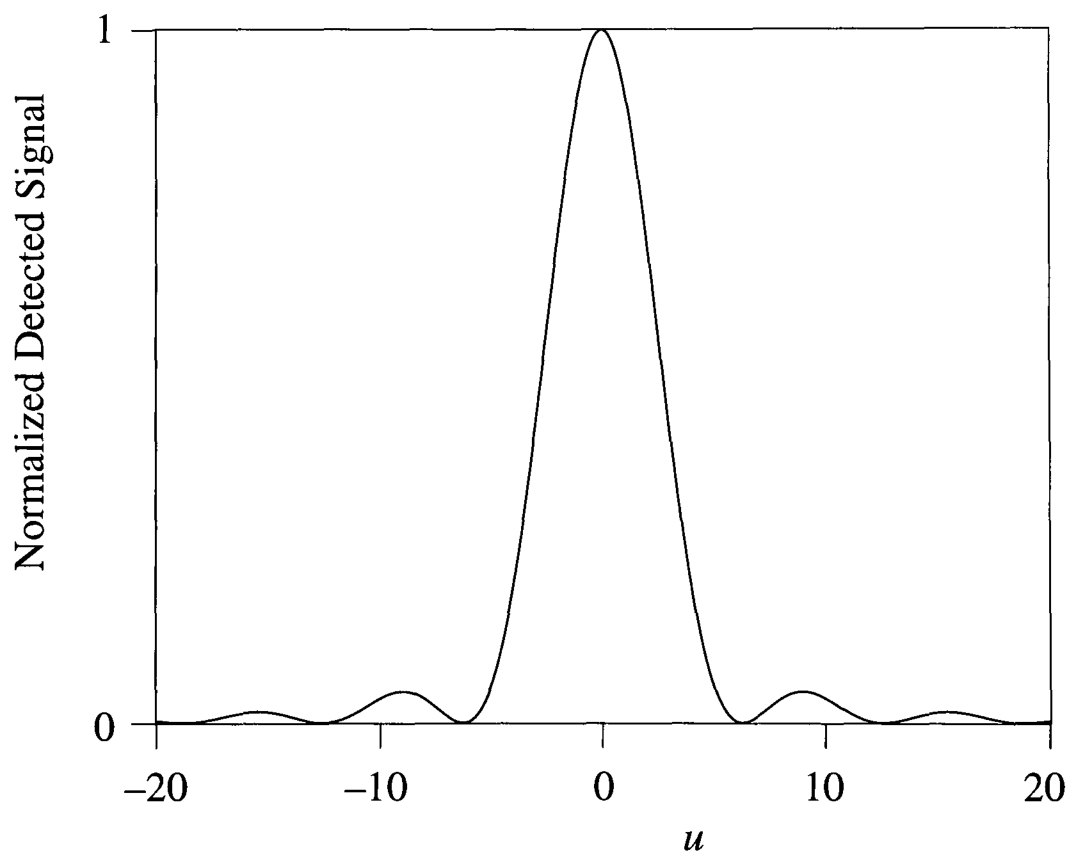

Fig. 4 The variation of detected intensity with axial displacement of the object for a confocal microscope. The Optical Unit, u, is defined as $4\,k\,z\,\sin^2(\alpha/2)$, where $k = 2\pi/\lambda$, z is the axial displacement in microns and $\sin\alpha$ is the numerical aperture of the objective lens.

Finally, one other significant property of the CSOM comes from its serial imaging nature and the fact that the image is obtained in an electrical form. As a result this microscope is particularly suitable for electronic image processing and enhancement. This means that the data can be analysed directly.

Throughout the rest of this thesis we shall only consider the reflection scheme of the microscope.

1.4 Detection Schemes

Light detectors, such as photodiodes, can, by their nature, only measure the intensity of incident light, and this is referred to as *Incoherent* Detection. Mathematically this is described by the integral of the square of the signal amplitude incident on the detector, U (which may vary for each point on the specimen (x_s, y_s)), and the detector sensitivity, D. The integral, which is shown in eqn (1), is over the area of the detector, $\mathcal{S}$, and U and D may vary across $\mathcal{S}$.

$$I(x_s, y_s) = \int_{\mathcal{S}} |U(x_s, y_s)|^2 \; D \; \mathrm{d}\mathcal{S} \tag{1}$$

From this it can be seen that only if the pinhole in front of the photo–detector is infinitesimal, thus making D effectively a Dirac delta function, do we obtain the coherent result $I(x_s, y_s) = |U(x_s, y_s)|^2$.

It is however possible to detect simply U rather than $|U|^2$ by using a monomode optical fibre, and thus ensure that the imaging is always *Coherent*. The signal which is then emitted from the fibre and fed onto the photo–detector, is then the square of the overlap integral of U and the eigenmode of the fibre, e, as shown by eqn (2).

$$I(x_s, y_s) = \left| \int_{\mathcal{T}} U(x_s, y_s) \; e \; \mathrm{d}\mathcal{T} \right|^2 \tag{2}$$

For either of these systems to produce acceptable images it is important that a given point on the object is focussed by the lens system onto the point source of the illumination and simultaneously onto the point detector. This is what gives the system its remarkable depth discrimination. However it also imposes a tight restriction on any possible misalignment of the

optical system. In practice, to achieve successful imaging, the required alignment accuracy of the laser and photo–detector pinhole relative to the lens system and object is of the order of a micron.

With an optical fibre we can, however, greatly simplify the problem of positioning the detector if we use a reciprocal geometry scheme. In this case the point source and point detector are automatically at the same point in space and therefore, of necessity, both focussed onto the same point on the specimen. As a result we gain considerable lateral freedom in positioning the source/detector. This can be achieved by using a single mode fibre between the laser and the lens as shown in Fig. 5 [10,11,12]. The fact that the detector is now an end of an optical fibre removes the need to use a pinhole in front of the photo–detector, since all that is necessary is that a constant proportion of the light detected by the fibre enters the photo–detector. Clearly this makes positioning the photo–detector relatively trivial.

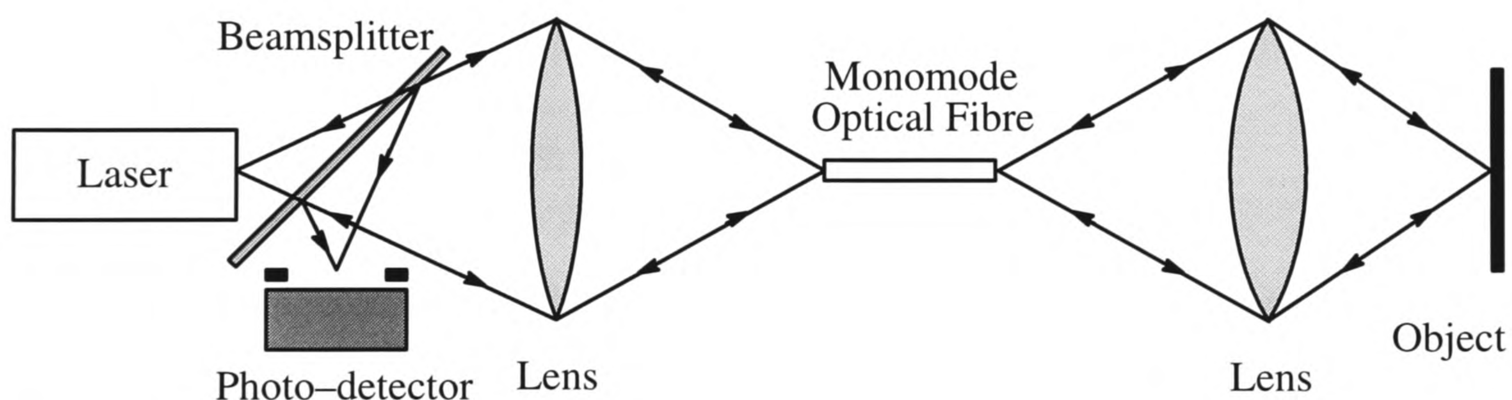

Fig. 5 CSOM with Optical Fibre Detection.

As a further simplification we can remove the need for a beam splitter by allowing the light to pass back through the laser [13]. The optical intensity emitted from the back of the laser (as shown in Fig. 6) is measured by a photo–detector, which detects the microscope signal as modulation of the continuous laser beam. This is the starting point of the research in Chapter 4. However, before we can consider this scheme in detail, it is necessary to consider further the theory governing imaging in confocal microscopes. This is discussed in Chapter 2.

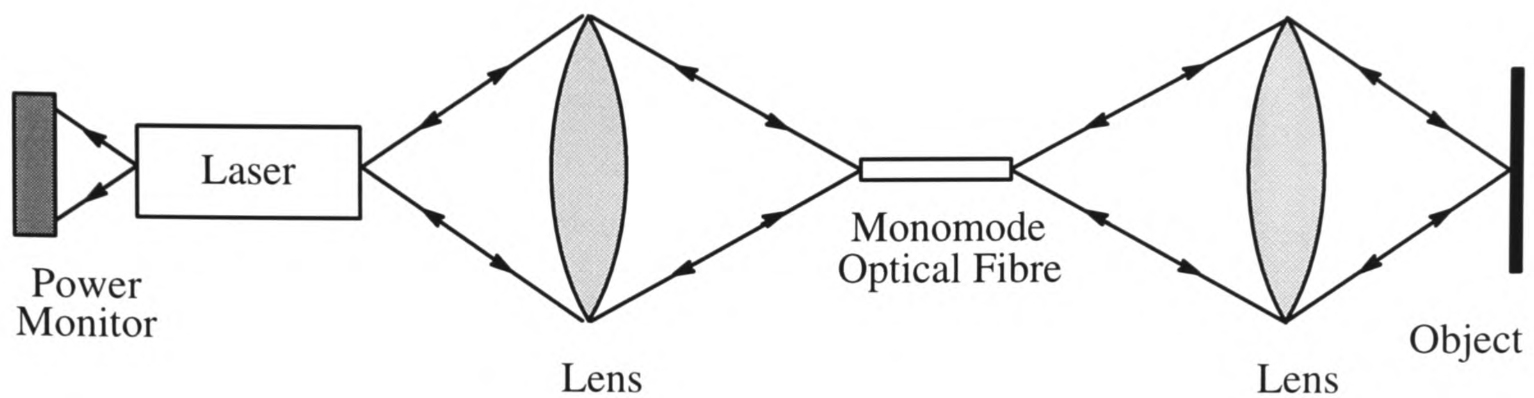

Fig. 6 A fully reciprocal geometry scheme for a reflection CSOM.

1.5 Experimental Arrangement

1.5.1 General Layout

Though we use a number of different experimental systems in the course of the research described in this thesis, there are a number of common aspects to these systems and how they are controlled. These common aspects are described in this section.

The usual control scheme which was used is illustrated in Fig. 7.

The control computer received the image signal for a point on the object and synchronised the image position with the object position, which was dictated by the scanning system. The images were displayed on a colour monitor and each was 256x256 pixels in size and had an eight–bit dynamic range. The scanning rate on the display monitor was 70Hz line scan and around 0.28Hz frame scan.

The optical system consisted of a laser which was used to illuminate the object, a lens system, often an optical fibre, and a scanning stage which held the specimen to be imaged. This was all mounted on an anti–vibration isolation table. The details of the lasers, optical fibres and the lenses used are given in the descriptions of the particular experiments.

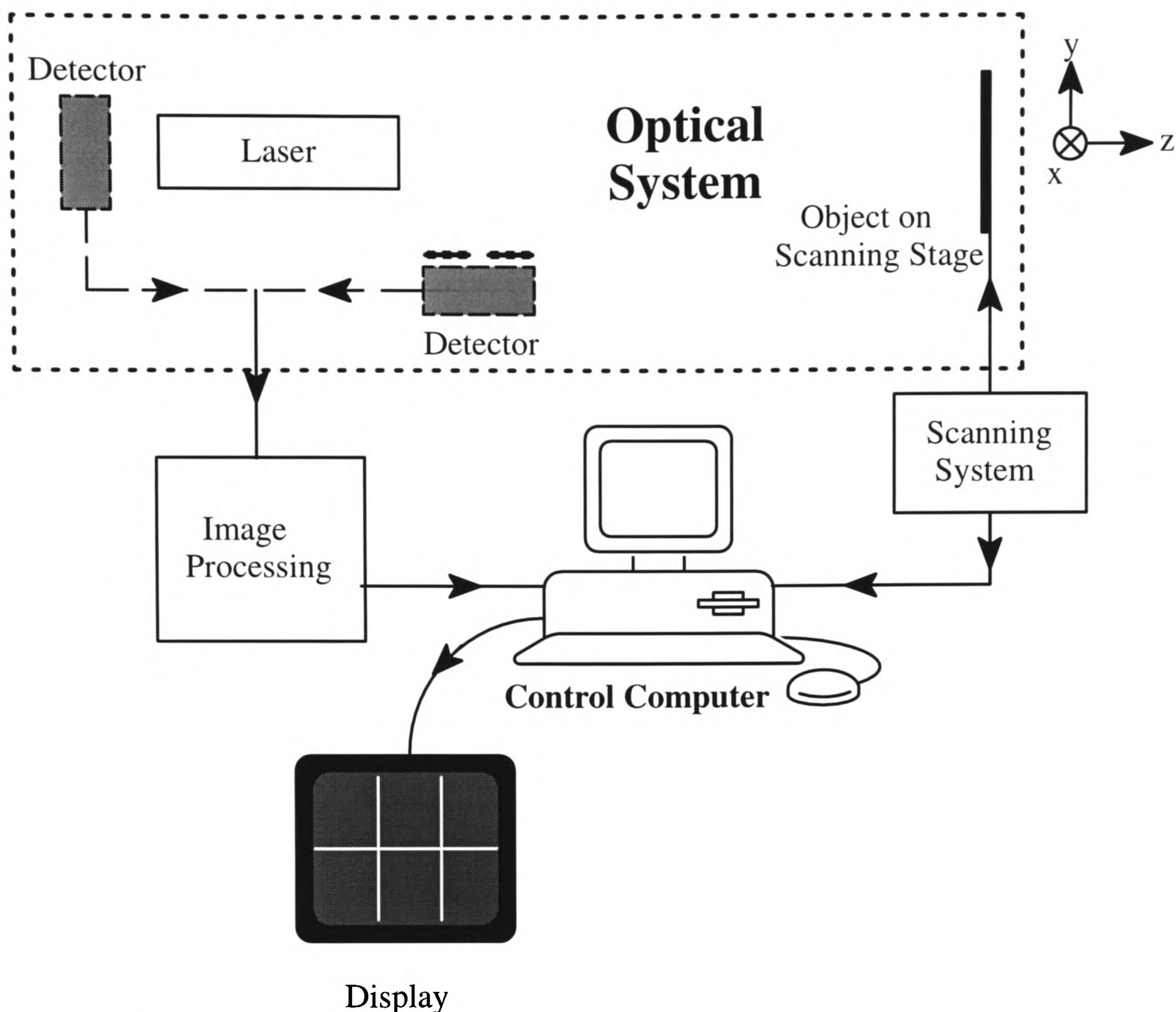

Fig. 7 A schematic diagram of the control scheme used for the microscope.

1.5.2 The Scanning Mechanism

Since the specimen is imaged point by point there needs to be some mechanism whereby a series of these point images are obtained over the area of interest, and this requires some means of lateral scanning. There are two approaches: on–axis object scanning (in which the object is mechanically scanned across a stationary focussed beam) and off–axis beam scanning (in which a focussed beam is scanned across the surface of a stationary object).

Historically, the first mechanism used was beam scanning. There are various techniques which may achieve this, including the use of acousto–optical beam deflectors and scanning mirrors mounted on resonant galvanometers. Indeed both these techniques are used in commercially available video–rate confocal microscopes. This highlights the main strength of the beam scanning technique, namely its ability to scan at high speed. However

this is achieved at the cost of a significantly more complex optical system since it is necessary to compensate for off–axis aberration. As a result such systems are only used when modest resolutions are required.

The scanning mechanism used for the research in this thesis was mechanical on–axis object scanning. This technique relaxes the aberration requirements for the lens system since it is now only necessary to produce a constant, focussed spot at the surface of the object. It also ensures that the imaging is spatially invariant, ie the resolution and contrast are constant across the entire field of view. In addition, the resolution and contrast are decoupled from the magnification, unlike with the beam scanning technique. To change the magnification it is only necessary to change the amplitude of the scan of the object. Mechanical scanning also greatly simplifies interference scanning microscopy, removing the need for matched optics. This is significant for the later research in this thesis. For this research, the lateral scanning was achieved by orthogonal electro–mechanical vibrators, mounted on a fixed frame, which scanned a specimen stage. The stage was stabilised to a neutral position by three metal piano wires of adjustable tension.

To achieve axial scanning, which is necessary for the acquisition of through focus scans, a separate piezo–electric translator was used.

1.6 Summary of Research in this Thesis

Chapter 2 provides a brief overview of the optical theory required to provide mathematical descriptions for the experimental results obtained in this thesis while Chapter 3 provides an account of how lasers behave when coupled to an external cavity. The significant differences in behaviour between HeNe lasers and semiconductor lasers are highlighted and accounted for.

In Chapter 4 we begin by considering a novel form of confocal microscope in which a laser is used both to illuminate a specimen and to detect the signal reflected from it. We used a

single–mode optical fibre as a reciprocal spatial filter which ensures confocal operation. We consider HeNe and semiconductor laser versions of the microscope and their imaging properties both theoretically and experimentally.

In the system shown in Fig. 6 the fibre is used as a common source and confocal detector before the signal is fed back into the laser. However the laser itself can act as its own confocal detector [14] which, as we shall see, makes it possible to dispense with the fibre altogether. This is the starting point for Chapter 5 (Fig. 28). There we go on to consider the semiconductor laser in more detail and show that it is also possible to dispense with the power monitor altogether if the signal is taken as a modulation of the potential difference across the semiconductor material. We shall see that it can perform all the functions of a confocal scanning microscope, including optical sectioning, height detection and extended focus.

Next we consider the effect of optical feedback into a laser with a longer coherence length and high reflectivity mirrors and show that it behaves as a confocal interference microscope. To exploit this for imaging small features on a fairly flat surface we use an electro–optic feedback technique in Chapter 6 and a non–feedback technique in Chapter 7. In the latter case we once again use an optical fibre, but this time it serves as the source of the reference beam as well as the detector, and in this way enables near–common path interferometry to be achieved. In Chapter 9 we use this same interferometry system but this time with a semiconductor laser. This enables us to achieve real–time profilometry while using a non–mechanical feedback system, in which we take advantage of the dependence of the laser wavelength on junction current. Using these profilometry techniques we show that it is possible to achieve axial resolutions of the order of nm and demonstrate this experimentally.

In Chapter 8 we provide an account of the spatial resolution achievable by the profilometry systems discussed in Chapters 6, 7 and 9. It is seen that this is non–linear and, indeed, varies with the feature height being imaged.

2. Optical Theory for a Confocal Scanning Microscope

2.1 Introduction

In this chapter we outline the optical theory required in the rest of this thesis. We demonstrate how various of the optical properties of a confocal scanning optical microscope are modelled. First we describe how the action of a lens is modelled by introducing the concept of a point spread function. We show how this is modified to account for objects which are slightly axially displaced from the focus of the lens. With these results we describe the imaging of a confocal microscope and show how this is modified when the optical sources and detectors cannot adequately be described as pinholes. Finally we show how spatial frequencies can be used to introduce the concept of the transfer function of an optical system. This enables us to describe the imaging properties of the system independently of the object being imaged.

2.2 Imaging by a Lens

Before developing mathematically the basic theory behind the operation of a CSOM we need to understand how to model the action of a lens, and this requires Fresnel diffraction theory and the paraxial model of the lens, outlined in Appendices 1 and 2. We require a description of how an incident beam, of amplitude $U_o(x_o,y_o)$, distance d_1 in front of the lens, is imaged onto a plane, distance d_2 behind the lens.

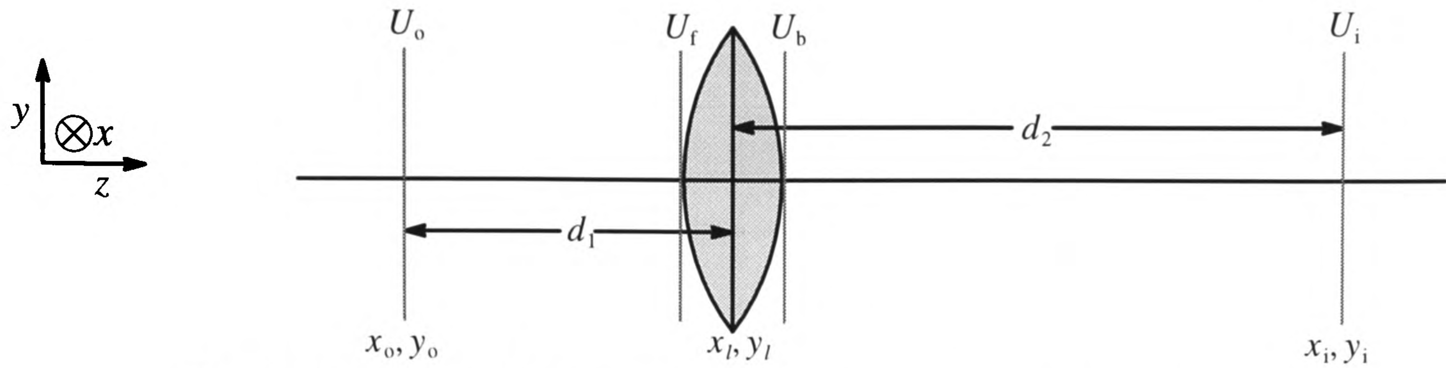

Fig. 8 Illustration of the Object, Lens (front and back) and Image notation.

Assuming, as we do for a thin lens, that the thickness of the lens is negligible compared to d_l or d_2, as defined in Fig. 8, we can write (from Appendix 1 [16])

$$U_f\,(x_l,y_l) = A\frac{e^{-jkd_1}}{j\lambda d_1}\; e^{-\frac{jk}{2d_1}\{x_l^2+y_l^2\}} \iint_{\Sigma_o} U_o(x_o,y_o)\; e^{-\frac{jk}{2d_1}\{x_o^2+y_o^2\}}\; e^{\frac{jk}{d_1}\{x_lx_o+y_ly_o\}}\; dx_o dy_o \tag{3}$$

As shown in Appendix 2 (eqn (195)), the phase shift, focussing and pupil function of the lens can be introduced as eqn (4).

$$U_b(x_l,y_l) = P(x_l,y_l)\,\exp\frac{jk}{2f}\left(x_l^2 + y_l^2\right)\,U_f(x_l,y_l) \tag{4}$$

and the field in the (x_i,y_i) plane is finally given by

$$U_i\,(x_i,y_i) = A\frac{e^{-jkd_2}}{j\lambda d_2}\; e^{-\frac{jk}{2d_2}\{x_i^2+y_i^2\}} \iint_{\Sigma_l} U_b(x_l,y_l)\; e^{-\frac{jk}{2d_2}\{x_l^2+y_l^2\}}\; e^{\frac{jk}{d_2}\{x_ix_l+y_iy_l\}}\; dx_l dy_l \tag{5}$$

These equations can be combined to enable us to express the field at the image plane $U_i(x_i,y_i)$, in terms of the field at the object plane, $U_o(x_o,y_o)$, and the lens parameters as shown in eqn (6).

$$U_i\,(x_i,y_i) = -A\frac{e^{-jk(d_1+d_2)}}{\lambda^2 d_1 d_2}\; e^{-\frac{jk}{2d_2}\{x_i^2+y_i^2\}} \iint_{-\infty}^{\infty}\iint_{\Sigma_o} U_o(x_o,y_o)\,P(x_l,y_l)\; e^{-\frac{jk}{2d_1}\{x_o^2+y_o^2\}}\; e^{-\frac{jk}{2}\{x_l^2+y_l^2\}\left(\frac{1}{d_1}+\frac{1}{d_2}-\frac{1}{f}\right)} e^{jk\left\{x_l\left(\frac{x_o}{d_1}+\frac{x_i}{d_2}\right)+y_l\left(\frac{y_o}{d_1}+\frac{y_i}{d_2}\right)\right\}}\; dx_o dy_o dx_l dy_l \tag{6}$$

When we assume the lens approximates to ideal behaviour such that the Lens Law $\left(\frac{1}{d_1} + \frac{1}{d_2} = \frac{1}{f}\right)$ holds and we can introduce the linear magnification $M = \frac{d_2}{d_1}$, eqn (6) can be rewritten as

$$U_i(x_i, y_i) = -A\frac{e^{-jkd_1(1+M)}}{\lambda^2 M d_1^2} e^{-\frac{jk}{2Md_1}\{x_i^2+y_i^2\}} \iint_{\Sigma_o} U_o(x_o, y_o)\, e^{-\frac{jk}{2d_1}\{x_o^2+y_o^2\}}\, h\left(x_o + \frac{x_i}{M}, y_o + \frac{y_i}{M}\right) dx_o dy_o \tag{7}$$

where
$$h(x,y) = \iint_{-\infty}^{\infty} P(x_l, y_l)\, e^{\frac{jk}{d_1}(x_l x + y_l y)}\, dx_l dy_l \tag{8}$$

which is the Fourier transform of the pupil function (neglecting the premultipling constant, as we do throughout the rest of this thesis).

The significance of *h(x,y)*, may be understood by considering an object which consists of a single point. Let us imagine it is positioned on the optic axis such that

$$U(x_0, y_0) = \delta(x_0)\,\delta(y_0) \tag{9}$$

After substitution into eqn (7) we have

$$U_i\,(x_i, y_i) = -A\frac{e^{jkd_1(1+M)}}{\lambda^2 M d_1^2}\, e^{-\frac{jk}{2Md_1}\{x_i^2+y_i^2\}}\, U(0,0)\; h\left(\frac{x_i}{M}, \frac{y_i}{M}\right) \tag{10}$$

The final factor in eqn (10) is therefore appropriately known as the Amplitude Point Spread Function or Impulse Response of the system and we shall make much use of it later on. The Intensity Point Spread Function is, of course, the modulus squared of h.

Returning to eqn (7) we see that it can be further simplified if we substitute the new variables $x' = x_o + \frac{x_i}{M}$ and $y' = y_o + \frac{y_i}{M}$. This is significant in the exponential x_o^2 and y_o^2 terms. An imaging system of reasonable quality has a point spread function that falls off quickly, so that x' and y' are small. Hence the exponential terms in x'^2, y'^2, $x'x_i$ and $y'y_i$

can be neglected compared to the x_i^2 and y_i^2 terms. In the interest of clarity we drop the constant factors from this point onwards.

$$U_i\,(x_i, y_i) = e^{-jkd_1(1+M)}\, e^{-\frac{jk}{2Md_1}\{x_i^2+y_i^2\}} \iint_{\Sigma_o} U_o(x_o, y_o)\; h\!\left(x_o + \frac{x_i}{M}, y_o + \frac{y_i}{M}\right) dx_o dy_o \tag{11}$$

ie
$$U_i = h \otimes U_o \tag{12}$$

where the symbol ⊗ denotes the convolution operation. This convolution of the object waveform with the point spread function shows that when diffraction effects are included, the image is no longer a perfect magnified replica of the object. Rather, the actual image obtained is a smoothed version of the object as a consequence of the non–zero width of the point spread function.

2.3 The Effect of Defocus

We now need to consider how the above result varies with small departures from the Lens Law. We model this by setting $d = d_1 + z$, (where $z << d_1$) and introduce into eqn (6) a generalised pupil function which includes the defocus factor, $P'(x_l,y_l)$, where

$$P'(x_l, y_l) = \exp(-jkz)\, \exp\left\{-\frac{jk}{2}\left(\frac{1}{d_1} + \frac{1}{d_2} - \frac{1}{f}\right)\left(x_l^2 + y_l^2\right)\right\} P(x_l, y_l) \tag{13}$$

Omitting the premultiplying phase terms, the field amplitude on the image plane is now described by

$$U_i\,(x_i, y_i) = \iint_{-\infty}^{\infty} \iint_{\Sigma_o} U_o(x_o, y_o)\;\; P'(x_l, y_l)\; e^{-\frac{jk}{2d_1}\{x_o^2+y_o^2\}} e^{jk\left\{x_l\left(\frac{x_o}{d_1}+\frac{x_i}{d_2}\right)+y_l\left(\frac{y_o}{d_1}+\frac{y_i}{d_2}\right)\right\}} dx_o dy_o dx_l dy_l \tag{14}$$

To simplify eqn (14) we can make use of the lens magnification again, and thus, with $x_o = -x_i/M$ and $y_o = -y_i/M$, we can, as before, neglect the remaining phase factor in the integral. We can now rewrite eqn (14) much more simply as

$$U_i\ (x_i, y_i) = \iint_{\Sigma_o} U_o(x_o, y_o)\ h\left(x_o + \frac{x_i}{M}, y_o + \frac{y_i}{M}\right)\ \mathrm{dx_o dy_o} \tag{15}$$

where the amplitude point spread function is defined in eqn (8), with P replaced by P' (from eqn (13)).

We can take advantage of the fact that all the systems we shall consider in this thesis are radially symmetric, and introduce the radial coordinate, r, via $x_l^2 + y_l^2 = r_l^2$. We now consider the case of a circular lens pupil of radius σ, such that we can introduce a normalized radial coordinate ϱ, where $\varrho = r_l/\sigma$ and the normalized axial coordinate, u, where

$$u = k\ \sigma^2 \left(\frac{1}{f} - \frac{1}{d_1} - \frac{1}{d_2}\right) \tag{16}$$

It should be noted that we can express the axial coordinate, u, more usefully in terms of the axial distance from the plane of focus, z, and the numerical aperture, $\sin\alpha$, where $\sin\alpha \simeq \sigma/d_1$. Using the definition of d and d_1 stated at the start of this section, we can write [15]

$$u \approx k\ z\ \frac{a^2}{dd_1} \approx 4\ k\ z\ \sin^2\!\left(\frac{\alpha}{2}\right) \tag{17}$$

This shows that the axial coordinate is proportional to the distance from the focal plane, z. We can now rewrite the pupil function as

$$\begin{aligned} P(u,\varrho) &= \exp\left(\frac{-ju}{4\sin^2\frac{\alpha}{2}}\right)\exp\left(\frac{ju\varrho^2}{2}\right) && |\varrho| \le 1 \\ &= 0, && \textit{otherwise} \end{aligned} \tag{18}$$

From this we can see that we may now allow for the effect of defocus simply by introducing this new pupil function into the point spread function of the system.

2.4 Imaging by the CSOM Optical System

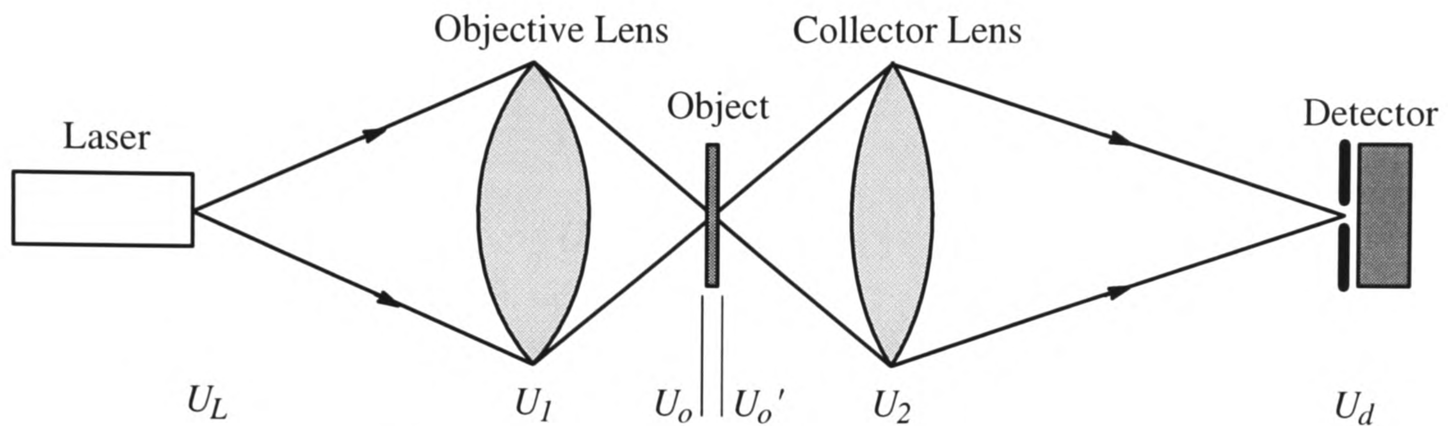

Fig. 9 Schematic Diagram of CSOM Optics.

As discussed in Chapter 1, the significant optical features of the CSOM are due to the fact that both the light source and detector are point–like and that both lenses are focussed on the same point on the object (hence 'confocal') as shown in Fig. 9. The point source means that we can immediately state that the optical field which probes the object is proportional to the amplitude point spread function of the objective lens $h_1(x_o,y_o)$. Given the amplitude transmittance of the object being viewed, $t(x_o,y_o)$, the expression for the field immediately after passing through the object is

$$U_o'(x,y) = h_1(x_o,y_o)\ t(x_o - x_s, y_o - y_s) \tag{19}$$

where (x_s,y_s) represents the scan position.

Since we require an expression for the detected signal we can apply eqn (11) to this situation and thus obtain the amplitude at the detector, $U_d(x_d,y_d)$. Hence

$$U_d\left(x_d, y_d : x_s, y_s\right) = \iint_{\Sigma_o} h_1(x_o,y_o)\ t(x_o - x_s, y_o - y_s)\ h_2\left(\frac{x_d}{M} - x_o, \frac{y_d}{M} - y_o\right)\ \mathrm{d}x_o \mathrm{d}y_o \tag{20}$$

If (as is true for a CSOM) the detector is a point on the optical axis ie ($x_d = y_d = 0$), and the point spread function is even, this convolution may be re–written as

$$U_d(x_s,y_s) = h_1\ h_2 \otimes t \tag{21}$$

In this thesis the CSOM is used in reflection mode, in which the objective and collector lenses are the same distances from the object and the source/detector (being the same lens), and hence the point spread functions for the two lenses are the same. As a result eqn (21) can be written

$$U_d(x_s, y_s) = h_1^2 \otimes t \tag{22}$$

2.5 The Effect of Finite Area Detectors

We now need to consider the fact that in this research single mode optical fibres are often used as spatial filters and the entrance to the fibre is not a mathematical point. Rather, it has its own Gaussian mode profile or sensitivity and this means that we need to consider an effective point spread function which replaces the original point spread function.

To investigate this we first need to consider the fibre or laser as a non–point source. If the source mode profile is $e(x_L, y_L)$ then the signal amplitude emitted by the source can be written as $e(x_L, y_L)$. Using eqn (12) we can now write the field incident on the surface of the specimen, $U_o(x_o, y_o)$, as the convolution of the point spread function of the lens, $h_1\left(x_o - \frac{x_d}{M}, y_o - \frac{y_d}{M}\right)$, and the source amplitude, $e(x_L, y_L)$,

$$U(x_o, y_o) = \int\int_{-\infty}^{\infty} e(x_L\ , y_L)\ h_1\left(x_o - \frac{x_L}{M}, y_o - \frac{y_L}{M}\right)\ \mathrm{d}x_L \mathrm{d}y_L \tag{23}$$

$$U_o(x_o, y_o) = h_1 \otimes e_L \tag{24}$$

This convolution essentially defines an effective point spread function, h_{1eff}, where

$$h_{eff} = h \otimes e \tag{25}$$

Clearly, when h is much broader than e, $h_{eff} \rightarrow h$.

Next we consider the effect of the detector mode profile which is given by eqn (2). We substitute h_{eff} for h_1 in eqn (20) and substitute U_d from there into eqn (2), which gives

$$I = \left| \iint_{\Sigma_o} \iint_{\Sigma_d} h_{1eff}(x_o, y_o)\ t(x_s - x_o, y_s - y_o)\ h_2\left(\frac{x_d}{M} - x_o, \frac{y_d}{M} - y_o\right)\ e(x_d, y_d)\ \mathrm{d}x_d \mathrm{d}y_d \mathrm{d}x_o \mathrm{d}y_o \right|^2 \tag{26}$$

$$I = \left| \iint_{\Sigma_o} h_{1eff}(x_o, y_o)\ h_{2eff}(x_o, y_o)\ t(x_s - x_o, y_s - y_o)\ \mathrm{d}x_o \mathrm{d}y_o \right|^2 \tag{27}$$

and hence

$$I = \left| h_{1eff}\, h_{2eff} \otimes t \right|^2 \tag{28}$$

where

$$h_{1eff} = h_1 \otimes e_L \quad \text{and} \quad h_{2eff} = h_2 \otimes e_d \tag{29}$$

Finally, if the system is reciprocal, with the source and detector being the same fibre, and therefore having the same mode profile, $e(x_L, y_L)$, (such as is illustrated in Fig. 5), and the same lens acts as the objective and collector lens (as happens in the reflection scheme), then $h_{1eff} = h_{2eff}$. We can therefore write

$$I = \left| h_{eff}^2 \otimes t \right|^2 \tag{30}$$

or in terms of amplitude

$$U_d = h_{eff}^2 \otimes t \tag{31}$$

2.5.1 Axial Responses

To show the difference this makes in practice we now consider the response of the microscope to a perfect reflector moving in the axial direction. The axial response of this simple test scheme is easy to obtain experimentally, and its shape is very sensitive to any irregularities such as aberrations or system misalignments. For a perfect reflector ($t = 1$) we can rewrite eqn (31) as

$$U_d = \iint_{-\infty}^{\infty} h_{eff}^2 \, dx_o \, dy_o \tag{32}$$

This can be rewritten using radial coordinates (since the lenses we use are radially symmetric) in terms of the pupil function defined in eqn (18) (as shown in eqn (8)), to give

$$U_d = \int_0^{\infty} P_{eff}(u,\varrho)\; P_{eff}(u,-\varrho)\; \varrho \; d\varrho \tag{33}$$

2.5.1 .1 *Pinhole Detectors*

For the limiting case, when h is much broader than e, and h_{eff} becomes h we can substitute for the pupil function, given by eqn (18), which gives

$$U_d = e^{-\frac{ju}{2\sin^2\frac{\alpha}{2}}} \int_0^1 e^{ju\varrho^2} \; \varrho \; d\varrho \tag{34}$$

When evaluated, ignoring constant phase factors, this gives the following expressions for the image of a plane

$$U_d = \frac{\sin\,(u/2)}{u/2} \tag{35}$$

and

$$I_d = \left\{\frac{\sin\,(u/2)}{u/2}\right\}^2 \tag{36}$$

2.5.1 .2 *Small Finite Area Detectors*

However when we cannot neglect the effect of e relative to h we can allow for it by expressing it as the Gaussian $\left(\exp - \dfrac{r^2}{a}\right)$. This models the fundamental transverse mode of an optical fibre or, as we shall need later on, the fundamental transverse mode of a laser. We know that the pupil function is the Fourier transform of the point spread function (eqn (8)) so we can simply include the additional factor of the Fourier transform of the mode profile

which is also a Gaussian, $\left(\exp - \frac{a\varrho^2}{4}\right)$, in the expression for the pupil function. As a result the effective pupil function, P_{eff}, can be written as eqn (37).

$$P(u,\varrho) = \exp \frac{j\varrho^2}{2}\left(u + \frac{ja}{2}\right)\exp\left(\frac{-ju}{4\sin^2\frac{\alpha}{2}}\right) \qquad |\varrho| \leq 1 \tag{37}$$

$$= 0 \qquad \textit{otherwise}$$

The integral in eqn (33) can now be calculated once again and gives the following expression for the microscope axial response for a perfect reflector

$$U_d = \operatorname{sinc}\left\{\frac{1}{2}\left(u + \frac{ja}{2}\right)\right\}\exp\left(-2j\,k\,z\cos^2\frac{\alpha}{2}\right) \tag{38}$$

where sinc $x = \frac{\sin x}{x}$. Also

$$I_d = 4\sinh^2\frac{a}{4}\ \frac{\left(\coth\frac{a^2}{4}-1\right)\sin^2\frac{u}{2} + 1}{\left(\frac{u}{2}\right)^2 + \left(\frac{a}{4}\right)^2} \tag{39}$$

These results are used throughout the following research and their accuracy is readily seen, when compared with the experimental results presented.

2.6 Spatial Frequencies

As we saw in the last section, it can be very convenient to be able to use separate terms to describe the object and the optical system. In normal spatial co–ordinates this is not possible. However in eqn (31) we can see that the detected amplitude of the image can be expressed as the convolution of the square of the point spread function of the objective lens and the specimen reflectivity. We know that one of the properties of Fourier transforms is that the Fourier transform of a convolution can equally be expressed as the product of the Fourier transforms of the terms being convolved, or, in this case

$$\mathcal{F}\{U_d\} = \mathcal{F}\{h^2_{eff}\} \, . \mathcal{F}\{t\} \tag{40}$$

where $\mathcal{F}\{.\}$ denotes the Fourier transform. We therefore choose to express the detected amplitude, U_d, the effective point spread function, h_{eff}, and the amplitude reflectivity of the specimen, t, in terms of their *spatial frequencies* with units μm^{-1}, by means of the Fourier transform. Thus if the object, $U(x,y)$, is expressed as the spatial frequency spectrum, $T(m,n)$, and the response of the optical system (the Fourier transform of $h_{eff}{}^2$) as $c(m,n)$, then we write the output spectrum as $T(m,n).c(m,n)$ and the output signal as the inverse Fourier Transform of the spectrum.

To express the reflectivity of the object in terms of spatial frequencies we use the inverse Fourier Transform, as shown in eqn (41).

$$t(x_o, y_o) = \iint_{-\infty}^{\infty} T(m,n) \;\; e^{-2\pi j\{mx_o + ny_o\}} \, dmdn \tag{41}$$

Using the inverse Fourier transform, this can now be substituted into eqn (31), giving

$$U_d \, (x_s, y_s) = \iint_{-\infty}^{\infty} \iint_{-\infty}^{\infty} h_1^2(x_o, y_o) \; T(m,n) \; e^{-2\pi j\{mx_o + ny_o\}} \; e^{2\pi j\{mx_s + ny_s\}} \;\; dx_o dy_o dmdn \tag{42}$$

We can now re–write this as

$$U_d(x_s, y_s) = \iint_{-\infty}^{\infty} T(m,n)\ c(m,n)\ e^{2\pi j\{mx_s + ny_s\}}\ dmdn \tag{43}$$

where
$$c(m,n) = \iint_{-\infty}^{\infty} h_1^2(x_o, y_o)\ e^{-2\pi j\{mx_o + ny_o\}}\ dx_o dy_o \tag{44}$$

This separation of *T(m,n)* and *c(m,n)* is an important result since it shows how the object and optical system can be considered separately. Hence we can study different features of the optical system, *c(m,n)*, without having to refer to a specific object. We shall now derive an expression for *c(m,n)* in terms of the pupil function we discussed earlier.

From eqn (8) we know that the point spread function, *h*, is the Fourier Transform of the pupil function, *P*,

$$h(x,y) = \iint_{-\infty}^{\infty} P(r,s)\ e^{2\pi j(rx+sy)}\ drds \tag{45}$$

Substituting for h_1 in eqn (44) gives

$$c(m,n) = \iint_{\Sigma_0} \iint_{-\infty}^{\infty} \iint_{-\infty}^{\infty} P(r,s)P(r',s')\ e^{2\pi j(rx+sy)}\ e^{2\pi j(r'x+s'y)} e^{-2\pi j\{mx_o+ny_o\}}\ dr'ds'\ drds\ dx_o dy_o \tag{46}$$

However, since

$$\iint_{-\infty}^{\infty} e^{2\pi j\{r+r'-m\}x_o}\ e^{2\pi j\{s+s'-n\}x_o}\ dx_o dy_o = \delta(r + r' - m)\ \delta(s + s' - n) \tag{47}$$

we can see that in the integral over r' s', the only non–zero for values occur when $r' = m - r$ and $s' = n - s$.

This means that eqn (44) can now be expressed as

$$c(m, n) = \iint_{-\infty}^{\infty} P(r, s)\ P(m-r, n-s)\ \mathrm{d}r\mathrm{d}s = P(r, s) \otimes P(r, s) \tag{48}$$

It is in this way that the pupil function can be introduced into the Fourier transform of the object waveform.

It should be noted that, from eqn (18) we know that the generalised pupil function includes a factor, u, which describes the defocus, and can be further generalised to account for the effect of a finite size detector, as shown in eqn (37). Also, it is more useful to express the pupil function in radial coordinates since the lenses we use are circularly symmetric. Hence we can write eqn (48) as

$$c(u, \tilde{\varrho}) = P(u, \varrho) \otimes P(u, \varrho) \tag{49}$$

where $P(u,\varrho)$ is defined in eqn (37).

3. Laser Theory for Optical Feedback

3.1 Introduction

So far we have looked at how the signal reflected from the specimen is detected by a single mode fibre and how this varies with defocus in a CSOM. However, in some of the following research we use an optical system in which the reflected signal is fed from the fibre back into the internal cavity of the laser illuminating the specimen in the microscope (as illustrated in Fig. 6). Later we consider a system in which we dispense with the fibre altogether and feed the reflected signal back into the laser cavity directly, using the single transverse mode of the laser to act as the spatial filter required for confocal imaging. In both arrangements (with and without the optical fibre) we use the laser as an optical detector and we therefore need to establish how the measured output from the laser varies with the signal being fed back into it.

We start by considering a compound cavity model of the microscope, which consists of a laser cavity coupled through the laser output mirror to an external cavity. This external cavity is essentially the optical system of the microscope, between the laser output mirror and the object. In the model, the microscope signal from the object is represented as a variable reflectivity from a mirror at the object end of the external cavity. We then show that the signal reflected from the object can be regarded as a perturbation of the reflectivity of the output mirror of the laser cavity, providing the coupling between the cavities is very low, as is the case for a HeNe laser. However, the coupling from a semiconductor laser is too high for this approximation to be valid, so we develop a fuller theory, based on laser dynamics, to describe the influence of the external reflectivity on the action of the laser.

3.2 Reflectivity Model of the Compound Laser Cavity

In this analysis we account for the effect of feeding light from the specimen back into the laser cavity by treating the external cavity mirror (which represents the microscope system) and the laser cavity mirror (coupling the laser and external cavities) as a compound mirror with effective reflectivity R. We investigate how R depends on the amplitude reflectivity of the object mirror, R_S, which is proportional to the confocal amplitude image from the microscope system. Further, we consider the response of the laser to the varying phase of the microscope signal.

Consider the following arrangement in which the laser internal cavity is bounded by lossless mirrors with amplitude reflectivities R_1 and R_2 and the external cavity by mirrors R_2 and R_S. We neglect multiple reflections in the external cavity since, in all the experimental arrangements we used, they were always much weaker than the initial reflection, because of factors such as low coupling efficiencies between the fibre and the laser cavity and reflection losses in the objective lens system. The propagation of a beam of amplitude E_0 at mirror R_2 is described in Fig. 10, in which ω is the angular frequency of the laser signal and τ is the round–trip time of the wavefront in the external cavity.

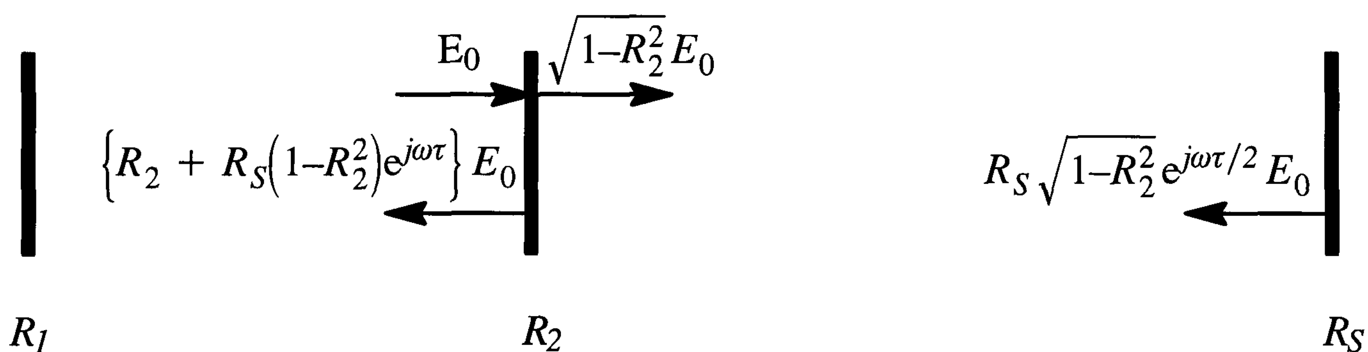

Fig. 10 Amplitude and phase variation throughout a schematic double (laser and external) cavity.

From Fig. 10 we can see that the additional contribution to the reflectivity of the coupling mirror resulting from the presence of the external cavity can be expressed as $R_S\left(1-R_2^2\right)e^{j\omega\tau}$. The presence of the additional reflectivity reduces the effective cavity losses which results in the lasing threshold being achieved for a lower rate of population inversion than for the isolated laser. Above this an increase in population inversion results in an increase in inten-

sity (until saturation) and hence the additional reflectivity results in the generation of a higher laser intensity than happens for the same rate of population inversion in an isolated laser.

Within the laser cavity the phase change after a round–trip must be zero and the lasing frequency will always adjust to ensure this is so. Therefore when a new wavefront is added into the cavity but with a different phase, the frequency will adjust to make the overall round–trip phase change zero again.

From this analysis we are seeking an expression for the change in the intensity emitted from the laser, through mirror R_1, resulting from the additional reflectivity in the external cavity. It is therefore necessary to consider how this additional reflectivity is to be correctly added to the reflectivity of the cavity mirror. This is shown in Fig. 11. There we can also clearly see the coupling of the laser frequency, ω, and the external cavity period, τ, to the change of the phase of the wavefront at the coupling mirror within the laser cavity, $\Delta\Psi$, resulting from the microscope signal (here considered as the specimen reflectivity, R_S).

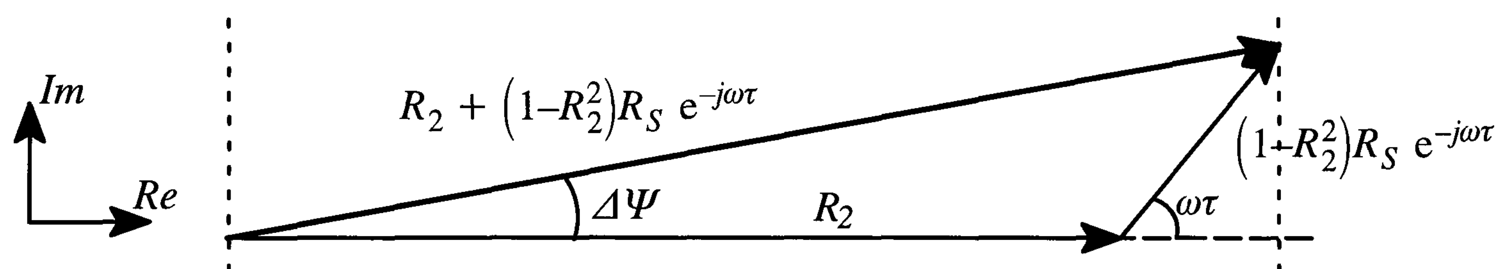

Fig. 11 Vector illustration of the addition of the specimen and cavity reflectivities.

It is the absolute mirror reflectivity which influences the intensity within the laser cavity and, when the feedback signal is small, this can be approximated as R' where

$$R' = \mathrm{Re}\left\{R_2 + \left(1-R_2^2\right)R_S\ e^{-j\omega\tau}\right\} \tag{50}$$

Bearing in mind the assumption, stated earlier, that all the cavity reflectivities are real, this can be rewritten as

$$R' = R_2 + \left(1-R_2^2\right)\ \mathrm{Re}\left\{R_S\ e^{-j\omega\tau}\right\} \tag{51}$$

We now wish to describe the effective reflectivity of the specimen, R_S, for the general experimental arrangement (which includes a fibre between the laser and the specimen) in terms of the *intensity* coupling coefficient between the fibre and the laser, η, and the microscope signal, s, ie the fraction of the optical field coupled back into the fibre after reflection from the specimen. (Note that this was calculated in Chapter 2, and summarized in eqn (31).) We can therefore express the specimen amplitude reflectivity, R_S, as ηs. The intensity coupling coefficient, η, appears because light is coupled into the fibre twice, once from the laser into the fibre and secondly back from the fibre into the laser.

If we replace R_S by ηs, eqn (51) becomes

$$R' = R_2 + \left(1-R_2^2\right) \eta \ \mathrm{Re}\left\{s \ \mathrm{e}^{-j\omega\tau}\right\} \tag{52}$$

Notice s is in general complex and so maybe written as

$$s = |s| \ \mathrm{e}^{j\phi} \tag{53}$$

Hence we can finally express the compound mirror reflectivity as

$$R_2 + \left(1-R_2^2\right) \eta \ |s| \ \mathrm{Re}\left\{\mathrm{e}^{-j(\omega\tau-\phi)}\right\} \tag{54}$$

The exponential term included in expression (54) shows the dependence of the system on the laser frequency, ω, and on the round–trip time of the signal in the external cavity, τ, as well as any phase shift caused by the microscope, ϕ. Clearly τ varies as the distance from the laser to the specimen varies, either due to the specimen being scanned axially or variations of its surface profile as it is scanned laterally. However the laser frequency, ω, can also vary in some situations and we therefore need to investigate the effect of this variation on the whole phase term.

From Fig. 11 we can see that the variation in the phase of the wavefront at the coupling mirror in the laser cavity is $\Delta\Psi$ and this is coupled to $\omega\tau$. This results in a coupling between the intensity and wavelength in the cavity. Any variation in τ or $|s|$ results in a change in $\Delta\Psi$ as well as in the cavity intensity and this change in $\Delta\Psi$ results in a compensating change in ω

to bring the round–trip phase back to zero. This results in a further change in $\Delta\Psi$ and so on. Using this model, it is difficult to see where the iterations lead in every case and therefore a more detailed model is developed in the next section to describe more precisely the result of this coupling between the phase and intensity which results from the feedback from the external cavity.

However this model is of direct value in the case of weak coupling, which occurs when the reflectivity of the cavity coupling mirror, R_2, is much greater than the additional effective reflectivity resulting from the presence of the external cavity, $\left(1-R_2^2\right)R_S\ e^{-j\omega\tau}$. In this case $\Delta\Psi$ remains small during any variations of τ or $|s|$ and the resulting variation of the lasing frequency ($\Delta\omega$) has a negligible effect on the phase shift $\omega\tau$, and hence there is no further effect on $\Delta\Psi$. This decoupling occurs in the case of the HeNe laser, in which R_2 has a value in excess of 99%. However in the case of a semiconductor laser, R_2 has a value of around 55%. Since the intensity coupling, η, is no higher than 0.2, the additional reflectivity from the specimen is still only about $0.1R_2$, but the coupling is now significant and leads to complex phenomena, which are described in more detail in the next section.

3.3 Dynamical Laser Theory

3.3.1 Theoretical Basis

The case of a semiconductor laser with an external cavity was first analysed by Lang and Kobayashi in 1980 [17]. They started their analysis with the fundamental dynamical equation for the electric field within a laser, which can be expressed as

$$\frac{d}{dt}E(t) = \left\{j\omega(N) + \frac{1}{2}\left(G(N)-G_{th}\right)\right\} E(t) + \frac{\varkappa}{\tau_L}\ E(t-\tau) \tag{55}$$

where $E(t)$ is the complex electric field inside the laser cavity. N is the carrier density in the lasing medium and $G(N)$ is the gain per unit time of the lasing medium. G_{th} is the gain of an

isolated laser at threshold, which is equivalent to the cavity loss of the laser cavity. ω is the cavity frequency and τ_L is the cavity roundtrip time. $\varkappa$ is defined as

$$\varkappa = \frac{\left(1 - R_2^{\ 2}\right)R_S}{R_2} \tag{56}$$

which is clearly the ratio of the amplitude reflected from the external cavity back into the laser cavity, $R_S(1-R_2^{\ 2})$, to the amplitude reflectivity of the laser mirror, R_2.

Since the change in carrier density is caused by the change in effective cavity reflectivity due to the external cavity, and this is small relative to the mirror reflectivity of the cavity, we can assume that the gain is linear for small changes in N around the threshold value for an isolated laser, N_0.

$$G(N) - G_{th} = \beta\left(N\text{–}N_0\right) \tag{57}$$

where $\beta = \frac{\partial G}{\partial N}$ at $N = N_0$

We can also expand $\omega(N)$ for small changes in N as

$$\omega(N) - \omega_0 = \gamma\left(N\text{–}N_0\right) \tag{58}$$

where $\gamma = \frac{\partial \omega}{\partial N}$ at $N = N_0$

We can now substitute from eqns (57) and (58) into eqn (55) and, for clarity, separate the complex expression for $E(t)$ into real–valued quantities of electric field and phase, using

$$E(t) = E_0(t)\ e^{j(\omega_0 t + \phi(t))} \tag{59}$$

where $E_0(t)$ is the slowly varying electric field amplitude and $\phi(t)$ the contribution to phase variation. ω_0 is the oscillation frequency of the isolated laser. Separating the resulting equation into real and imaginary parts, gives

$$\frac{d}{dt}E_0(t) = \frac{1}{2}\ \beta\ \left(N\text{–}N_0\right)E_0(t) + \frac{\varkappa}{\tau_L}\ E_0(t\text{–}\tau)\ \cos\left(\omega_0\tau + \phi(t) - \phi(t\text{–}\tau)\right) \tag{60}$$

$$\frac{d}{dt}\phi(t) = \gamma \left(N - N_0\right) - \frac{\varkappa}{\tau_L} \frac{E_0(t-\tau)}{E_0(t)} \sin\left(\omega_0 \tau + \phi(t) - \phi(t-\tau)\right) \tag{61}$$

We also require the rate equation for the carrier density, N, given by

$$\frac{d}{dt}N(t) = J - \frac{N}{\tau_s} - G(N)\ I \tag{62}$$

where J is the pumping term, τ_s is the carrier lifetime and I is the photon density within the active layer of the laser.

It should be noted that these equations can be applied to any laser, not simply the semiconductor laser for which they were introduced in this chapter. However, in the case of a HeNe laser, the dependence of the lasing frequency on the carrier density is negligible.

In the absence of optical feedback, the steady state of an isolated laser is characterised by photon density, I_0, and carrier density, N_0. From eqn (62) we can see that they are related as

$$J = \frac{N_0}{\tau_s} + G_{th} I_0 \tag{63}$$

This enables us to rewrite eqn (62), for constant J, as

$$\frac{d}{dt}N(t) = -\left(N - N_0\right)\left(\frac{1}{\tau_s} + \beta I\right) - G_{th}\left(I - I_0\right) \tag{64}$$

Using eqns (60), (61) and (64) as the basic description of our model we can now look for solutions. For any steady state solution to this model, N must be time–independent and $\phi(t) = \Delta\omega\, t$, where $\Delta\omega$ is the time–independent shift to the new angular frequency, ω_s, due to the external cavity ie $\omega_s = \omega_0 + \Delta\omega$. Inserting these constant expressions into the model we obtain the following conditions for steady state solutions

$$\Delta\omega = -\frac{\varkappa}{\tau_L}\left(2\frac{\gamma}{\beta}\cos\omega_s\tau + \sin\omega_s\tau\right) \tag{65}$$

$$I = I_0 + 2\frac{\varkappa}{\tau_L}\frac{\left(I_0 + \frac{1}{\beta\tau_s}\right)\cos\omega_s\tau}{G_{th} - 2\frac{\varkappa}{\tau_L}\cos\omega_s\tau} \tag{66}$$

It should be noted that the ratio $2\gamma/\beta$ is conventionally referred to as the linewidth enhancement factor, b, [18,19,20] and is commonly expressed as

$$b \equiv 2\frac{\partial\omega}{\partial N}/\frac{\partial G}{\partial N}\bigg|_{N=N_0} \tag{67}$$

We now look more closely at these conditions to understand their implications.

3.3.2 Phase Variation and Introduction of Parameter *C*

We consider first the phase condition, eqn (65). It can be solved graphically, and to do so we rearrange it and introduce a new variable $\Delta\psi$. The solution is given when $\Delta\psi = 0$, where

$$\Delta\psi = \Delta\omega\,\tau + C\,\sin\left(\Delta\omega\,\tau + \omega_0\tau + \arctan b\right) \tag{68}$$

where

$$C = \varkappa\,\frac{\tau}{\tau_L}\sqrt{1 + b^2} \tag{69}$$

$\Delta\psi$ is plotted against $\Delta\omega$ in Fig. 12 for various values of the dimensionless parameter C [21], when τ is held constant at a typical value of 6ns. The solutions, $\omega_0 + \Delta\omega$, for $\Delta\psi = 0$ are the allowed lasing frequencies for the laser with feedback.

From Fig. 12 we can see that as long as C is less than unity $\Delta\psi$ increases monotonically with $\Delta\omega$, yielding a single zero for $\Delta\psi$ and therefore a single lasing frequency. However as C increases the perturbations increase until a critical point at $C = 1$, above which the curve cuts the axis at more than one point indicating the existence of more than one possible emission frequency. As C increases further the number of $\Delta\psi = 0$ intercepts increases and hence the number of possible emission frequencies increases.

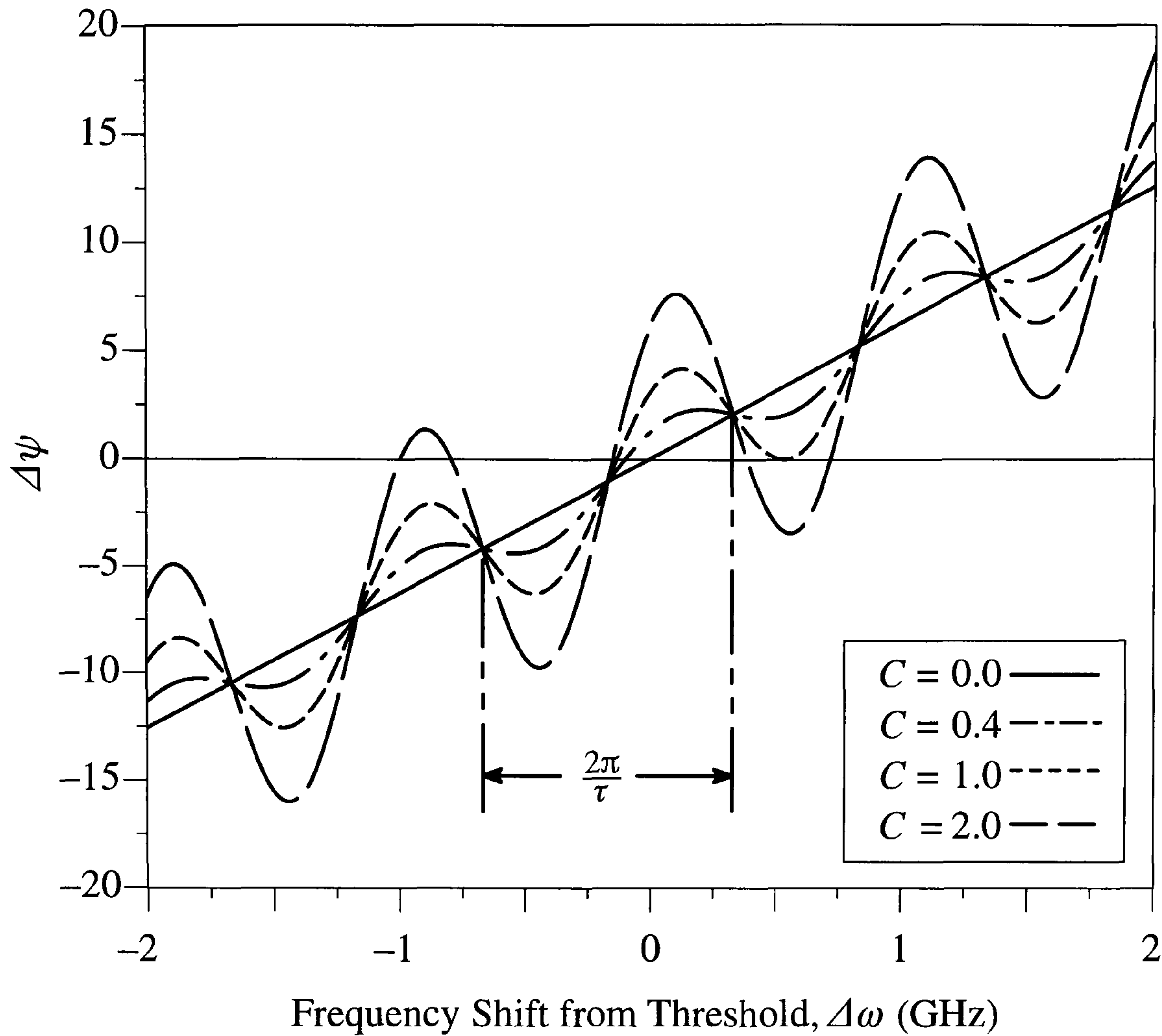

Fig. 12 The effect on $\Delta\psi$ of varying C as $\Delta\omega$ is varied.

3.3.3 The Physical Meaning of C

We now look at the factors in the parameter C and consider their meaning and typical values for the HeNe and semiconductor lasers we use.

As stated earlier, $\varkappa$ is the ratio of the amplitude reflected from the external cavity which re–enters the laser, relative to the amplitude reflected from the coupling mirror between the laser and the external cavity. For the feedback signals we shall consider here $\varkappa \ll 1$ (typically < 0.1). To understand the importance of this factor on the intensity and frequency of a laser subject to feedback, we can refer back to Fig. 11 where it is clear that as $R_S\left(1-R_2^2\right)$ increases relative to R_2 so the coupling between $\Delta\Psi$ and $\Delta\omega$ increases. Hence the coupling between the laser frequency and intensity increases, as described earlier.

The ratio τ/τ_L is the roundtrip time in the external cavity, τ, relative to the roundtrip time in the internal laser cavity, τ_L. For the experimental arrangement we used, the optical length

of the external cavity is typically 1m and the length of the laser cavity in a HeNe laser is roughly 20cm. Hence τ/τ_L is of order 1 for a HeNe laser. For a semiconductor laser, on the other hand, the cavity length is about 250μm, which, together with a refractive index of about 3.6, gives a value for τ/τ_L of the order 10^3. Reference to Fig. 11 once again illustrates how the magnitude of this factor affects the coupling between the laser frequency and intensity.

The factor $\sqrt{(1+b^2)}$ gives the dependence on the spectral linewidth enhancement factor, b. This results from the dependence of the real part of the refractive index of the lasing medium on the carrier density. In gas lasers the refractive index in the laser cavity is relatively unaffected by any change in the carrier density and hence $b \approx 0$ for HeNe lasers. However, in semiconductor lasers the intensity reflected from the specimen changes the carrier density which does affect the refractive index in the active region where the lasing occurs. This change in refractive index in the laser cavity affects the wavelength of the cavity wave since it changes the effective optical length of the cavity which must still hold an integer number of wavelengths. As a result there is a coupling between the amplitude and phase fluctuations in the electric field in the laser cavity.

For a given semiconductor laser b is constant but it varies between different laser types, though its value usually lies between 1 and 10 [19]. Hence it can increase the value of C by a similar factor.

3.3.4 The Experimental Significance of *C*

We can now see why C is so significant: it contains all the factors which govern the coupling of the laser frequency and intensity. Lenstra et al [22] stated, "C is a natural measure for the effectiveness of the feedback mechanism to change the behaviour of the optical field in the laser".

The case $C = 1$ is significant because it separates the 'weak' from the 'strong' feedback cases. When $C \ll 1$, as is the case for a HeNe laser, only a single longitudinal laser mode is

generated at a frequency which is just slightly perturbed from the natural laser frequency by the feedback. As a result the HeNe laser system can be adequately described by the compound reflectivity model outlined in section 3.2 of this chapter.

However when $C > 1$, which is the case for a semiconductor laser, eqn (68) gives multiple solutions for ω_s [23], which indicates that the perturbation by the feedback is sufficient to allow several frequencies to be generated, each of which turns out to be a perturbation of one of the modes of the external cavity. Because these external cavity modes are very close together it is possible for the laser to 'hop' between these modes. It has been shown that the system chooses the mode with the smallest linewidth (lowest noise) which is usually the one with the lowest threshold gain, ie the highest lasing intensity for a given pumping strength [24,25].

3.3.5 The Effect of Varying the External Cavity Length

3.3.5 .1 *Frequency Variation*

We can now consider the effect on the lasing frequency of moving the remote external cavity mirror, ie changing τ.

In Fig. 13 $\Delta\omega\,\tau$ is plotted against $\omega_0\tau$ for different values of C according to eqn (70)

$$\Delta\omega\,\tau = -C\sin\left(\Delta\omega\,\tau + \omega_0\tau + \arctan b\right) \tag{70}$$

To calculate the curves shown in Fig. 13 we set the value of b at the typical value of 4.

For $C < 1$ (Fig. 13(a)) we can see that the variation in frequency from that of an isolated laser is a single valued periodic function with period 2π. This is the case for the HeNe laser, as described earlier in this chapter and modelled in eqn (54).

As C increases above unity (Fig. 13(c) and (d)), the frequency becomes multivalued for some or all values of $\omega_0\tau$. Not all the solutions are stable and indeed there are various constraints on the stability of a feedback system. It has been shown by Tromborg et al [26]

that a phase condition applies which states that a necessary, though not sufficient condition for a stable solution is $\frac{d\omega_0}{d\omega_s} > 0$, where $\omega_s = \omega_0 + \Delta\omega$. From eqn (70) we see that

$$\frac{d\omega_0}{d\omega_s} = 1 + C\cos(\omega_s \tau + \arctan b) \tag{71}$$

This means that as $\omega_s\tau$ passes a maximum of $\omega_0\tau$ (for increasing $\omega_s\tau$) the solution becomes unstable until it passes a minimum of $\omega_0\tau$ again [22,27]. The regions for which eqn (71) is violated are always between two regions for which eqn (71) is true. These stable solutions are marked in Fig. 13 by bold lines. It can be shown that if phase fluctuations were the only cause of instability then eqn (71) would be both the sufficient and necessary condition for stability. However, when intensity fluctuations are particularly significant, eqn (71) is no longer sufficient, and transitions between these regions occur rapidly. These transitions are enabled by the presence of noise such as is due to spontaneous emission in the laser cavity.

Fig. 13 also illustrates how the distance between adjacent stable frequencies decreases as C increases. The spacing tends to approach the "external" frequency spacing ($2\pi/\tau$). Hence we can consider the stable solutions for $C > 1$ to be perturbed external cavity modes.

As has already been mentioned, transitions between phase stable states are stimulated by noise resulting from spontaneous emission, etc. However, it has been shown by Tkach and Chraplyvy [28] that there are five different regimes of optical feedback which are marked by different levels of feedback. For our purposes the most important of these is termed Coherence Collapse and occurs at high feedback levels ($C \geq 50$), when all states become unstable and transitions occur randomly. This is the regime which dominates under the feedback levels experienced by the semiconductor laser in the microscopes described in this thesis when the injection current is in its usual operating range. In this regime the laser hops randomly between adjacent frequencies but as the value of C increases these hops become shorter, and in the next section we shall see that this results in a decrease in the amplitude of the fluctuations in intensity.

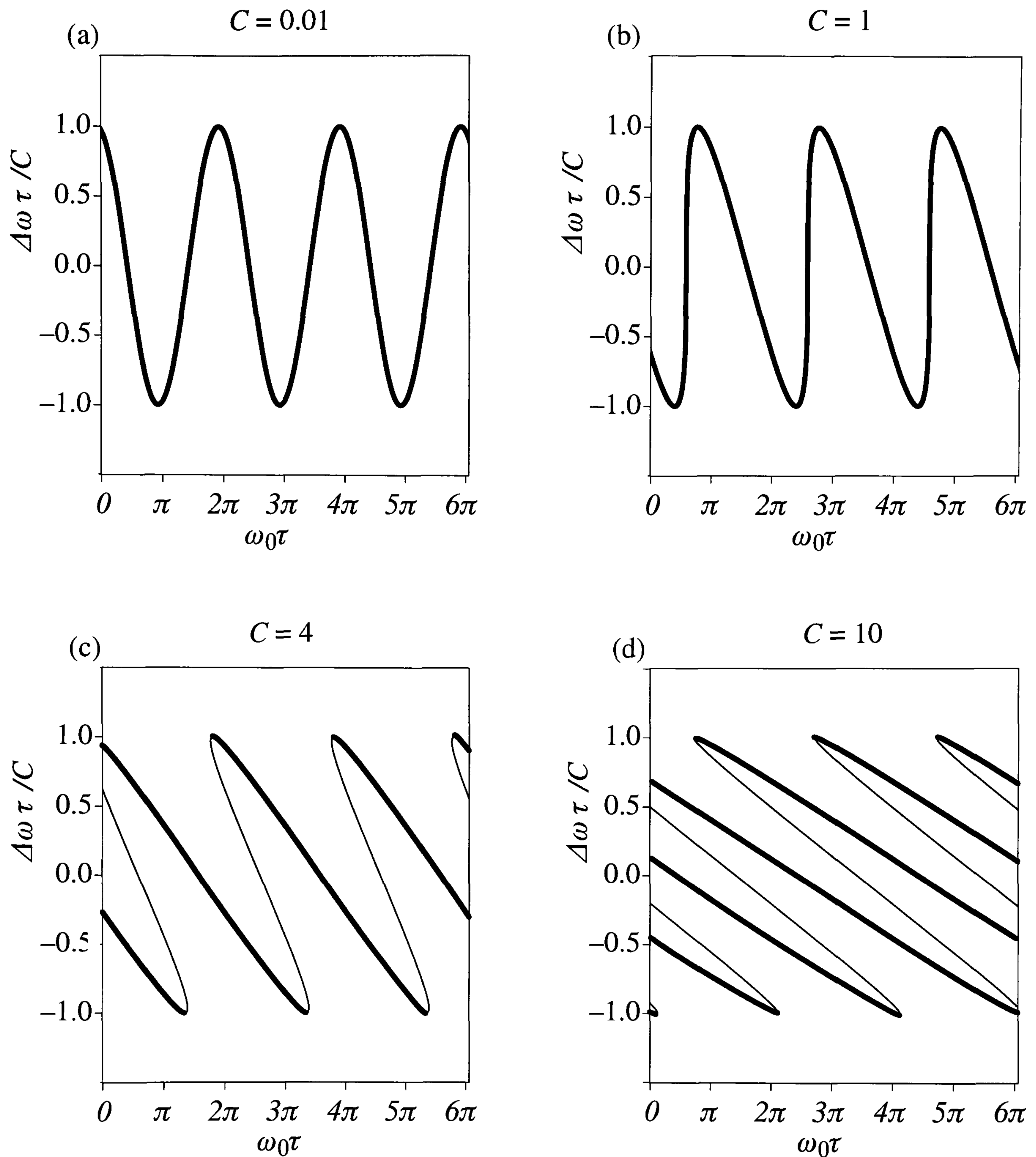

Fig. 13 $\Delta\omega\tau / C$ against $\omega_0\tau$ for different values of C, with $b = 4$.

The increased ease of mode hopping between adjacent modes which becomes possible for higher values of C has a very important, practical implication and this is the change in phase which accompanies it. When an object is scanned and the round–trip period, τ, varies, the resulting change of phase of the wavefront re–entering the laser cavity is compensated for by a jump in the frequency of the laser so as to keep the phase of the wavefront constant. In this way the laser can maintain the highest intensity for the level of pumping being used. Hence all phase information in the reflected wave is lost automatically, leaving only the amplitude information.

Using the form of eqn (54), we can express this as $(\phi - \omega_S \tau) \approx 0$. The variation in the effective reflectivity of the coupling laser mirror is therefore solely dependent on the amplitude of the signal reflected from the specimen $|s|$, which, in a confocal arrangement, depends on the position of the specimen, ie $s(z,y,z)$. Since the phase term is cancelled out we are left with the following expression for the effective reflectivity at mirror R_2.

$$R_2 + \left(1 - R_2^2\right) \eta \; |s| \tag{72}$$

3.3.5 .2 *Intensity Variation*

The laser intensity of feedback systems is governed by eqn (66). This can be simplified if we consider typical values of the various factors involved. In the numerator we have terms which represent the stimulated emission (I_0) and spontaneous emission ($1/\beta\tau_s$) of the laser, of which the stimulated term is much the greater when the laser is operating well above threshold. In the denominator are terms describing the losses from the cavity, but in our system, the laser threshold gain (or cavity loss), $G_0 \approx 1$THz, is much greater than the change in gain due to the external reflectivity (max $\varkappa/\tau_L \approx$ 0.1 / 5ps = 20GHz).

Hence eqn (66) simplifies to

$$\Delta I = I - I_0 \approx 2\frac{\varkappa}{\tau_L} \frac{I_0}{G_0} \cos\left(\Delta\omega\,\tau + \omega_0 \tau\right) \tag{73}$$

We now wish to consider how the intensity emitted from the laser cavity varies, ΔI, with the round–trip time in the external cavity, τ, as described in eqn (73). In Fig. 14 we plot the intensity variation for the same values of C we used in Fig. 13. Bold lines are used to mark typical intensities which may be observed as τ is varied.

It now becomes clear that as the value of C increases so the number of transitions possible around the maximum intensity increases markedly. Hence it becomes increasingly unlikely that there are any random transitions to significantly lower values of intensity and hence the variation in intensity decreases. This results in the intensity in the laser cavity becoming virtually independent of the phase of the microscope signal which has been fed back. We

can therefore rewrite the change in intensity of the laser cavity due to feedback, at medium to high levels of feedback, as

$$\Delta I \approx 2\frac{\varkappa}{\tau_L}\frac{I_0}{G_0} \tag{74}$$

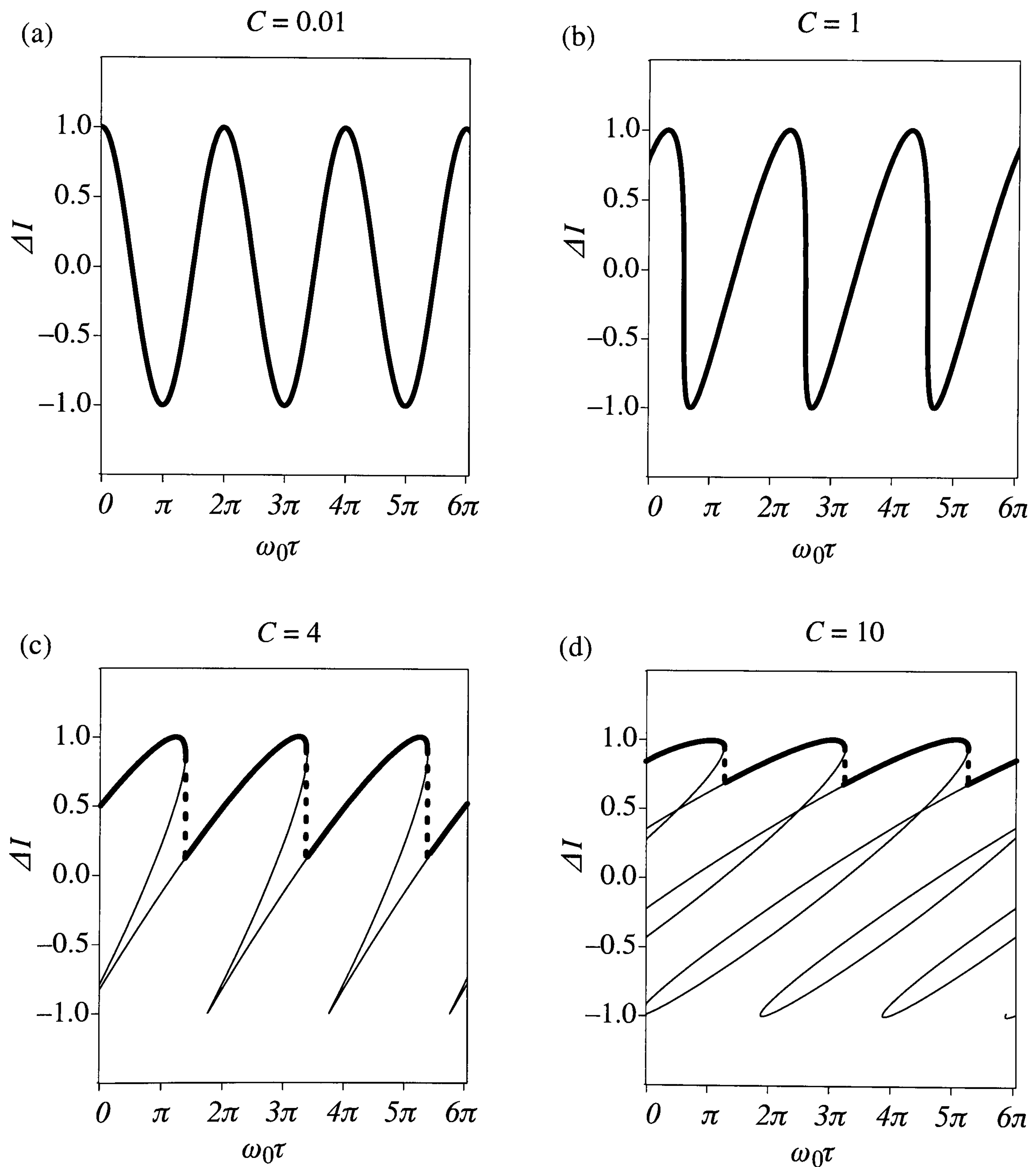

Fig. 14 ΔI against $\omega_0\tau$ for different values of C, with $b = 4$, normalized to $2\frac{\varkappa}{\tau_L}\frac{I_0}{G_0}$.

From this we can see that, after the approximations we have made, the change in intensity is linear with a change in the reflected signal from the specimen, which is proportional to $\varkappa$, where $\varkappa$ is given by

$$\varkappa = \frac{\left(1 - R_2{}^2\right) R_S}{R_2} \tag{75}$$

3.4 Conclusions

From the reflectivity model used in section 2 we showed that we can express the compound reflectivity at the coupling mirror of a HeNe laser as

$$R_2 + \left(1 - R_2^2\right) \eta \ |s| \ \mathrm{Re}\left\{e^{-j(\omega\tau - \phi)}\right\} \tag{76}$$

However, when a semiconductor laser is subject to feedback into the cavity we have seen that the internal laser dynamics are complex, due to the coupling between the frequency and intensity. For medium to high levels of feedback, certainly including the normal feedback range which a semiconductor laser experiences in the microscopes we will describe, we see that the coupling enables the laser mode to jump between closely spaced modes to nullify any variation in the phase of the signal re–entering the cavity. As a result the intensity variation caused by the feedback signal is solely dependent on the amplitude of the signal which is fed back, as shown in eqn (77).

$$R_2 + \left(1 - R_2^2\right) \eta \ |s| \tag{77}$$

Also the fluctuations in the intensity (due the variation of phase of the fedback signal) decrease as the feedback level increases. Hence, for medium to high levels of feedback, the change in intensity varies simply with the variation in amplitude of the reflected signal, and not its phase, as shown in eqn (74).

4. Laser Feedback: Optical Intensity Variation

4.1 Introduction

In Chapters 1 and 2 we saw how a monomode optical fibre can be used as a coherent detector and that a laser may used, in principle, in a reciprocal geometry, as shown in Fig. 15. In this chapter we consider the case of a semiconductor laser system and look at the performance of the laser under various feedback conditions. Using this understanding of the laser response we have constructed a simple confocal microscope.

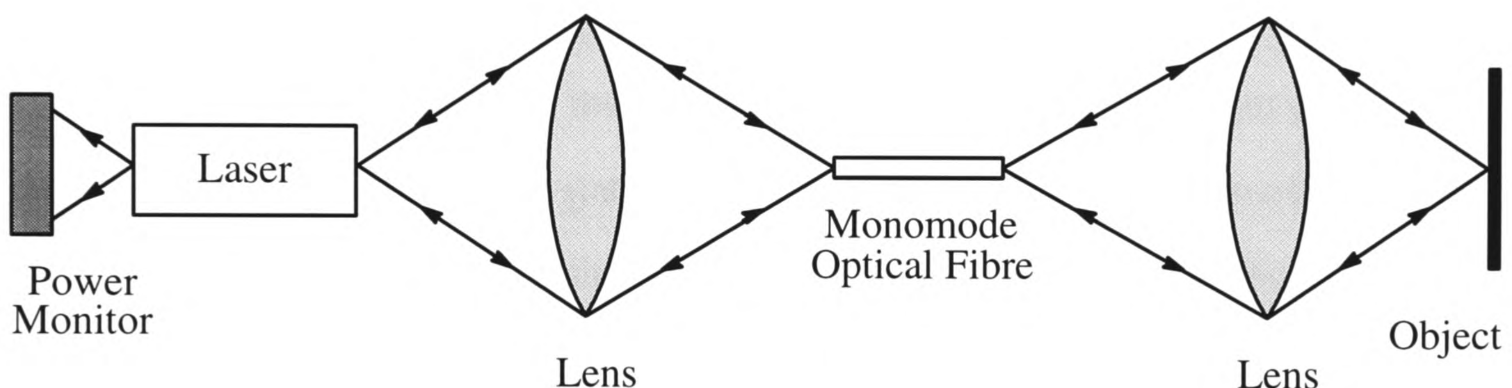

Fig. 15 Schematic Layout Of Microscope Optics.

We first provide a simplified model to predict the optical intensity within the laser cavity of a semiconductor laser using steady state equations. This enables us to understand how the emitted intensity at one port depends on the cavity mirror reflectivities. Using this, along with the compound cavity modelling in Chapter 3, we present results of modelling the response of the laser and the microscope and show that they are confirmed experimentally.

The noise properties of the system are illustrated experimentally and discussed in the light of the theory used to describe the laser.

Finally we present two images which demonstrate the confocal imaging capabilities of the system. Together they clearly display the depth discrimination typical of a confocal microscope.

4.2 Simplified Semiconductor Laser Theory

4.2.1 Introduction to Simplified Feedback Theory

In Chapter 3 we saw that, using dynamical laser equations, it was possible to describe the effect of optical feedback on the operation of a laser. For low levels of feedback ($C < 1$), the phase information of the fedback signal was conserved, but for higher feedback intensity the laser could operate in different modes and would jump between them in such a way as to keep the phase of the fedback signal as constant as possible. This is the case for semiconductor lasers. We also showed that, to a good approximation, the change in intensity in the laser cavity varies linearly with the change in amplitude of the fedback signal (eqn (74)).

However, we now wish to show that it is possible to obtain this final result using a much simpler analysis based on steady state equations [29]. As in Chapter 3 we start by considering the laser coupling mirror and the specimen as a compound mirror. We now need to derive the dependence of the cavity intensity on this compound reflectivity.

To justify this approach we recall that laser dynamics effects caused by the feedback have frequencies in the MHz to GHz range. However the bandwidths of our scanning microscope signal circuitry in most cases do not exceed 1MHz. It therefore seems reasonable to assume therefore that an averaged laser intensity would provide an acceptable approximation to the microscope signal, and hence the equations describing steady state generation (rather than dynamics) can be used.

4.2.2 Laser Intensity

We wish to express the light intensity reaching the photodiode, I_{out}, in terms of the unsaturated cavity gain, $2gL$, (where g is the gain coefficient of the laser and L is the laser cavity length), and the mirror amplitude reflectivities, R_1 and R_2.

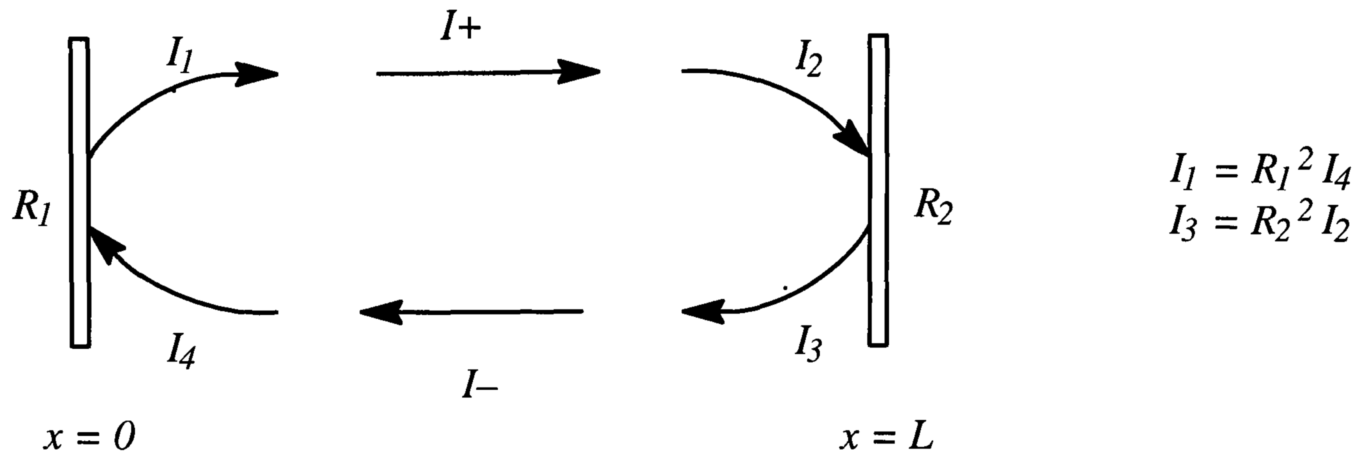

Fig. 16 Schematic diagram of intensity distribution inside a laser cavity.

The semiconductor laser is strongly output coupled so we use the following analysis, first performed by Rigrod [30]. From standard laser theory ([29] p 292 ff), the intensity gain $g(I)$ is as shown in (78), in which I is the total intensity at any point $0 < x < L$, ie $I = I_+ + I_-$, I_S is the saturation intensity and J is the normalized intensity ie $J = I / I_S$.

$$g(I) = \frac{g_0}{1 + \frac{I}{I_s}} = \frac{g_0}{1 + \frac{I_+ + I_-}{I_s}} = \frac{g_0}{1 + J_+ + J_-} \tag{78}$$

Since $\frac{1}{I}\frac{dI}{dx} = g$ we can write

$$\frac{1}{J_+}\frac{dJ_+}{dx} = -\frac{1}{J_-}\frac{dJ_-}{dx} = g \tag{79}$$

Also

$$\frac{d}{dx}\{J_+(x)J_-(x)\} = (g\ J_+)\ J_- - J_+(g\ J_-) = 0 \tag{80}$$

Hence we can see that

$$J_+(x)\ J_-(x) = K \tag{81}$$

where K is a constant.

Combining eqns (78), (79) and (81) gives

$$\frac{1}{J_+}\frac{dJ_+}{dx} = \frac{g_0}{1 + J_+ + J_-} = \frac{g_0}{1 + J_+ + \frac{K}{J_+}} \tag{82}$$

and

$$\frac{1}{J_-}\frac{dJ_-}{dx} = \frac{g_0}{1 + J_+ + J_-} = \frac{g_0}{1 + J_- + \frac{K}{J_-}} \tag{83}$$

When these are integrated, combined and simplified we obtain

$$2g_0L = 2J_2(1-R_2^2) + 2J_4(1-R_1^2) - ln(R_1R_2)^2 \tag{84}$$

We want to express J_4 as a function of R_2. First we remove J_2 by expressing it as a function of J_4, and we achieve this by evaluating eqn (81) at the boundaries which gives $J_2J_3 = J_1J_4$. This, combined with $J_1 = R_1^2J_4$ and $J_3 = R_2^2J_2$, gives $J_2 = \frac{R_1}{R_2}J_4$. Substitution into eqn (84), and further rearrangement leads to

$$J_4 = \frac{g_0L + lnR_1R_2}{\left(1 + \frac{R_1}{R_2}\right)(1 - R_1R_2)} \tag{85}$$

The intensity emitted towards the power monitor is

$$I_{out} = \left(1 - R_1^2\right)J_4 \tag{86}$$

Hence

$$I_{out} = \left(1 - R_1^2\right)I_S\frac{g_0L + lnR_1R_2}{\left(1 + \frac{R_1}{R_2}\right)(1 - R_1R_2)} \tag{87}$$

We are now able to substitute the expression for compound reflectivity for a semiconductor laser with optical feedback obtained in Chapter 3

$$R_2 + \left(1 - R_2^2\right)\eta\ |s| \tag{88}$$

for the variable R_2 in eqn (87). Thus we now have the output intensity in terms of the amplitude reflectivity of the specimen, $|s|$.

4.2.3 Predictions from the Model

When we substitute expression (88) for the variable R_2 in eqn (87) we can plot the Optical Power (I_{out}) against Injection Current (proportional to g_0) as shown in Fig. 17. For the other variables we used the parameters:

Length of laser cavity, $L = 250\mu m$

Cavity mirror amplitude reflectivities, $R_1 = R_2 = \sqrt{0.3} = 0.548$

Injection Current (mA) = 155 g_0

Output Power (mW) = 34 I_{out}

The values for L and R were chosen as typical for the type of semiconductor laser being used, while the constants of proportionality for the injection current and the output power were chosen to provide the best fit between the theoretical and experimental results shown in Fig. 17 and Fig. 20.

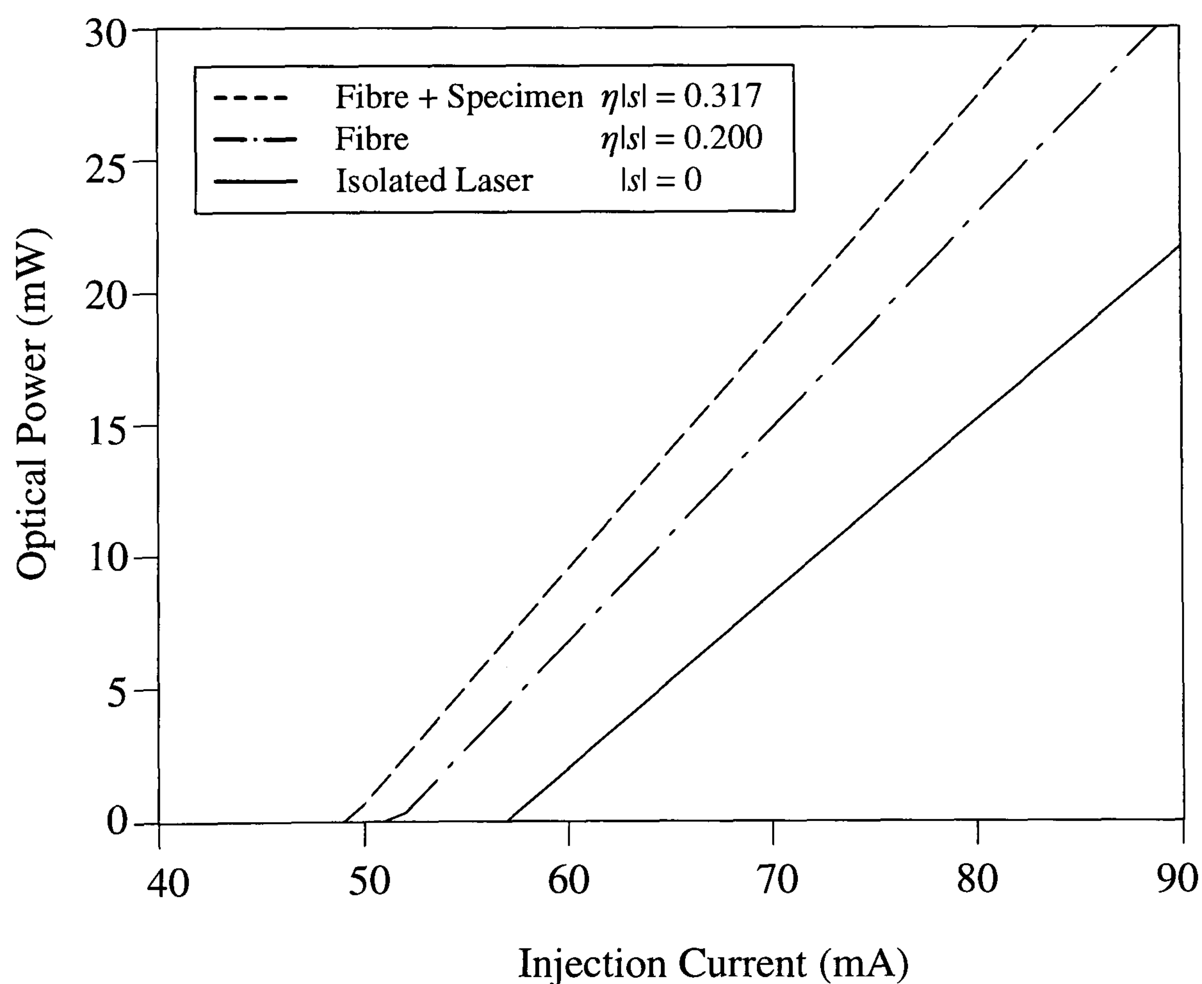

Fig. 17 Theoretical Prediction of Optical Power against Injection Current for 3 different reflectivities, ie $\eta|s| = 0.317$, 0.200 and 0, from left to right.

For the theoretical model we still need values for the amplitude reflectivity experienced by the laser. Up until now we have neglected to include in our model the effect of reflection from the input end of the optical fibre, just as we have neglected the reflection from the surfaces of the collimating lens. We have considered any effect from the intermediate optical components to be constant and have therefore treated them as part of the laser system, choosing to concentrate solely on the variable reflectivity of the specimen. At this point, however, we wish to test our model of the laser by comparing the different values for the laser threshold for different reflectivities in the external cavity, so we need to be more specific about which reflectivities are included in each case.

For the case of the "isolated" laser, when the specimen or mirror is removed from the microscope system, we still require a collimating lens to focus the signal onto a photodetector in order to measure the intensity variation of the laser as the injection current is scanned. The feedback from the reflection at the surface of this lens is neglected due to the curvatures of the laser wavefront and the lens, and any residual feedback effect is considered as a constant background. We therefore model this with $|s| = 0$.

We then look at the case of the laser coupled into a "free" fibre which is not output coupled to the microscope system, and consider the reflection from the surface at the input end and total internal reflection at the output end. We can therefore replace $\eta|s|$ with $|s'|$ which was measured as $|s'| = 0.200$.

Finally we measured the reflectivity when the laser was coupled into a fibre, the output of which was focussed onto a fixed plane mirror and reflected back to the laser through the fibre again. In this case we can replace $\eta|s|$ with $|s'| + \eta|s''|$, where s'' is the amplitude reflectivity at the surface of the mirror. This was measured to be 0.317.

The actual values for $\eta|s|$ were found by directly measuring the signal reflected from the fibre and fibre/specimen, relative to the signal strength of the isolated laser.

In Fig. 18 (a) and (b) we plot the theoretical dependence of the output power on reflectivity, according to eqn (87). This is done for both the threshold injection current (57mA) and the operating injection current (89mA). In the latter case a dc component of the output power (of 21.7mW) has been removed since it is only the change in output power due to the varying reflectivity in which we are interested. The most significant feature of these lines is that they are almost straight. This indicates that there is an almost linear relation between the reflected signal and the detected signal, as is also predicted by the dynamical laser theory in Chapter 3, eqn (66).

We note that this implies that the modulation of the power monitor signal is proportional to the amplitude of the reflected signal, $|s|$, which contrasts with conventional confocal systems, in which the image signal is proportional to the square of the amplitude of the reflected signal, $|s|^2$.

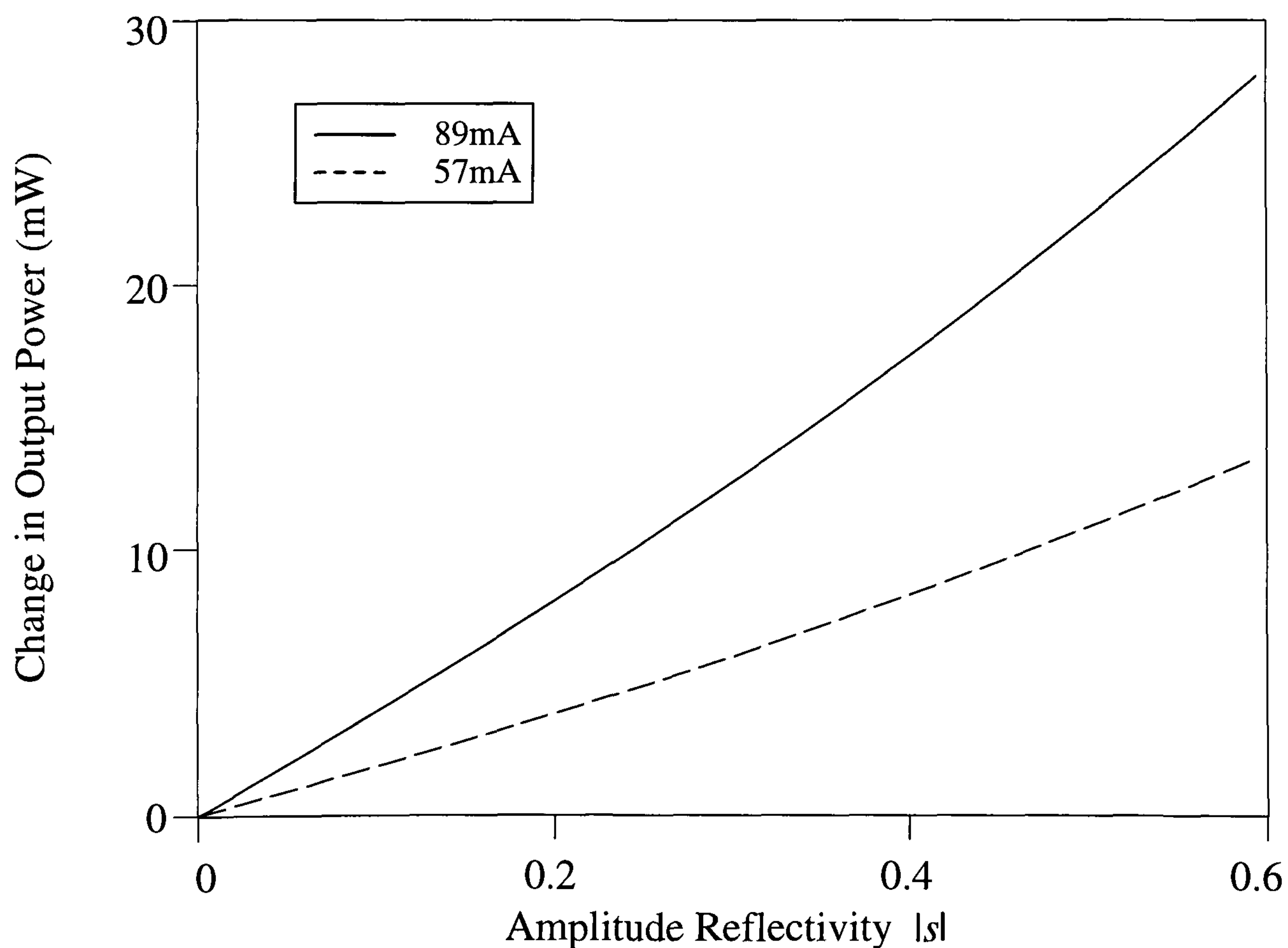

Fig. 18 Dependence of output power on specimen reflectivity for constant injection current (a) Threshold Current 57mA, (b) Operating Current 89mA.

To obtain a prediction of the axial response of the system we finally substitute into eqns (87) and (88) the expression for the confocal amplitude response of the specimen as it is scanned axially, $s(u)$, (calculated in Chapter 2 (eqn (38)). The result is plotted in Fig. 19 with two different values of the fill factor, a (0 and 1.5), which models the effect of the finite size of the source and detector, as we saw in Chapter 2. In the limiting case, when the amplitude point spread function of the system, h, is much broader than the eigenmode of the laser, e, a tends to zero and the axial response may be written as $s(u) = \text{sinc}(u/2)$, where u is, as usual, a measure of defocus.

Fig. 19 also shows the reduction in depth discrimination which results from a non–zero value of a, which correspond to cases where the point spread functions are not broad compared with the mode profile.

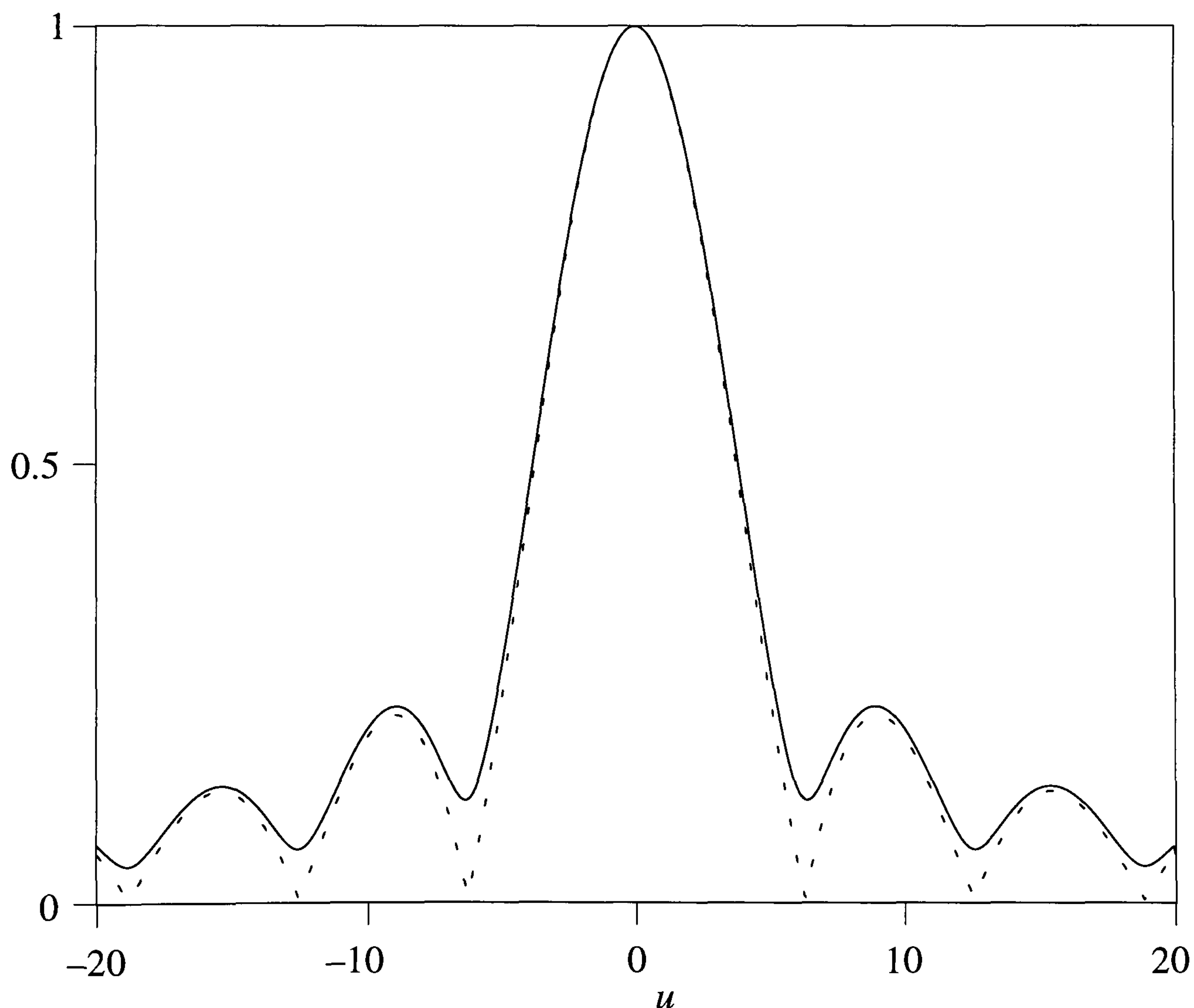

Fig. 19 Normalised axial responses of semiconductor laser detection microscope: $C \gg 1$, solid line: a = 1.5, broken line: a = 0.

For reasonably small feedback signal levels (although sufficient to cause coherence collapse, ie $C \gtrsim 50$) these curves are approximated as $\left|\mathrm{sinc}\left\{\frac{1}{2}\left(u + \frac{ja}{2}\right)\right\}\right|$. This is not surprising since we have seen in Fig. 18 that the theory predicts that the microscope signal detected by the laser and measured from the back laser port is virtually linear with the amplitude reflectivity from the specimen.

4.3 Experimental Results for the Semiconductor Laser Microscope

4.3.1 Characteristics of the Laser with Feedback

We undertook some preliminary experiments to investigate the laser behaviour at different injection current levels. The laser we used was a Sharp LT015MDO laser diode which operated at 829nm and gave a maximum power from single output of 22mW at an operating injection current of 89mA. It was driven by a Liconix LDD–200 power supply module.

To produce the curves shown in Fig. 20 we used an external ramping signal to control the injection current, and measured the optical power using the power monitor. The results shown are the superposition of three separate curves. In the first case the laser was isolated to minimize feedback, which gave the right hand curve, showing the natural characteristic of the laser, with a threshold current of about 57mA.

In the second case the laser was coupled into a fibre which was not output coupled onto a reflector. This increased the intensity generated by the laser and reduced the threshold current to 52mA. In the third case a mirror was included as a specimen in the microscope arrangement and the threshold current was reduced to 49mA. During this time the specimen translator was held stationary in the position which gave maximum reflected signal.

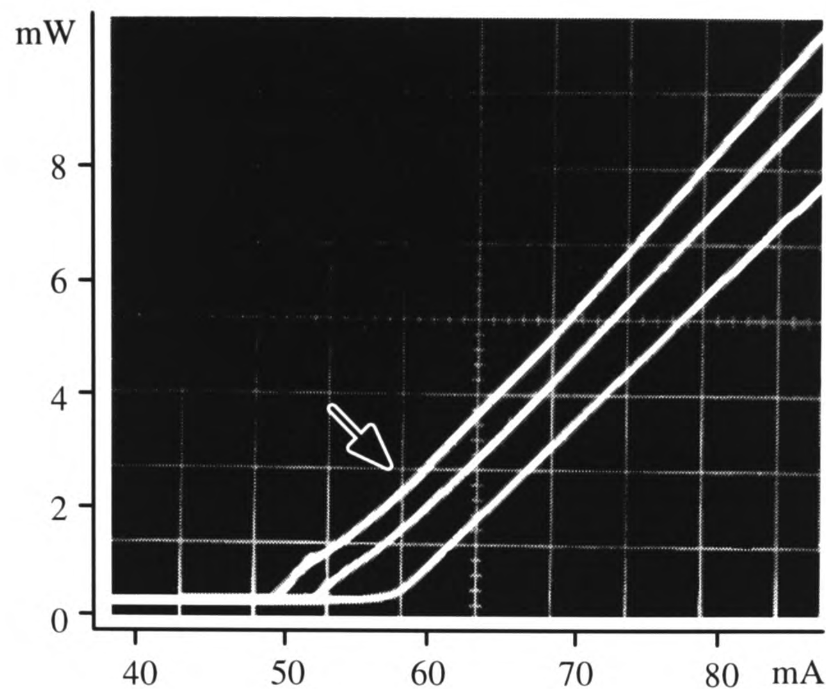

Fig. 20 Laser power against injection current.
Right hand trace – isolated laser,
Central trace – laser with feedback signal reflected from a fibre,
Left hand trace – laser with feedback signal reflected from a fibre and mirror.

This is in excellent agreement with the form of the theoretical curves discussed earlier and shown in Fig. 17.

A significant feature of the experimental characteristic with feedback (the left hand line) is the characteristic kink (marked by an arrow) which is not shown in Fig. 17. This occurs when the injection current becomes approximately equal to its threshold value in the case of the isolated laser. It is believed [21] that this kink marks the transition from coherent external cavity–locked operation to the coherence collapse state. For the feedback levels involved our system, it seems that the semiconductor laser we used was in coherence collapse mode for injection currents above 57mA. Above this current the laser intensity increased linearly with a gradient slightly greater than that for the isolated laser, which implies that the microscope signal should increase with current as well. This is also predicted by eqn (87), as discussed earlier.

4.3.2 The Response of the Microscope

The curve in Fig. 21 is an axial response obtained with the semiconductor laser run at maximum operational current 89mA.

The response is remarkably close to that calculated for $a = 1.5$ using eqns (88) and (87), thus providing a strong support to the model used in the theoretical section. The distance between the first maxima, 6.2μm, matches the value predicted by an idealised $\left|\operatorname{sinc}\left\{\frac{1}{2}\left(u + \frac{ja}{2}\right)\right\}\right|$ axial response function for a 0.5 NA objective lens and indicates the high quality of the Leitz microscope objective used.

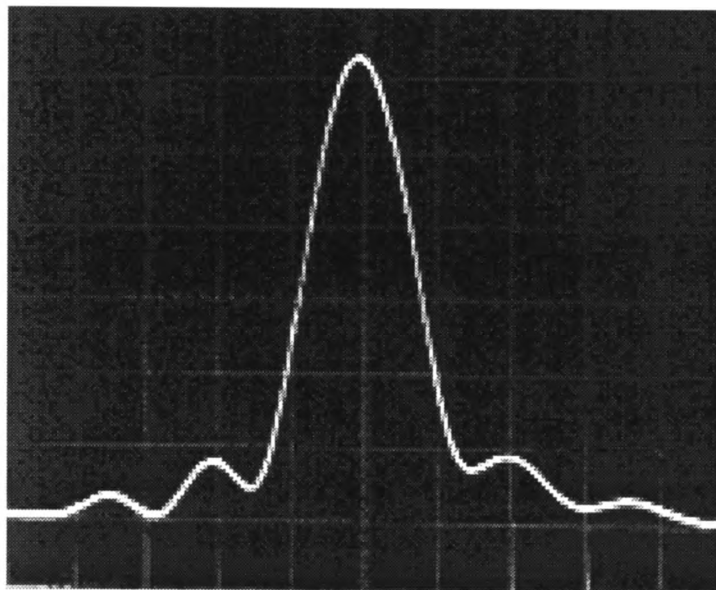

Fig. 21 The axial response of the semiconductor laser based microscope, injection current = 89mA. Vertical scale: 0.53mW / division, horizontal scale: 2.1μm / division.

We also undertook a direct experiment to prove that the microscope signal is approximately proportional to the amplitude, rather than the intensity, of the feedback signal (indirect proof is, of course, the shape of the axial response in Fig. 21). The microscope signal was monitored while the coupling efficiency η was decreased by misaligning the fibre coupler. The signal amplitude was then plotted against the coupling efficiency which is shown in Fig. 22 where a reasonable fit to the curve calculated from the eqns (87) and (88) was obtained. The theoretical curve itself is almost a straight line in this case, since the feedback signal is fairly weak.

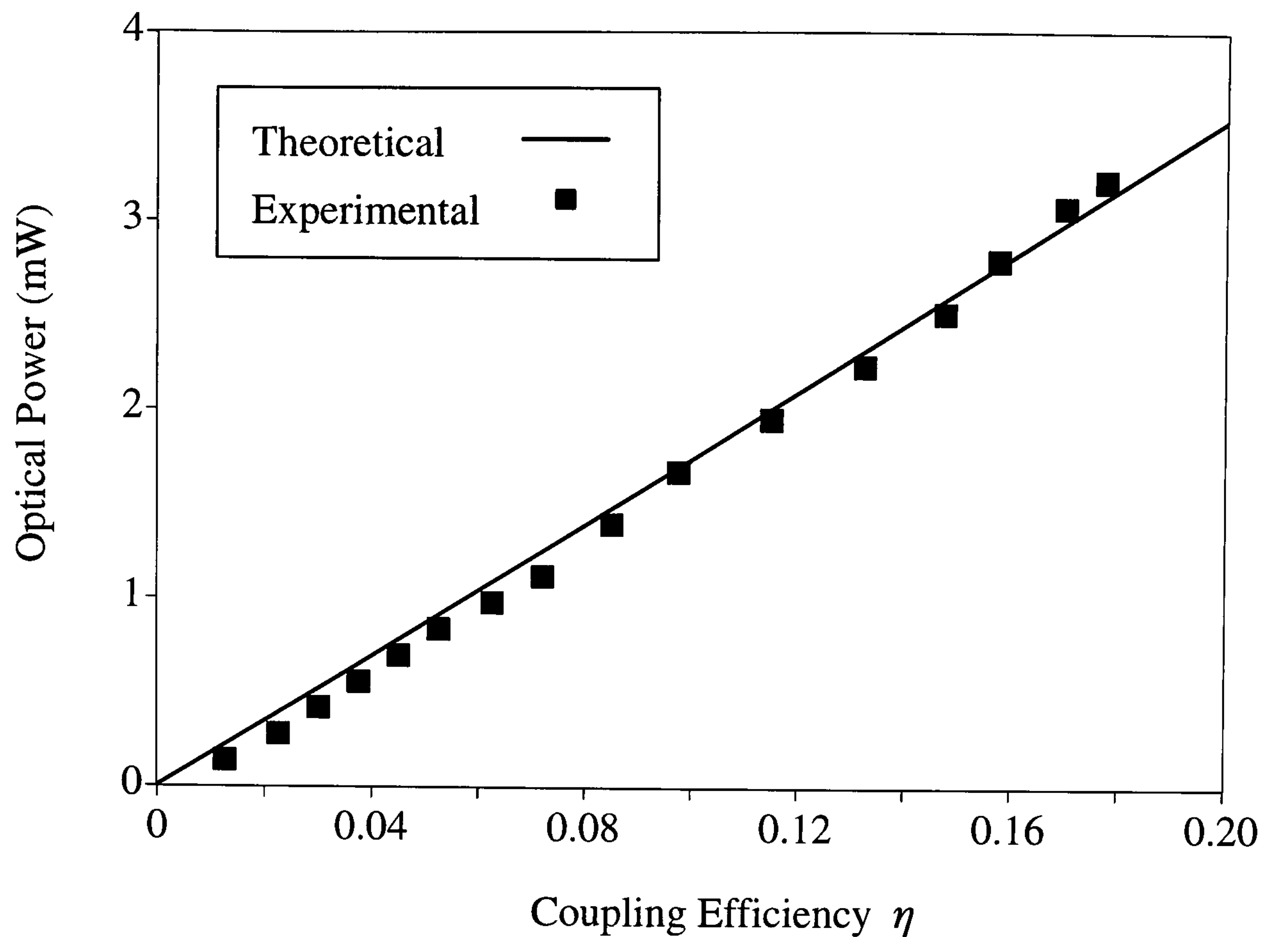

Fig. 22 The Theoretical correspondence with the Experimental results for Optical Power against Coupling Efficiency.

4.3.3 Noise Characteristics

We went further to investigate the microscope signal at lower current levels and took the curve in Fig. 23(a) just above threshold (for the feedback system) at about 55mA. The signal, as compared to the previous one, is noisy and, more important, the noise character differs for different feedback levels. This can be understood with reference to the description of the operation of a semiconductor laser under feedback conditions given in Chapter 3.

While the reflector is far from the focal plane, the feedback signal is very weak and the laser appears to operate coherently in one of the external cavity modes. Since the reflector is scanned, the external cavity parameters change continuously and the laser hops from mode to mode (each of which is a perturbation of an external cavity mode) producing the characteristic pattern visible at the wings of the axial response in Fig. 23(a).

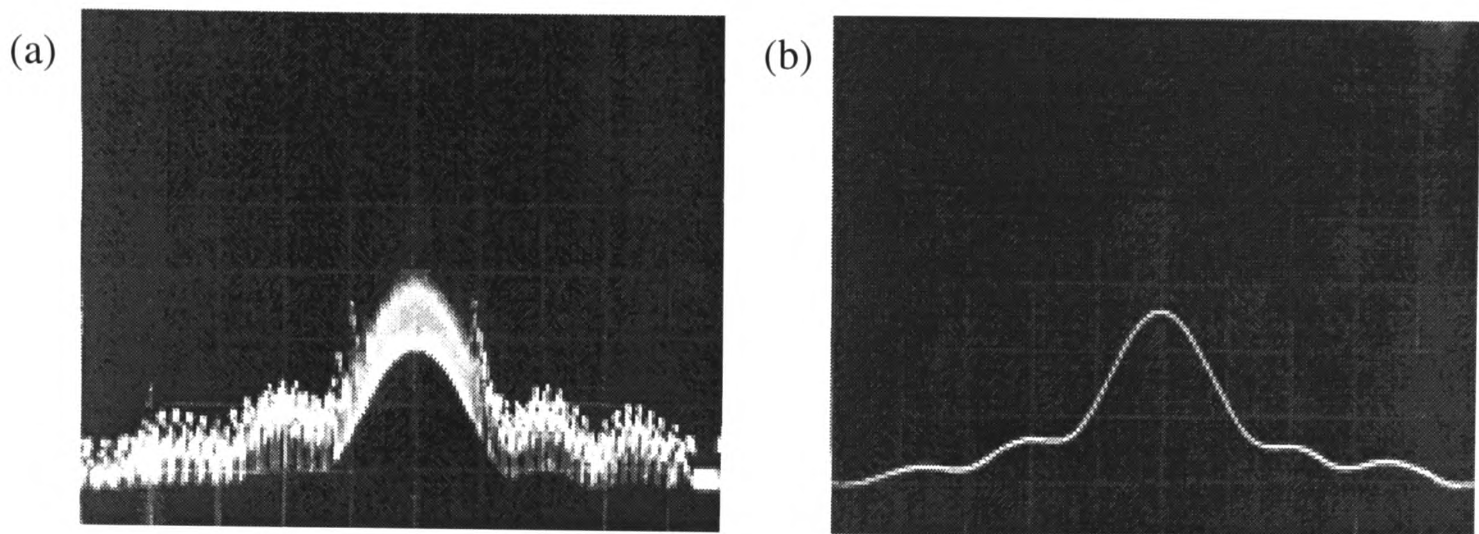

Fig. 23 (a)Different types of noise observed in the microscope run just above threshold, (b) – the averaged response. Vertical scale: 0.53mW / division, horizontal scale: 2.1μm / division.

This noise clearly displays a periodicity which corresponds to $\lambda/2$ (or 2π in Fig. 14). This clearly implies that the laser is hopping between external cavity modes as the external cavity length is changing. To understand better what is happening here it is instructive to look at an expanded view of such a period, as shown in Fig. 24. Here it is possible to observe the many transitions which take place between the different phase–stable solutions of eqn (72). (Eqn (72) relates the change in intensity due to laser feedback to the round–trip period in the external cavity, which is proportional to the cavity length).

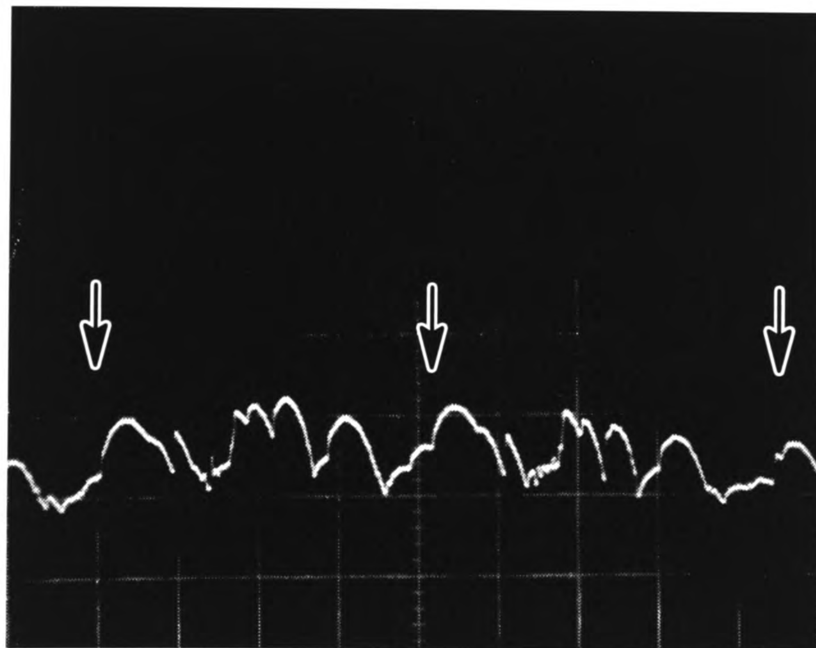

Fig. 24 A magnified view of the periodic noise shown for low feedback levels in Fig. 23 Vertical scale: 0.53mW / division, horizontal scale: 0.1μm / division.

Two complete periods are visible, marked by arrows, and it is clear that the transitions between different phase–stable states appear to take place at corresponding points in each

cycle. This is considered to be due to the presence of other instabilities which make the system particularly vulnerable to transitions initiated by spontaneous emission noise [26].

As the reflector moves toward the focus and the feedback intensity increases, the noise abruptly becomes wideband, indicating the transition to the coherence collapse state. The noise averaged response in Fig. 23(b) also differs substantially from Fig. 21 by exhibiting more pronounced sidelobes. This can be explained as a consequence of the kink in laser injection characteristics shown in Fig. 20. This shows that small feedback signals failing to reach coherence collapse threshold are relatively enhanced.

The microscope performance is rather unusual in the injection current range between the thresholds of the feedback and isolated cases. This is because in this case the laser only generates when the object is sufficiently close to focus to reflect a signal sufficiently strongly to bring the laser above threshold. Naturally this results in a much reduced (and variable) depth of field and the absence of the secondary maxima. Fig. 25 shows the averaged display obtained when the microscope was operated 2mA below the threshold current of the isolated laser, and illustrates clearly the feedback amplitude discrimination performed by laser.

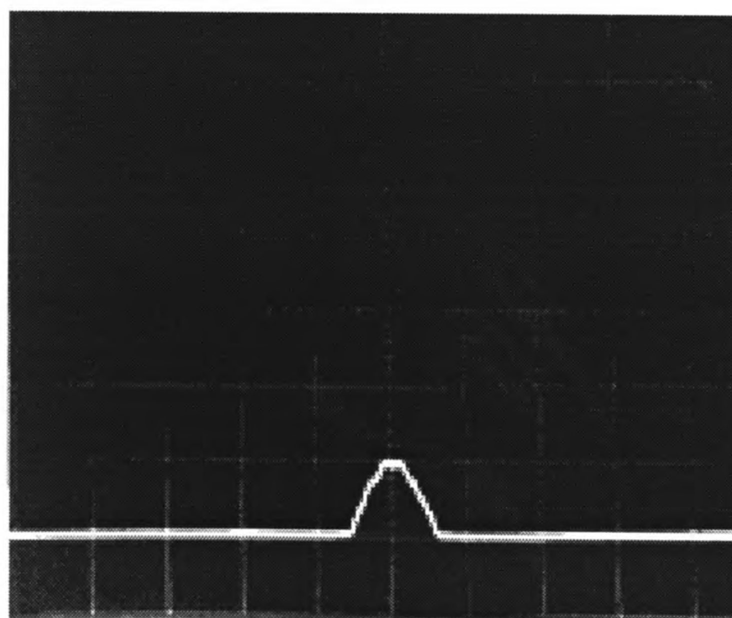

Fig. 25 The averaged axial response when the laser is operated 2mA below threshold. Vertical scale: 0.53mW / division, horizontal scale: 2.1μm / division.

When we look at the noise on this signal, shown in Fig. 26, we see that it is of the semi–periodic kind, rather than the wideband kind shown in the centre of Fig. 23(a). This is clearly due to the particularly low level of feedback, even when the object is in focus: a level which corresponds to the out–of–focus signal shown at the sides of Fig. 23(a).

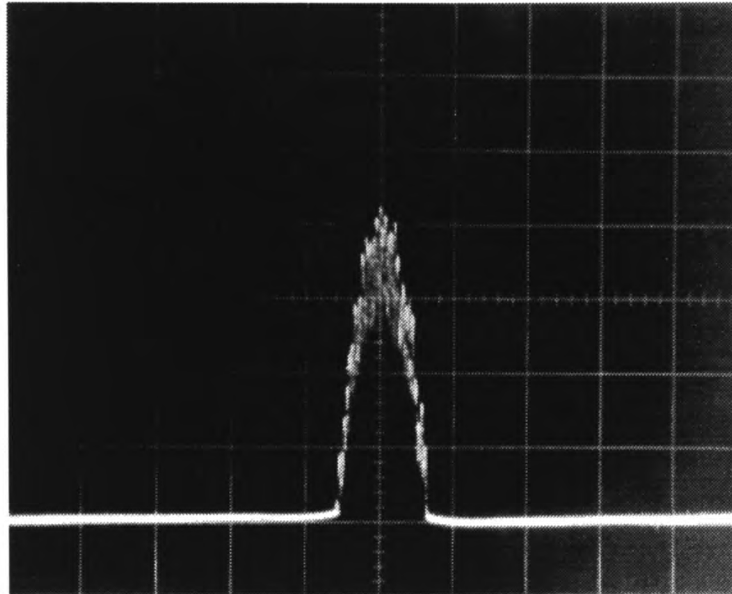

Fig. 26 The raw axial response when the laser is operated 2mA below threshold. Vertical scale: 0.17mW / division, horizontal scale: 2.1μm / division.

4.3.4 Imaging Capability

Finally, we took a through–focus set of images of a semiconductor chip. Two of these images with an axial separation of about 3 μm are shown in Fig. 27. These images do not differ considerably from the images obtained by a scanning microscope using traditional signal detection techniques (see, for instance, [8]).

It therefore seems clear that, despite some of the imaging peculiarities discussed above, the microscope using semiconductor laser detection, can perform all the functions of a confocal scanning microscope, including optical sectioning, height detection and extended focus.

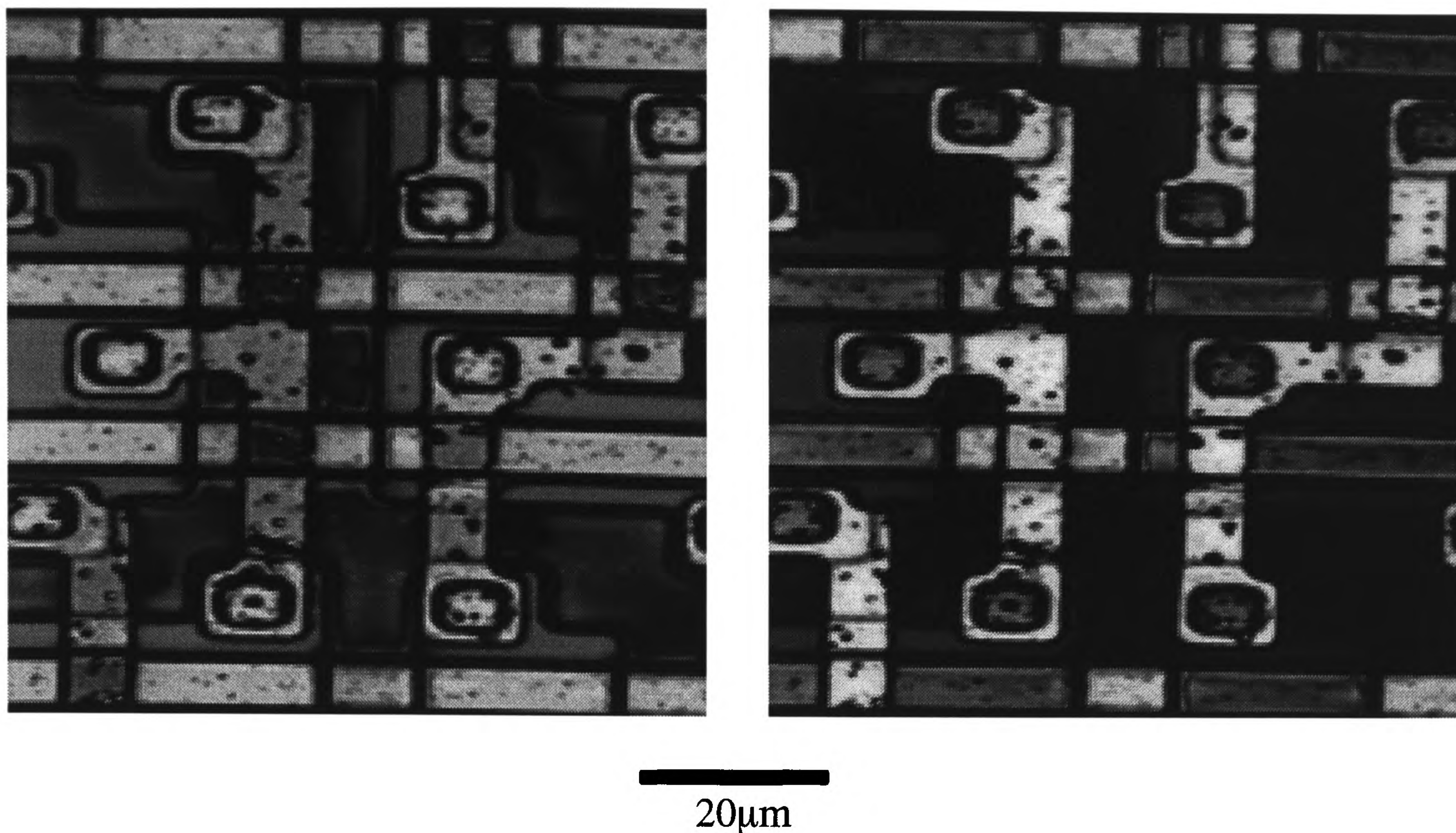

Fig. 27 Two specimen images taken at 3μm axial separation.

4.4 Conclusions

In this chapter we have shown the theoretical basis for and experimental viability of a new scheme of confocal scanning microscope. In this scheme the light reflected from the specimen is permitted to re–enter the laser cavity and change the generation intensity which is then used as the microscope signal. Using a semiconductor laser we have demonstrated complex behaviour including coherence collapse induced by strongly coupled external reflections. Within this regime, however, the laser produced a predictable signal proportional to the object amplitude reflectivity, but insensitive to the phase of the detected lightwave. We used this configuration to obtain images similar to those provided by a traditional confocal microscope.

Such a semiconductor laser feedback microscope is an attractive scheme for a simple and rugged scanning microscope perhaps based on a prefabricated pigtailed laser module.

5. Laser Feedback: Junction Voltage Variation

5.1 Introduction

In Chapter 4 we considered a reciprocal arrangement microscope in which the image signal is fed back into the laser cavity. The signal is then obtained by measuring the resulting small variation of optical intensity emitted by the semiconductor laser. This reciprocal arrangement removes the need for a beam splitter, which was previously required to divert some of the reflected signal to a photodiode. Using such a reciprocal arrangement also significantly simplifies the alignment of the system. However it still requires access to the second port of the laser and the use of a separate photodiode. In this chapter we therefore investigate the possibility of simplifying the detection technique further, such that no external photodiode is required. Instead we measure the image signal as a perturbation of the laser diode junction voltage while the diode is operated at constant injection current.

First we discuss the optical system and show that the reciprocal detection by the single mode optical fibre which was used in Chapter 4 can be carried out by the single transverse mode of the laser itself. As a result of this simplification we are now able to consider a very simple and compact reciprocal confocal microscope consisting merely of a semiconductor laser and lens system as illustrated schematically in Fig. 28. We demonstrate theoretically that the change in junction voltage of the laser is proportional to the change of the optical intensity within the laser cavity, and hence that the laser can be used as a detector itself.

This new scheme is then investigated experimentally. First we confirm a number of predictions of the theory including the differential resistance of the diode and the relationship of the variation in the junction voltage to the intensity reflectivity of the specimen. Next we investigate the spatial filtering action of the laser and present axial scans which are well modelled by the theory. Finally we present images obtained with this new system.

5.2 The Optical System

We consider the scanning optical microscope system shown in Fig. 28 where the light reflected from the specimen is permitted to re–enter the laser cavity. The image signal is detected as a perturbation of either the power monitor signal or the laser diode junction voltage.

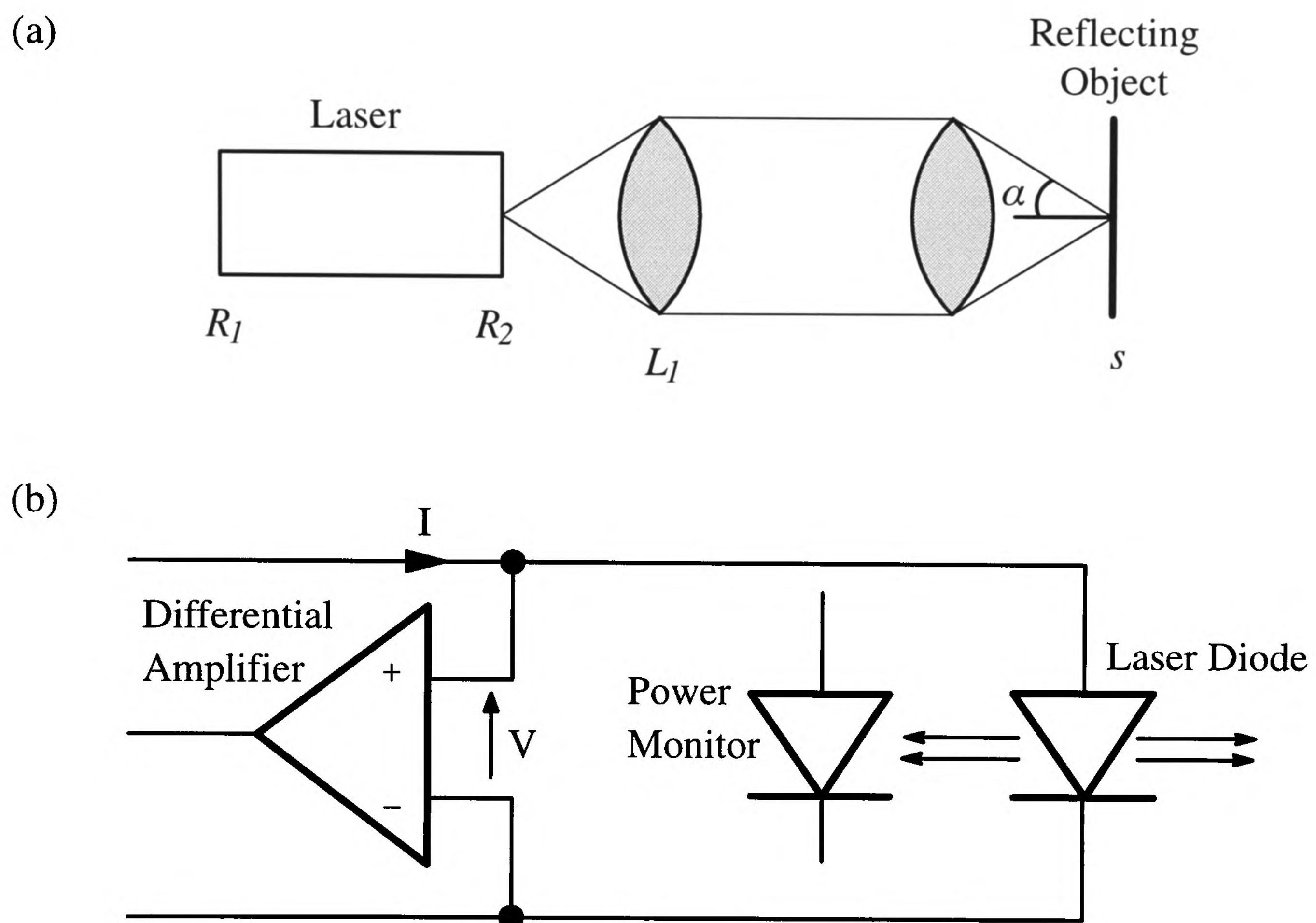

Fig. 28 (a) Schematic layout of the laser diode microscope.
(b) Schematic diagram of the power monitor and diode voltage detection schemes.

In the schematic optical arrangement shown in Fig. 28 (a) no optical fibre has been used. This is because the laser, which is designed to operate with only one transverse mode, has been shown capable of performing the same reciprocal detection function as was originally performed by the monomode fibre [14]. The spatial filtering action between the field reflected from the specimen and the single mode of operation of the laser ensures confocal operation. This is explained by the fact that only the part of the reflected field that matches the lasing mode modulates the laser generation. We demonstrate this later when we present

axial responses for different collimating lenses (L_l) in Fig. 29 (theory) and Fig. 33 (experiment).

The signal measurement options we used are schematically illustrated in Fig. 28 (b) where it can be seen that we could measure both the change in junction voltage and in optical intensity simultaneously, for a constant injection current.

5.3 Theory

5.3.1 Laser power

In Chapter 4 we derived an expression for the laser output intensity in terms of the reflectivities of the laser cavity mirrors, the gain of the lasing medium and the saturation intensity. However we now wish to consider how the junction voltage of the semiconductor laser varies with the optical intensity within the laser cavity. We therefore choose to consider the laser intensity as photon density and the junction voltage in terms of electron density.

Although we could simply use the cavity intensity dependence on the amplitude of the signal reflected from the object which we derived using the dynamical laser equations in Chapter 3, we wish to show that the same result can be obtained using only the rate equations for electron density in the excited state (N) and photon density (i) in the active region. [29,31].

$$\frac{dN}{dt} = \frac{j}{dq} - \frac{N}{\tau_s} - G(N)i \tag{89}$$

$$\frac{di}{dt} = G(N)i - \frac{i}{\tau_{ph}} \tag{90}$$

where j is the injection current density, τ_s is the spontaneous lifetime of the excited electrons, τ_{ph} is the photon lifetime, and $G(N)$ is the gain per unit time, which is itself a function of carrier density N. We have assumed that all the mode energy is in the active region which has thickness d. q is the charge on an electron.

If we denote the steady state values of these variables in the absence of optical feedback by the subscript zero we obtain directly from eqns (89) and (90)

$$\frac{j_0}{dq} - \frac{N_0}{\tau_s} - G_0 i_0 = 0 \tag{91}$$

and

$$G_0 - \frac{1}{\tau_{ph0}} = 0 \tag{92}$$

The photon lifetime in the cavity, τ_{ph}, is determined, inter alia, by the cavity mirror reflectivities and to find the dependence we need to separate the effect of the losses through the mirrors from the other losses which contribute to the brevity of the photon lifetime. This is easiest to derive using the integral solution to a form of the intensity rate equation

$$I = I_0 \, e^{(G(N)-\sigma)t} \tag{93}$$

where σ describes the losses in the laser cavity. After one complete round–trip within the cavity, in a steady state, this becomes

$$I_0 = (R_1 R_2)^2 I_0 \, e^{(G(N)-\sigma)\tau_L} \tag{94}$$

where R_1 and R_2 are the amplitude reflectivities of the cavity mirrors, and τ_L is the round–trip time within the laser cavity. From this, and eqn (92), it is easy to show that, in the steady state

$$\frac{1}{\tau_{ph0}} = \sigma + \frac{2}{\tau_L} \ln\left(\frac{1}{R_1 R_2}\right) \tag{95}$$

When part of the laser radiation is reflected back to the cavity the result is to increase the effective reflectivity of one of the cavity coupling mirrors and hence to increase the photon lifetime from τ_{ph0} to τ_{ph1} . By assuming that the mirror reflectivity R_2 has increased to $R_2 + r$, and linearising, we can express the change as

$$\frac{1}{\tau_{ph1}} = \frac{1}{\tau_{ph0}} - \frac{2r}{\tau_L R_2} \tag{96}$$

In order to analyse this change we need to solve eqns (89) and (90) subject to this variation in τ_{ph}. Typically the lifetime τ_s is measured in nanoseconds whereas τ_{ph} is usually a few

picoseconds. This implies that the photon population will respond quickly to any changes whereas the excited electron carrier density relaxes far more slowly. If, however, the rate of change of τ_{ph} is slower than τ_s then we may use the steady state form of eqns (89) and (90). In our case of relatively slow specimen scanning this assumption is valid.

If we further assume that all the other variables increase by a small amount such that we can write $N = N_0 + \Delta N, j = j_0 + \Delta j$ and so on, it is straight forward, in the steady state regime, to obtain from eqns (89) and (90) together with eqns (91), (92) and (96).

$$\frac{\Delta j}{dq} - \frac{\Delta N}{\tau_s} - G_0 \Delta i - A\ \Delta N\ i_0 = 0 \tag{97}$$

$$A\ \Delta N + \frac{2r}{\tau_L R_2} = 0 \tag{98}$$

where we have ignored the product of small quantities and have used the definition

$$\Delta G = \frac{dG}{dN}\ \Delta N = A\ \Delta N \tag{99}$$

where A is referred to as the differential gain slope of the laser. It is now straight forward for the case of constant injection current density ($\Delta j = 0$) to solve these two equations to yield

$$\Delta i = \frac{2r}{A\ dq G_0^2 \tau_L R_2 N_0}\left[\left(G_0 - N_0 A\right) j_{th} + N_0 A j_0\right] \tag{100}$$

where we have introduced the threshold current density $j_{th} = \frac{dq\ N_0}{\tau_s}$. This now permits us to calculate the change in laser power (proportional to Δi) from a given change in coupling mirror reflectivity, r, for a constant injection current.

5.3.2 Specimen Reflectivity

In Chapter 3 we showed that, for a semiconductor laser, the effective, compound reflectivity of the coupling mirror is as shown in expression (72). However, in the present case, we can dispense with the fibre coupling factor, η, since we no longer have an optical fibre in the arrangement. Therefore the contribution from the specimen to the effective reflectivity at a cavity mirror is given by

$$r = \left(1 - R_2^2\right)|s| \tag{101}$$

Thus we conclude that if we measure the image signal via a power monitor diode we will obtain a signal proportional to Δi and hence to $|s|$. The expression for s was derived in Chapter 2 as eqn (38)

$$s = \operatorname{sinc}\left\{\frac{1}{2}\left(u + \frac{ja}{2}\right)\right\} \exp\left(-2j\,k\,z\cos^2\frac{\alpha}{2}\right) \tag{102}$$

To illustrate the importance of the parameter a, which describes the coupling between the lens system and (in this case) the laser mode, we have plotted the normalized optical intensity (which from eqns (100) and (101) we know is proportional to $|s|$, which can be obtained from eqn (102)) against defocus (u) for three different values of a which were chosen to correspond to the results obtained experimentally later. These are shown in Fig. 29.

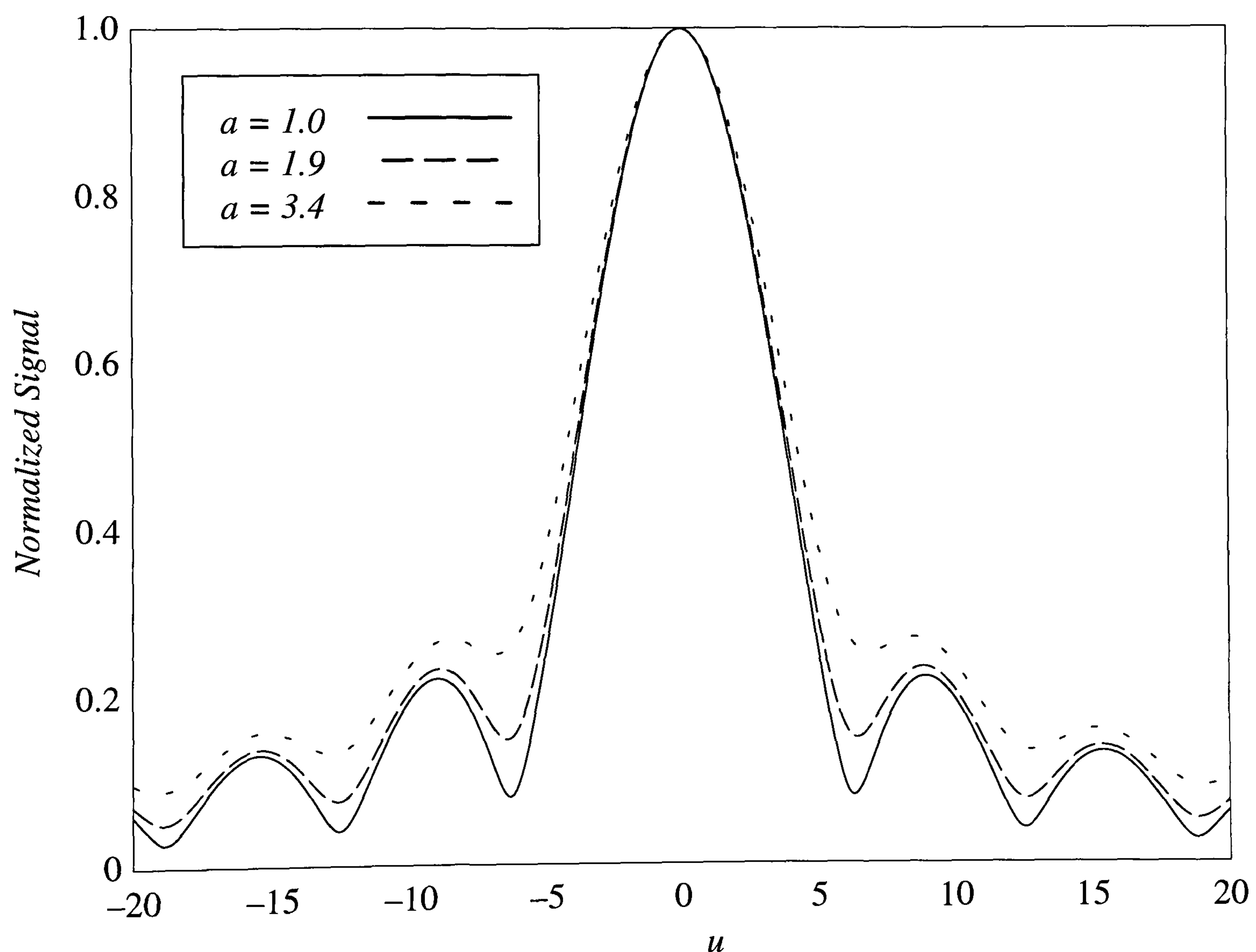

Fig. 29 Theoretical axial responses for various values of a

We will discuss experimental axial responses later (Fig. 33) which are presented to demonstrate the spatial filtering action of the laser mode and thus its confocal behaviour.

5.3.3 Junction voltage

We now turn our attention to the junction voltage signal. The junction voltage V is related to the carrier density N by [32]

$$N = N_i \exp\frac{qV}{2kT} \tag{103}$$

where N_i is the intrinsic carrier density, k is the Boltzman constant and T is the temperature. The $qV/2kT$ dependence is reported to be a good approximation for GaAs devices. In response to a small change of ΔN in carrier density we can write the change in junction voltage, ΔV, as

$$\Delta V = \frac{2kT}{q}\frac{\Delta N}{N_0} \tag{104}$$

and, after substitution of the expression for ΔN from eqn (98), we obtain

$$\Delta V = -\frac{4kT}{AqN_0\tau_L}\frac{r}{R_2} \tag{105}$$

It is important to note here that the carrier density N_0 does not depend on injection current above threshold. The junction voltage signal is therefore proportional to the feedback signal, r, alone, whereas the laser intensity signal, ΔI, increases with injection current density, j_0, according to eqn (100). Nevertheless, at a particular value of injection current density the signals derived from both the power monitor, eqn (100), and the diode voltage, eqn (105), are proportional to $|s|$ and so both signal detection techniques should yield comparable images.

We shall now use eqns (100) and (105) to obtain an expression for the diode differential resistance ϱ, since this is a readily measurable parameter and will permit us to compare the power monitor and diode voltage signals directly. It is given, below threshold, by [29]

$$\varrho = \frac{2kT}{qJ} \tag{106}$$

where J is the injection current, which is equal to the injection current density, j_0, multiplied by the diode junction area, a. The injection current density is in turn related to the carrier density at or below threshold, eqn (91) as $\frac{dqN_0}{\tau_s}$.

Another common laser characteristic is an efficiency ξ, defined by $\xi = \frac{dP}{dJ}$, where P is the lasing power which is proportional to the photon density, i, say $P = \varepsilon\, d\, a\, i$. Hence we can write

$$\xi = \frac{\varepsilon}{qG_0} \tag{107}$$

We can combine these parameters with eqns (100) and (105) as follows. Consider eqn (100) at threshold ie $j_0 = j_{th}$.

$$\Delta P = \frac{2\varepsilon da}{AG_0^2\tau N_0} \cdot \frac{r}{R_2} . G_0 \frac{j_{th}}{dq} \tag{108}$$

We can now substitute for r/R_2 (from eqn (105)) and j_{th} to obtain

$$\Delta P = \frac{2\varepsilon da}{AG_0\tau N_0} \cdot \frac{-\Delta VAqN_0\tau}{4kT} \cdot \frac{N_0}{\tau_s} = -\frac{\varepsilon daN_0}{\tau_s G_0} \cdot \frac{q}{2kT} \cdot \Delta V \tag{109}$$

However, from eqn (106)

$$\varrho_{th} = \frac{2kT}{qJ_{th}} \tag{110}$$

Hence

$$\Delta P = -\frac{\varepsilon}{qG_0} \cdot \frac{1}{\varrho_{th}} \cdot \Delta V \tag{111}$$

This gives

$$\Delta V = -\frac{\varrho_{th}}{\xi} \Delta P \tag{112}$$

where ΔP is the lasing power increase due to the feedback and ϱ_{th} is the diode differential resistance at threshold. The physical meaning of the eqn (112) is clear: when the laser power is increased by optical feedback, the change in junction voltage can be thought of as the equivalent voltage drop across the junction which would result from the increased injection current which would be required to give the same increase in laser power in the absence

of feedback. As an estimate, if we take typical values [29] for the differential diode resistance ϱ of 1Ω and the efficiency ξ = 1mW/mA then, eqn (112), predicts the diode junction voltage will decrease by 1mV per mW of laser power increase, ΔP.

5.4 Experimental Results

5.4.1 Semiconductor Laser Characteristics

For the research described in this chapter we used, once again, a Sharp LT015MDO laser diode which operated at 829nm and gave a maximum power from single output of 22mW at an operating injection current of 89mA. This was driven by a Liconix LDD–200 power supply module which has an integral power monitor which we employed to detect the optical power changes due to feedback.

Using the experimental arrangement of the diode laser described in section 5.2 (Fig. 28), we measured the differential resistance of the laser over the whole range of operational injection currents (both above and below the threshold). This was done by modulating the injection current at 10kHz with a constant amplitude, and monitoring the magnitude of the resulting junction voltage modulation. The results of this are shown in Fig. 30.

As can be seen the differential resistance reduces in a uniform manner with injection current until the threshold current is reached. At this point there is a noticeable kink as the resistance drops to a constant value. It is well known that the differential resistance of the laser diode junction is zero above threshold since any carrier density increase due to increased injection current is drained by the corresponding increase in lasing power. We conclude therefore that the residual constant resistance, ϱ_s = 1.8Ω, is in fact the series resistance of the wiring and the semiconductor chip. With this assumption the differential resistance follows closely a theoretical curve given by the eqn (106), which is also superimposed on the data in Fig. 30. The value of ϱ at threshold is 0.7Ω.

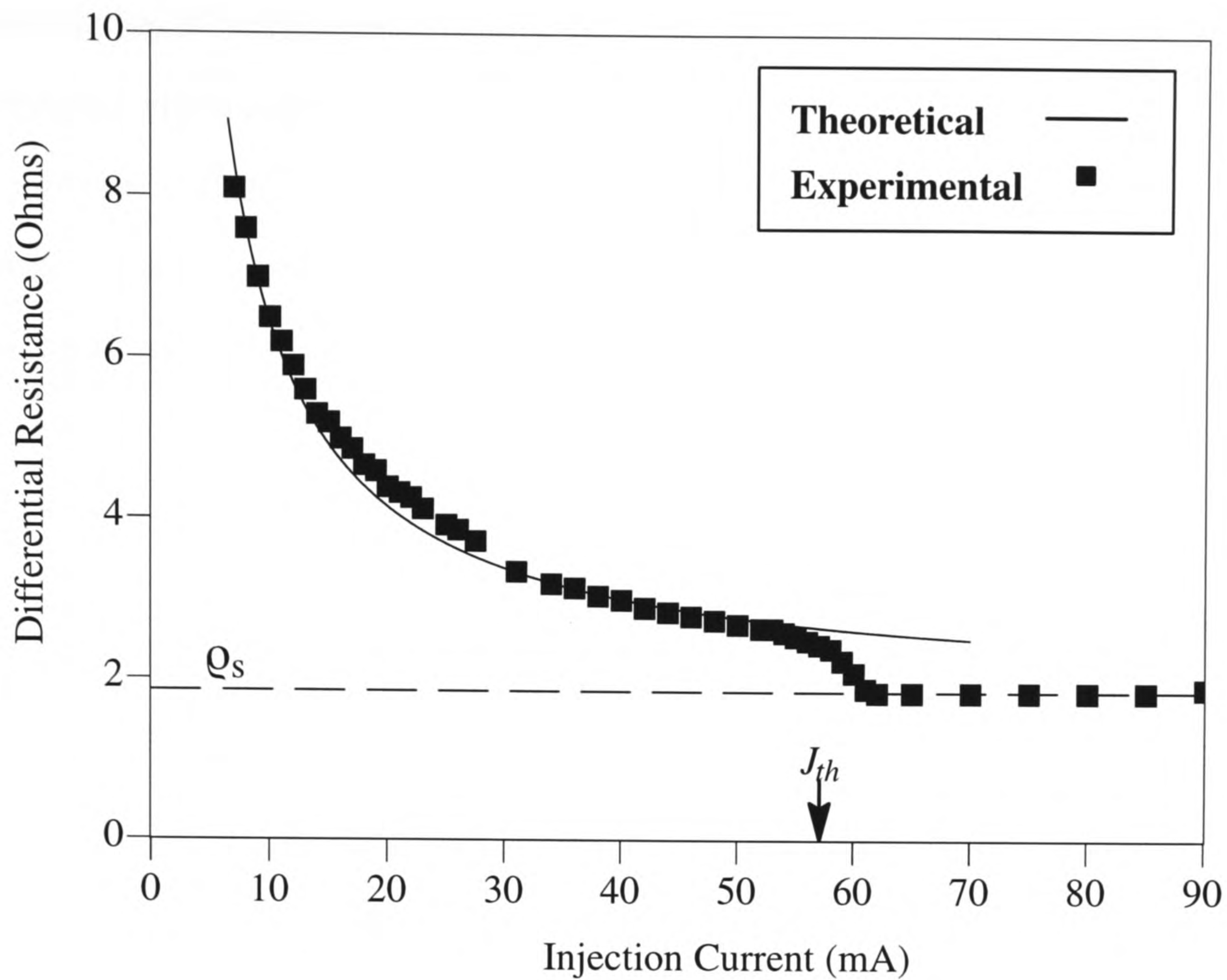

Fig. 30 The differential resistance of the diode laser. The squares represent the experimental measurements whereas the full line is the theoretical prediction from eqn (106).

The fact that the perturbation signal is still proportional to the amplitude of the reflected signal, $|s|$ is illustrated by Fig. 31, where the junction voltage signal is plotted against the feedback intensity. This intensity, which is proportional to $|s|^2$, was measured by an additional photodiode monitoring the signal reflected from a beamsplitter, which was inserted in the path of the feedback signal purely for the purpose of this measurement.

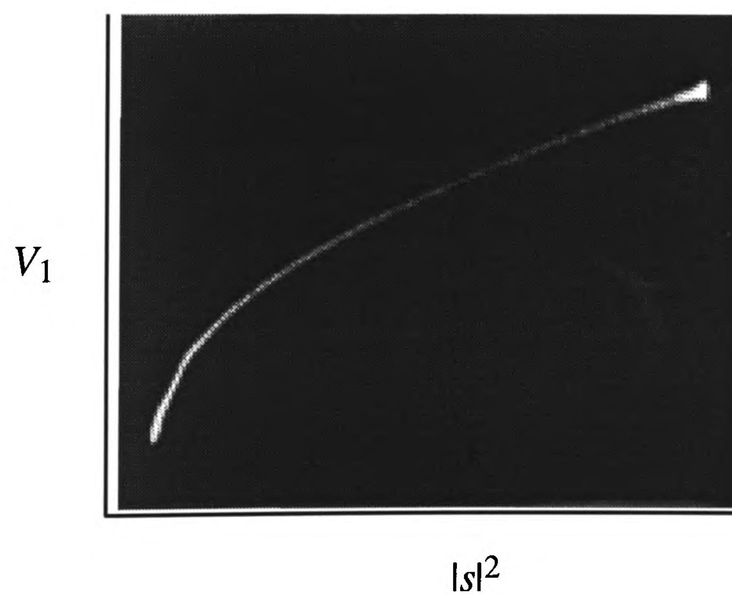

Fig. 31 The dependence of the junction voltage signal on the reflected power. Injection current 64mA.

The variation of both junction voltage and power monitor signals with change of injection current was also measured. According to our theory, if the specimen reflectivity is constant the junction voltage signal should also remain constant while the power monitor signal should increase monotonically with injection current. The measured behaviour was somewhat more complicated as shown in Fig. 32.

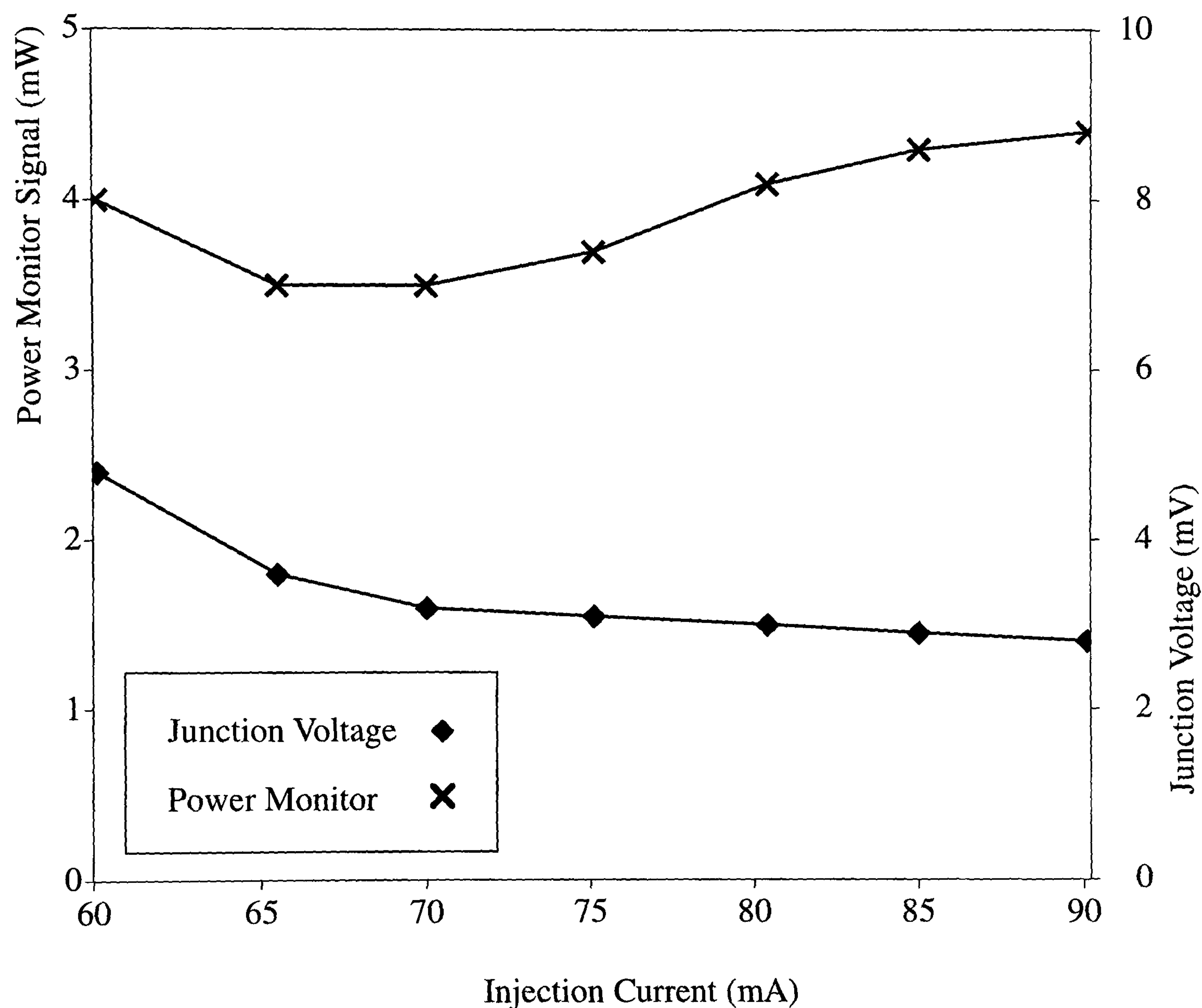

Fig. 32 The variation of the power monitor and junction voltage signals as a function of injection current.

This, we think, again can be attributed to the laser transition from the feedback–locked to the coherence collapse state and accompanying decrease in feedback efficiency. If, however, we take both signals just above threshold, the correspondence between the measured values and those calculated from the eqn (112) is quite reasonable.

5.4.2 Optical Characteristics

To demonstrate the spatial filtering action of the laser detection (which leads to the optical sectioning property of confocal microscopy) we scanned a mirror through the focus of the microscope objective and measured the resulting junction voltage signal. We took the axial responses with different collimating lenses (L_1 in Fig. 28) to simulate different values of parameter a in the eqn (102). The correspondence between the experimental traces shown in Fig. 33 and the calculated ones (Fig. 29) is readily apparent.

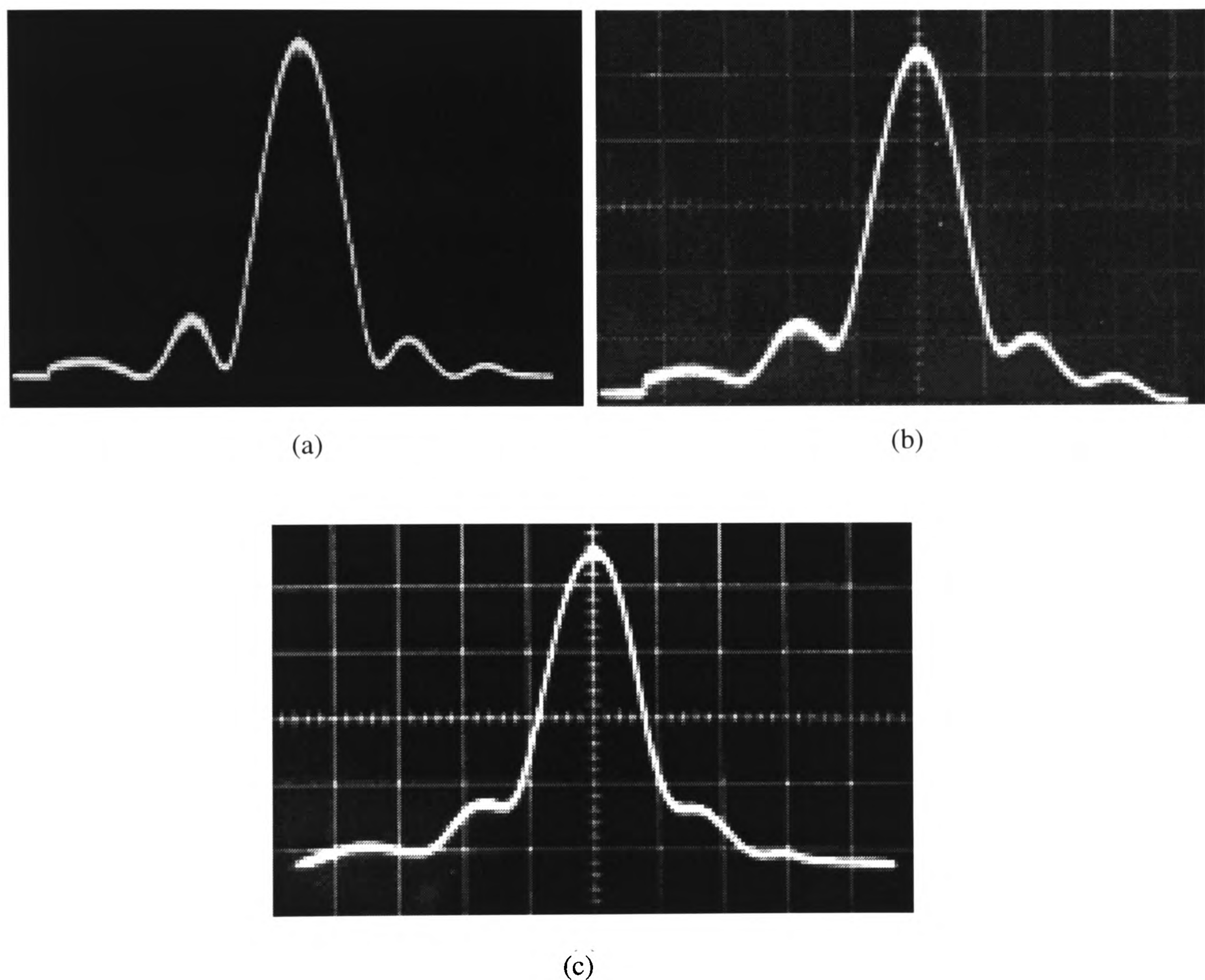

Fig. 33 The axial responses of the diode laser microscope, injection current 64mA. The values of a are (a) 1.0 (b) 1.9 (c) 3.4 . Horizontal scale 2.1μm / division, vertical scale normalised.

Finally, we took a through–focus set of images of a semiconductor chip. Two of these images with an axial separation of about 3μm are shown in Fig. 34. These images do not differ considerably from the images obtained by a scanning microscope using traditional signal detection techniques (see, for instance, [8]).

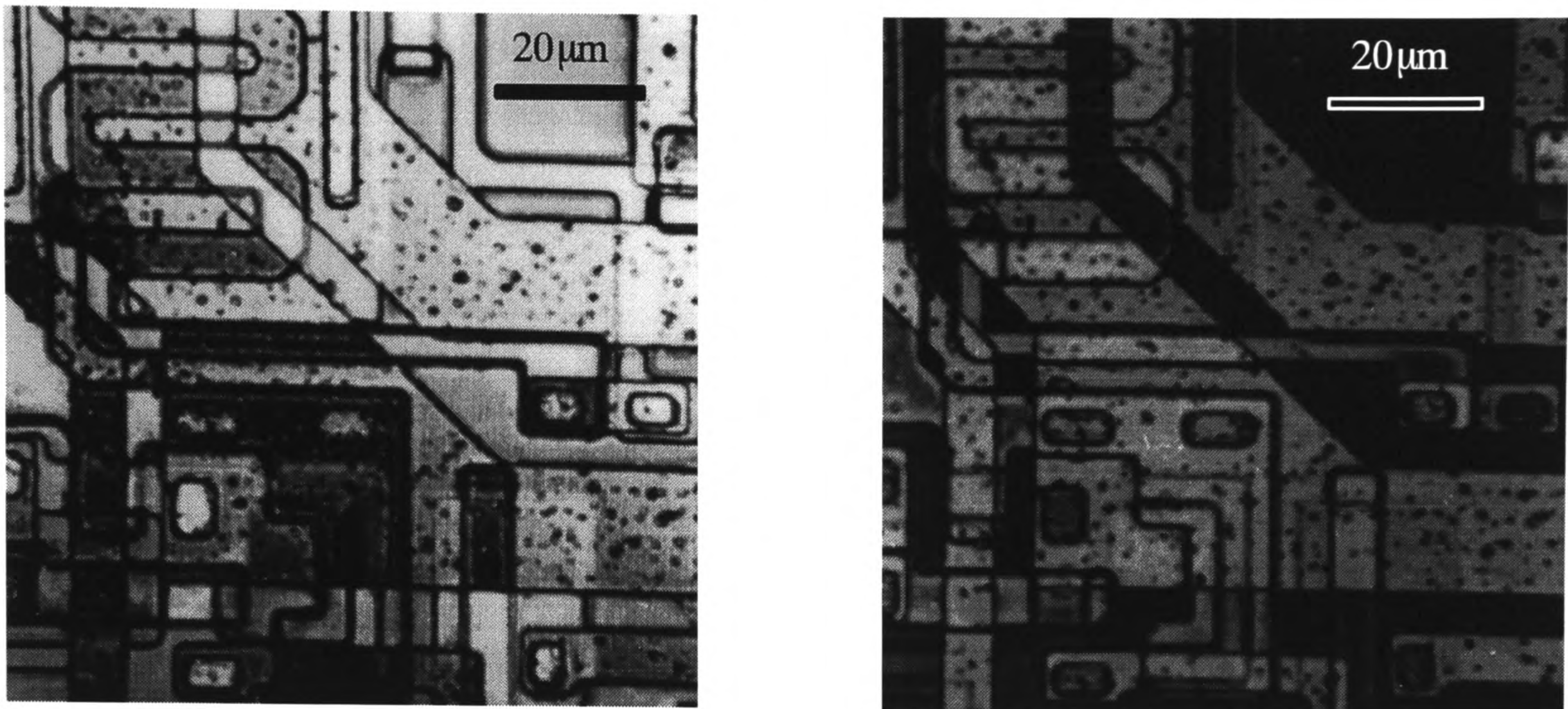

Fig. 34 Two specimen images taken at 3μm axial separation.

From this it can be seen that, despite some of the imaging peculiarities discussed above, this system can perform all the functions of a confocal scanning microscope.

5.5 Conclusions

We have demonstrated a particularly simple and compact form of confocal scanning optical microscope. The optical system consists merely of a semiconductor laser and lens system. No other optical components or photodetectors are required. The laser acts both to launch light into the optical system and also to spatially filter *and* detect the signal reflected back form the specimen. This confocal signal is then measured as a perturbation of the diode junction voltage. The images which result are comparable with those obtained by detecting the signal from a power monitor diode.

Because of the coherent nature of the detection system (whether it be using an optical fibre or the laser itself) the signal detected in these cases is proportional to the modulus of the confocal amplitude signal rather than the modulus squared as in traditional systems. The images which are obtained may therefore be squared if desired although we have found that the raw, unsquared, signal gives acceptable images in most cases.

6. Profilometry using Laser Feedback

6.1 Introduction

The last two chapters have been concerned with the development of a highly compact confocal microscope using a semiconductor laser both as a source of light and also as a confocal detector. The spatial filtering required to give confocal operation is provided by using a single mode semiconductor laser. The fundamental eigenmode serves to detect coherently the on–axis component of the reflected wave. However, as we saw in Chapter 3, a semiconductor laser is significantly affected by optical feedback (as described by a large value for the parameter C), resulting in the generation of a series of closely spaced modes, between which the laser frequency can hop. We saw that this freedom for the laser frequency to vary is automatically used to cancel the variation of the phase of the reflected signal as it enters the cavity. This leaves the image solely dependent on the amplitude of the reflected signal.

We now turn to look at the case of a laser in which the generation frequency is relatively unaffected by optical feedback (as described by the value of C being much less than unity), and for this purpose we use a HeNe laser. In a HeNe laser, the laser frequency remains roughly constant and therefore the phase of the feedback signal varies as the size of the external cavity varies. Hence when this signal is detected simultaneously with the signal from the cavity, an interference pattern occurs. In the past the dependence of the laser power on the feedback condition has been successfully employed as a detection technique in fibre–optic interferometer sensors [33] and Doppler velocimeters [34]. We now describe an extension of these techniques to confocal and interference microscopy.

The optical system we use for the research in this chapter (Fig. 35) is essentially the same as it was for the work with the semiconductor laser. As in Chapter 5, we use the single transverse mode of the laser, rather than a single mode optical fibre, to act as the spatial filter required to achieve confocal imaging. However, in this case, an electro–optic modulator is

included to enable us to control the phase of the signal reflected from the specimen. Also we re–introduce a photodiode to measure the optical intensity emitted from the laser cavity since there is no junction voltage which can be measured in this case.

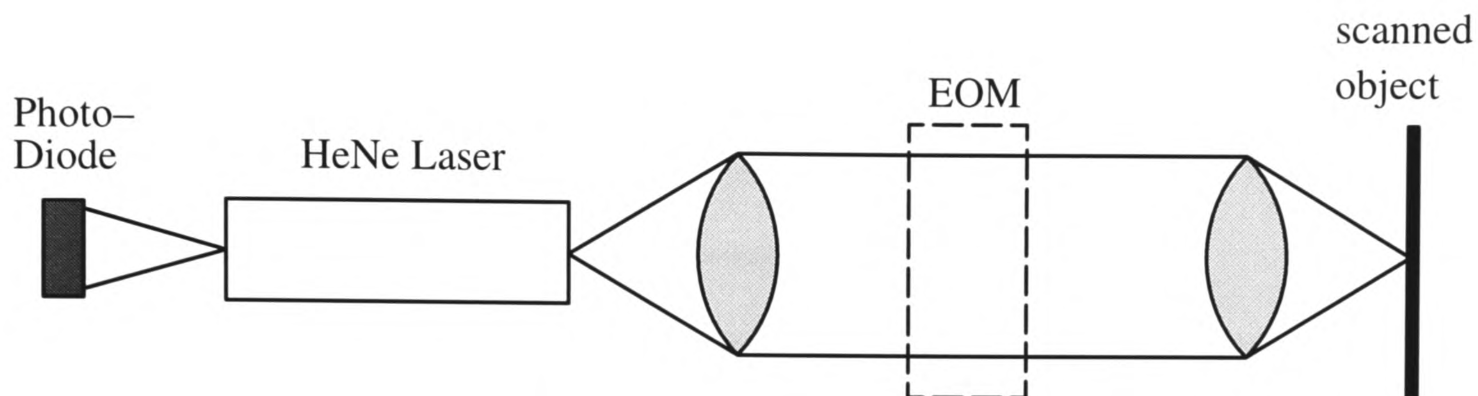

Fig. 35 Schematic diagram of the confocal interference microscope, showing where the electro–optic phase shifter may be introduced for profilometry.

In this chapter we once again present a simpler analysis than that used in Chapter 3 to establish the dependence of the output intensity of a HeNe laser on the reflectivity from an external reflector. We then use the description developed in Chapter 3, of the effect of the phase and amplitude of the signal reflected back into the laser cavity from the object on the behaviour of the laser. With this we show that the predicted axial response is confirmed by the experimental response. Next we describe the profilometry technique we use and establish its theoretical basis. We consider two different types of profilometry, one using a direct feedback control loop and the other a modulation feedback, lock–in system and provide images which show that they can achieve surface profile images of a variety of specimens. We also show that the lock–in system can simultaneously provide pure confocal images of the specimen.

6.2 Simplified HeNe Laser Theory

Once again we wish to express the emitted light intensity I in terms of the unsaturated cavity roundtrip gain $2gL$ and the mirror amplitude reflectivities R_1 and R_2. In the case of a HeNe laser, however, the reflectivities of the cavity mirrors (>99%) are much higher than those

for a semiconductor laser (>30%). As a result the coupling between the internal and external cavity is very weak, so we can use the following, simplified analysis.

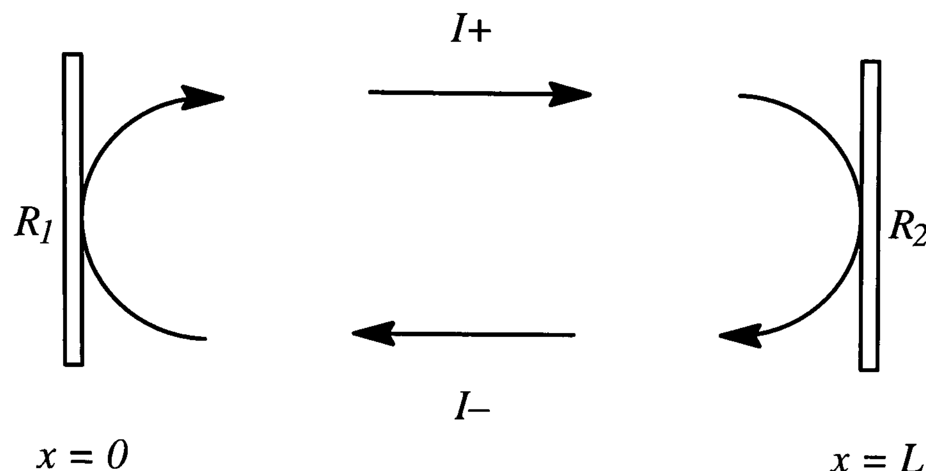

Fig. 36 Schematic diagram of intensity distribution inside a weakly coupled laser cavity.

As in the simplified semiconductor laser model outlined in Chapter 4, we start by making use of the result quoted in eqn (78) to express the intensity gain coefficient of a laser, *g(I)*, in terms of the threshold gain, g_0, and the cavity intensities, I_+ and I_- for any point $0 < x < L$, where I_S is the saturation intensity of the active media.

$$g(I) = \frac{g_0}{1 + \frac{I_+ + I_-}{I_s}} \tag{113}$$

For a HeNe laser we can assume that the end–mirror reflectivities R_1 and R_2 are both close to unity, and hence we can approximate the intensities I_+ and I_- as constants along the length of the cavity as shown below.

$$I_+(x) \approx I_-(x) \approx I_{cav} \tag{114}$$

where I_{cav}, the one–way circulating intensity inside the laser cavity, is, to first order, independent of position inside the cavity. Hence the intensity gain, *g(I)*, where $I = 2\,I_{cav}$, is given by

$$g(I) = \frac{g_0}{1 + \frac{2I_{cav}}{I_s}} \tag{115}$$

which gives

$$I_{cav} = \frac{I_s}{2}\left(\frac{g_0}{g(I)} - 1\right) \tag{116}$$

At threshold the intensity gain and the losses of a round trip in a laser must be equal. Hence, since the Fractional Gain $= e^{2(g(I)-\sigma)L}$ and the Fractional Loss through the mirrors = $(R_1R_2)^2$, we can write

$$R_1R_2e^{(g(I)-\sigma)L} = 1 \quad (117)$$

$$g(I)L = \sigma L - \ln R_1 - \ln R_2 \quad (118)$$

If we now make the simplifying assumptions that $1-R_2 \gg 1-R_1$ (where R_2 is the coupling mirror with the external cavity) and $\ln R_2 \gg g_{th}L$, then we can obtain

$$g(I)L \approx -\ln R_2 \approx 1 - R_2 \quad (119)$$

Hence
$$I_{cav} = \frac{I_S}{2}\left(\frac{g_0L}{1-R_2} - 1\right) \quad (120)$$

The intensity emitted towards the power monitor is $(1-R_1^2)\,I_{cav}$. Hence

$$I = \frac{I_S}{2}\left(1-R_1^2\right)\left(\frac{g_0L}{1-R_2} - 1\right) \quad (121)$$

To achieve eqn (121) we assumed that the laser was strongly asymmetric, $1-R_1 \ll 1-R_2$, as it usually is in HeNe devices.

Now that we have established the intensity dependence on R_2, we need to consider how this will affect the frequency of the emitted light. For this we need to recall the parameter C discussed in Chapter 3 and the fact that for a HeNe laser, with an external cavity of a metre, $C \ll 1$. In this limit the longitudinal laser generation modes are only weakly perturbed by the external reflection and it is appropriate to neglect the effect of the feedback signal on laser generation intensity when calculating the effective reflectivity R. Neither does the lasing frequency shift significantly, nor are other modes generated to which the frequency could easily hop.

We are now in the position to substitute expression (52) to the eqn (121) as follows. Ignoring the initial constants eqn (121) becomes

$$I_{out} \propto \frac{g_0 L}{1-R_2-\left(1-R_2{}^2\right)\,\eta\ \mathrm{Re}\{s\ \mathrm{e}^{-j\omega\tau}\}} - 1 \tag{122}$$

$$= K\left\{1-\left(1\ +\ R_2\right)\,\eta\ \mathrm{Re}\{s\ \mathrm{e}^{-j\omega\tau}\}\right\}^{-1} - 1 \tag{123}$$

where $K = \frac{g_0 L}{1-R_2}$. As discussed before, for our system, $\eta s \ll 1$ so we can use the Binomial expansion to first order which gives

$$I_{out} \approx K\ +\ K\left(1\ +\ R_2\right)\,\eta\ \mathrm{Re}\{s\ \mathrm{e}^{-j\omega\tau}\}\ -\ 1 \tag{124}$$

$$= (K-1)\left(1\ +\ \frac{K}{K-1}\left(1\ +\ R_2\right)\,\eta\ \mathrm{Re}\{s\ \mathrm{e}^{-j\omega\tau}\}\right) \tag{125}$$

Since $R_2 \approx 1$ we can rewrite this as

$$I\ =\ I_0\left[1\ +\ \frac{2\eta K}{K-1}\ \mathrm{Re}\{s\exp(-j\omega\tau)\}\right] \tag{126}$$

s can be expressed as $|U|\exp(\arg(U))$

$$I\ =\ I_0\left[1\ +\ \frac{2\eta K}{K-1}|U|\ \mathrm{Re}\{\exp(\arg(U)-j\omega\tau)\}\right] \tag{127}$$

To obtain an expression for the microscope axial response we need to substitute the expression for the amplitude of the fibre mode excited by the light reflected from the specimen which was derived in Chapter 2, eqn (38). This gives

$$I(u)\ =\ I_0\frac{2\eta K}{K-1}\mathrm{Re}\left\{\mathrm{sinc}\left[\frac{1}{2}\left(u\ +\ \frac{ja}{2}\right)\right]\exp\left(-2jkz\cos^2\frac{\alpha}{2}\right)\right\} \tag{128}$$

Here we omitted the constant laser intensity offset term and set the feedback phase to be zero for the reflector in the focal plane. In the ideal case of the fibre mimicking a pinhole ($a \rightarrow 0$) this expression reduces to

$$I(u)\ \propto\ \mathrm{sinc}(u/2)\cos\left(\frac{4\pi z}{\lambda}\right) \tag{129}$$

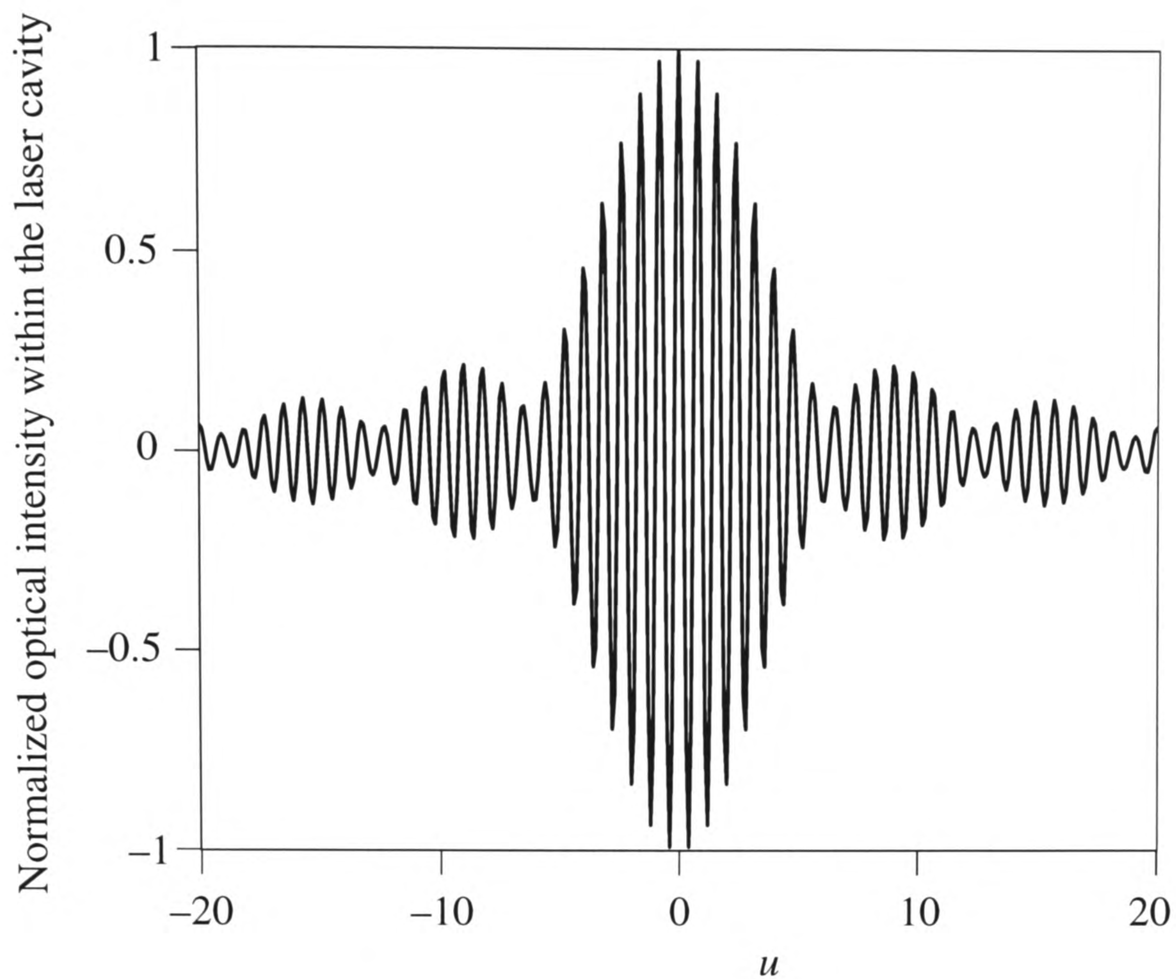

Fig. 37 Normalised axial responses of HeNe laser system
$C \ll 1, a = 1.5$ with $\mathrm{NA} = 0.5$.

However, in practice it is often difficult to choose optical elements to correspond exactly to the idealized $a = 0$ case. We therefore plot in Fig. 37 the effect of a non–zero value of a. The value of a chosen ($a = 1.5$) corresponds to the practical elements used in our experimental set–up which gave the axial response shown in Fig. 38.

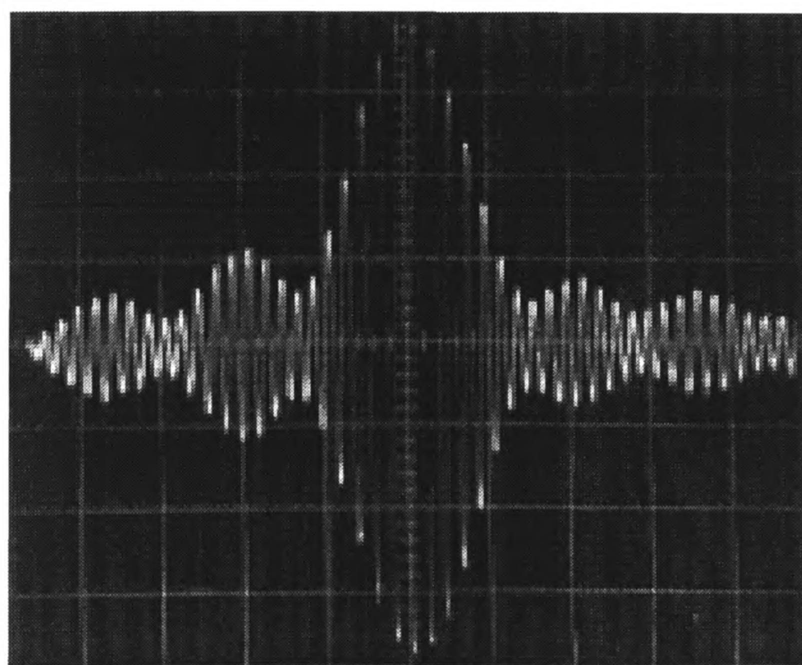

Fig. 38 Axial response of the microscope using HeNe laser. Horizontal scale: 1.5μm / division.

6.3 Introduction to Profilometry

As we have seen, the modulation of the intensity within a HeNe laser, when subject to optical feedback, is proportional to $\mathrm{Re}\{U\}$. Thus the image formation here is similar to that obtained in a confocal interference microscope.

The image contrast in an interference microscope generally consists of a combination of a regular, non–interference image together with an interference image. The latter is particularly sensitive to very small changes in optical path and hence is useful, for example, in surface profilometry[9]. In a conventional interference microscope the non–interference term does not possess an optical sectioning property and hence does not discriminate against detail outside the focal region, although, if the system is properly designed, the interference image does possess an optical sectioning property [35]. However, for the non–interference term to display optical sectioning it is necessary to use a confocal interference microscope. Reflection systems based on a Michelson interferometer [9,36], and transmission systems based on the Mach–Zehnder interferometer[37] have been built. Those systems, although producing images of good quality, suffer from the disadvantages of being non–common path and hence extremely sensitive to spurious air currents. Also they are unable to obtain easily the confocal and interference images simultaneously, and they can be difficult to set up since it is important that the phase fronts of the reference and object beams are made coincident.

We now describe an interference microscope which uses the standing wave within the laser cavity for the reference beam. We will show that the system may be configured to obtain high resolution surface profiles as well as confocal images.

6.4 Profilometry Theory

Based on eqn (127) we can write the interference term of the intensity in the more general form

$$I = |U| \cos[\phi + \arg(U)] \tag{130}$$

where ϕ is an extra phase factor to account for any other phase which might be introduced into the optical path. It is now clear that the image will consist of a confocal modulus image, $|U|$, together with a superimposed fringe pattern. This fringe pattern is particularly sensitive to object height, via $\arg(U)$, and so we will now discuss how this signal may be processed so as to obtain surface profiles.

We begin by considering the image of a planar reflector, for which we can adapt the result for U derived in Chapter 2, eqn (38).

$$U = \mathrm{sinc}\left\{\frac{1}{2}\left(u + \frac{ja}{2}\right)\right\} \cos\left[\phi + 2kz\cos^2\frac{\alpha}{2}\right] \tag{131}$$

From eqn (131) we can see that a surface profilometry system could be built, which set $I = 0$ at each picture point. This could be done by introducing an axial movement of the object designed to ensure that $\phi + 2kz\cos^2\frac{\alpha}{2} = \frac{\pi}{2} + n\pi$, and hence $\cos\left[\phi + 2kz\cos^2\frac{\alpha}{2}\right] = 0$ at each picture point. Monitoring the required axial movement would give the surface profile. This method is necessarily slow and so a preferable alternative is to introduce an electro–optic phase shifter into the optical path which enables us to tune ϕ at each picture point instead of mechanically moving the object. This is illustrated in Fig. 35. This technique has the advantage of speed and permits surface profiles to be obtained in real time.

As an alternative approach to locking onto a fringe to give a zero signal, we may rather use a lock–in amplifier technique which essentially sets $\cos\left[\phi + 2kz\cos^2\frac{\alpha}{2}\right] = 1$. (We will explain later how this is achieved in practice). Surface profilometry is again available either by axially scanning the object or, better, using an electro–optic phase shifter. This approach

has the advantage that by arranging to set the cosine term to unity the image signal is then simply proportional to $|U|$ and hence a confocal modulus image is automatically produced if the phase is varied. If the axial position, z, is varied then a confocal modulus, auto–focus image is produced which, for small values of z, will be very similar to a confocal modulus image. We shall return to discuss the merits of these various approaches later in the next section of this chapter.

6.5 Experimental Technique and Results

6.5.1 Experimental Arrangement

Fig. 39 shows a schematic diagram of our laser detection confocal interference microscope. A Spectra Physics Model 147 HeNe laser was modified to allow access to the output from the rear mirror of the laser cavity. This output was used to measure the modulation on the optical signal caused by the signal which re–enters the laser cavity after being reflected from the specimen. The laser power emitted towards the specimen was measured to be 3.7mW whereas that reaching the photodetector on the back side of the laser did not exceed 40μW. Since the laser generated several longitudinal modes we arranged the length of the optical path of the microscope to be roughly an integer number of laser cavity lengths, so that the reflected signal of all longitudinal modes were roughly in phase when re–entering the cavity. A telescope was used to expand the laser beam before it reached the microscope objective which focussed it onto the surface of the specimen.

A low voltage electro–optic phase modulator, model PC100/2, driven by a VLA30 video amplifier (both from Electro Optic Developments Ltd), was used to control the optical path length between the reference wave (in the laser) and the specimen. The principal axes of the ADP crystal used in the modulator were aligned with the plane of polarisation of the laser, so that pure phase modulation caused by the Pockels effect occurred when the voltage was applied to the modulator. To minimise the noise due to reflections from the crystal surfaces the modulator was slightly inclined to the laser beam. The maximum double–pass phase modulation which could be achieved by this amplifier–modulator setup was about 3.5 radians (peak–to–peak) in 6MHz bandwidth.

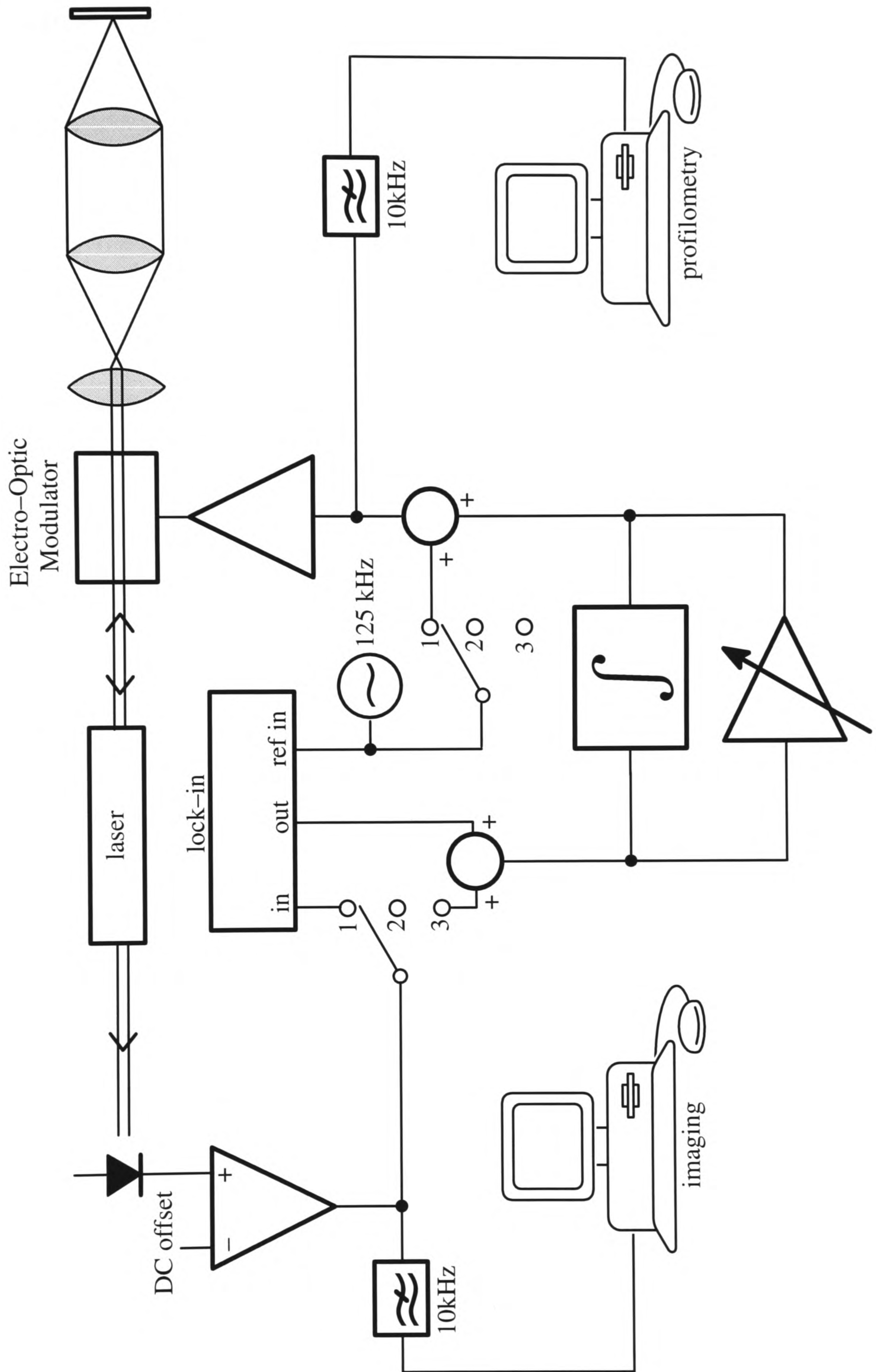

Fig. 39

Schematic diagram of the various interference contrast imaging options.

The switch positions correspond to 1) modulation feedback, 2) open loop, 3) dc feedback.

6.5.2 Experimental Approaches

The control circuitry in Fig. 39 allows us to use the interference microscope in three basic configurations.

6.5.2 .1 *Interferometry*

In the most simple, open loop configuration (switch position 2), no control system was used and the photodiode signal was measured from the back of the laser. The signal consisted of a constant part corresponding to the power of the free–running laser (which we offset) and a small varying part which was the interference signal. This remaining signal was used to provide the interference contrast image of the specimen. In this configuration our microscope can be thought of as similar to a conventional interference scanning microscope, but with confocal operation superimposed as a result of the spatial filtering property of laser detection.

6.5.2 .2 *Direct Feedback Profilometry*

In the closed loop configuration (switch position 3) the offset photodiode signal was used as an error signal for a feedback control loop. The feedback signal was finally applied to the phase modulator, and the overall action of the system resulted in the adjustment of the phase of the optical signal such that the interference term in eqn (131) was zero. In this case the feedback signal represented the height profile of the specimen under investigation and could be used for surface profilometry.

6.5.2 .3 *Lock–In Profilometry*

A more sophisticated version of the closed loop system (switch position 1) used an auxiliary modulation of the optical path at 125kHz and employed a lock–in amplifier (EG&G PARC Model 5210) to produce an error signal. The feedback loop again worked to minimize the error, but this was now achieved when the interference signal was at maximum, rather than zero as in previous case.

In order to understand this we return to eqn (131). Since the phase modulation by the lock–in amplifier was sinusoidal, at a frequency ω, we can express the phase of the signal after it has passed through the Pockels cell once as

$$\phi = \phi_0 + \phi_1 \cos \omega t + \phi_2 \tag{132}$$

where ϕ_1 represents the modulation depth, ϕ_0 is a constant and ϕ_2 is adjustable as a result of the feedback. The input to the lock–in (output from the microscope) is now given by eqns (131) and (132). If we now assume that the lock–in demodulates sinusoidally then the output is given by the time average of, $V(t)$, where

$$V(t) = \operatorname{sinc}\left\{\frac{1}{2}\left(u + \frac{ja}{2}\right)\right\} \cos\left(\phi_0 + \phi_1 \cos \omega t + \phi_2 + 2kz \cos^2 \frac{\alpha}{2}\right) \cos \omega t \tag{133}$$

If we expand the phase term as

$$\cos\left(\phi_0 + \phi_2 + 2kz \cos^2 \frac{\alpha}{2}\right) \cos(\phi_1 \cos \omega t) - \sin\left(\phi_0 + \phi_2 + 2kz \cos^2 \frac{\alpha}{2}\right) \sin(\phi_1 \cos \omega t) \tag{134}$$

then eqn (133) becomes easy to calculate, giving $\overline{V}$, the time average of $V(t)$, as

$$\overline{V} \sim \operatorname{sinc}\left\{\frac{1}{2}\left(u + \frac{ja}{2}\right)\right\} \mathrm{J}_1(\phi_1) \sin\left(\phi_0 + \phi_2 + 2kz \cos^2 \frac{\alpha}{2}\right) \tag{135}$$

where J_1 is a first order Bessel function of the first kind. Since the action of the integral feedback is to set this function equal to zero, it is clear that the variation in ϕ_2 required to achieve this will map the variations in z and hence produce a surface profile. We note that if the phase, ϕ, is modulated with a square wave of frequency, ω, and a similar square wave is used to demodulate the lock–in, then an equation similar to (135) results but with $\mathrm{J}_1(\phi)$ replaced by a more complicated function of ϕ_1. As has been mentioned, an additional advantage of this modulation–locked feedback system is that a confocal modulus image (photodetector signal) could be obtained simultaneously with the height image (modulator voltage) since the cosine terms of eqns (130) and (131) are set to be constant. A further experimental bonus was that since the feedback loop operated at the modulation frequency (125kHz) the effect of any low frequency laser noise and interference noise from spurious reflections was considerably reduced.

Our feedback system also offers some flexibility in tuning the image quality in the surface profiling mode. The purely integrating feedback does, of course, provide zero error operation but we found that it wasn't fast enough in some circumstances. This was particularly true when used in conjunction with the lock–in amplifier with an integration time constant of around 100μs. In the modulation feedback regime we therefore decided to introduce a parallel proportional feedback channel. This reduced the overall system response time but at the price of introducing some dynamic error which could be reduced by increasing the overall loop gain as long, of course, as the system remained stable.

6.5.3 Preliminary Results

When the modulation feedback system is used the "cosine term" in eqn (131) is set equal to unity and the image is given by $|U|$. In the case of the axial response of a plane this reduces to $\left|\text{sinc}\frac{1}{2}\left(u + \frac{ja}{2}\right)\right|$. Fig. 40 shows the response for the 0.5NA objective. We note, again, that the usual confocal response is simply the square of this response [9,10].

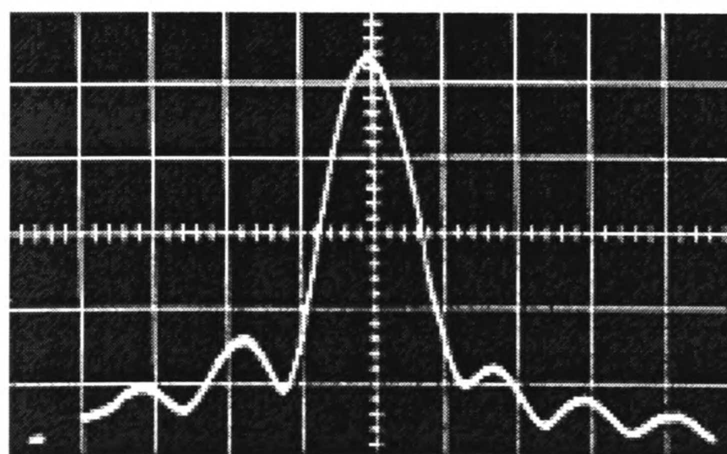

Fig. 40 Axial response with closed loop operation, NA=0.5.
One division represents an axial scan of 1.0μm.

In order to demonstrate the wide range of imaging capabilities of our system, we used a selection of specimens containing features with a variety of lateral and axial dimensions. The first was a waveguide structure manufactured by depositing a photoresist pattern on a glass substrate. The height of the photoresist stripes was about 0.14μm, and this meant that it lay outside the linear range of our interference microscope in the open–loop configuration. This can be seen in the linescan of Fig. 41(a) where the foldover effect of the fringes

results in a considerably distorted profile of the specimen, even when the phase offset is adjusted to its optimal value. It should be noted that the specimen was almost perfectly perpendicular to the optical axis, and hence there are no fringes across the surface. For comparison the linescan obtained in the closed–loop configuration is presented in Fig. 41(b).

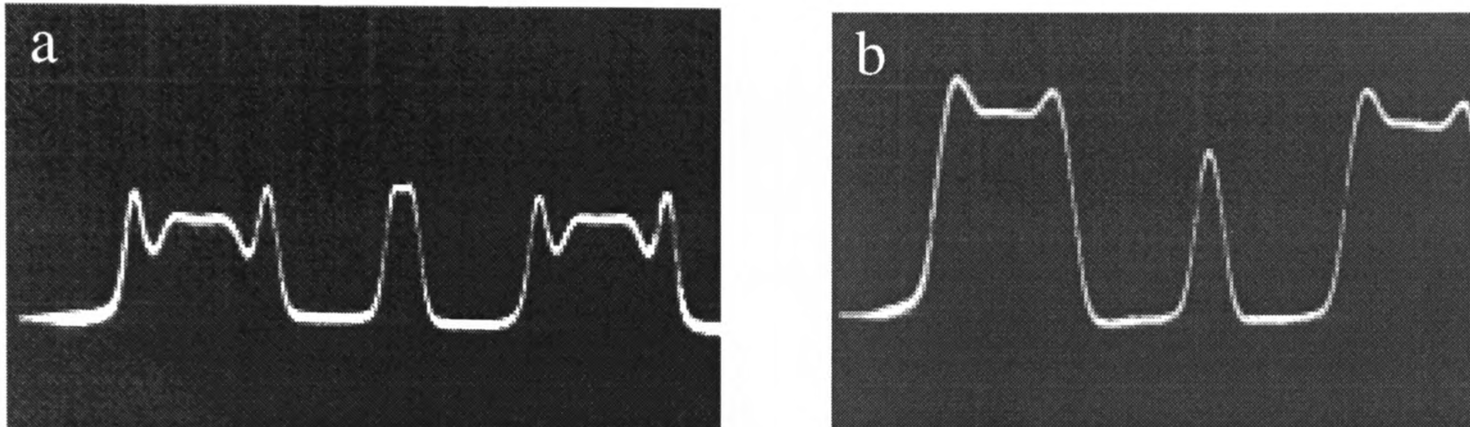

Fig. 41 Photoresist waveguides on glass.
Linescans with a) open loop and b) closed loop operation.
One division represents 4μm.

6.5.4 Images

In figures 42 to 46 we present a series of images of the stripe waveguide specimen.

Fig. 42 is a confocal interference image consisting of a confocal image with a fringe pattern superimposed. This fringe pattern is a result of the slight tilt of the specimen relative to the plane along which it was scanned.

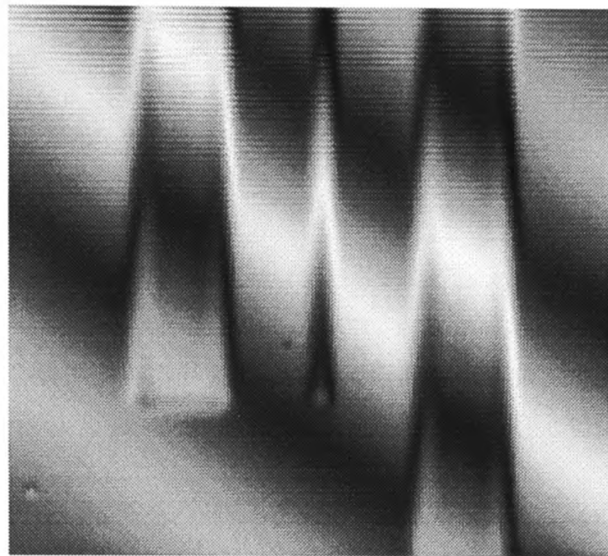

Fig. 42 Ordinary interference pattern of the stripe waveguide.

Fig. 43 shows a surface profile of the structure obtained using the dc feedback technique. The raw height data from the microscope has been subjected to differential filtering and volume rendering algorithms to produce the representation shown.

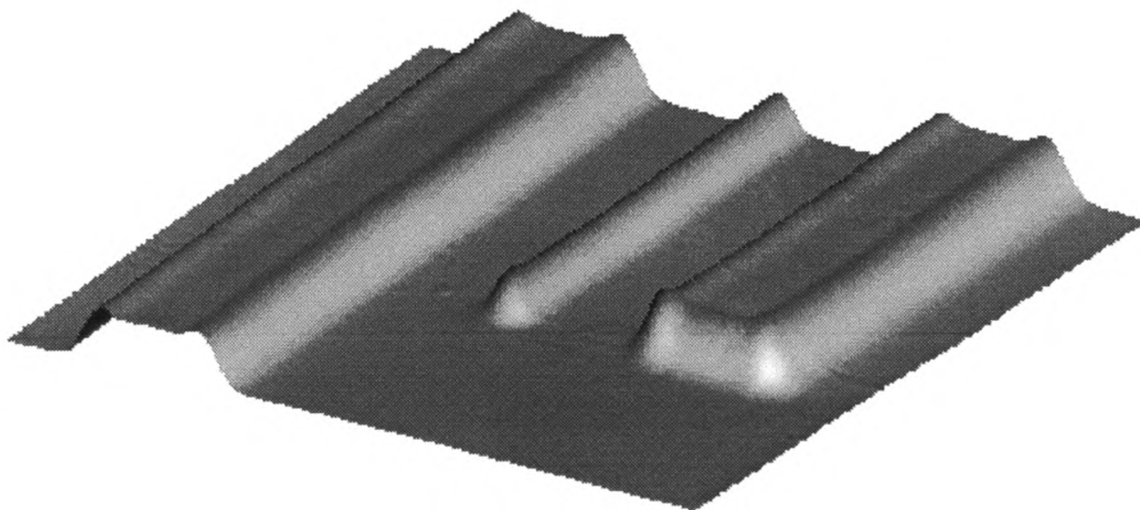

Fig. 43 Surface profile of the stripe waveguide using the dc feedback technique.

Fig. 44 shows the surface profile of the same region of the specimen when the raw data was obtained by the modulation feedback technique.

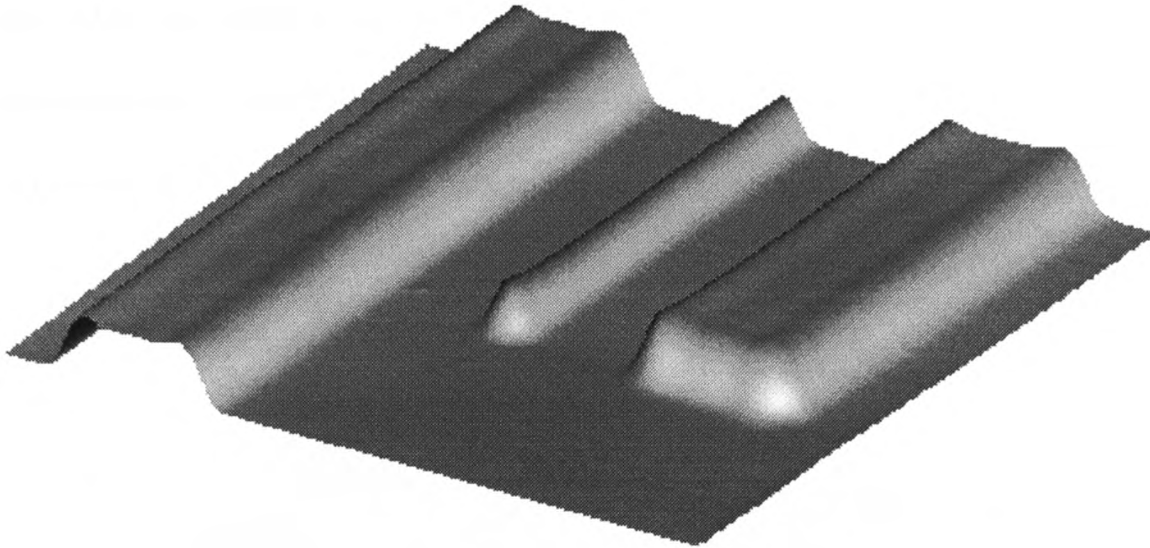

Fig. 44 Surface profile of the stripe waveguide using the modulation feedback technique.

An advantage of this technique, as we have said, is that it automatically generates a confocal modulus image. This is presented in Fig. 45.

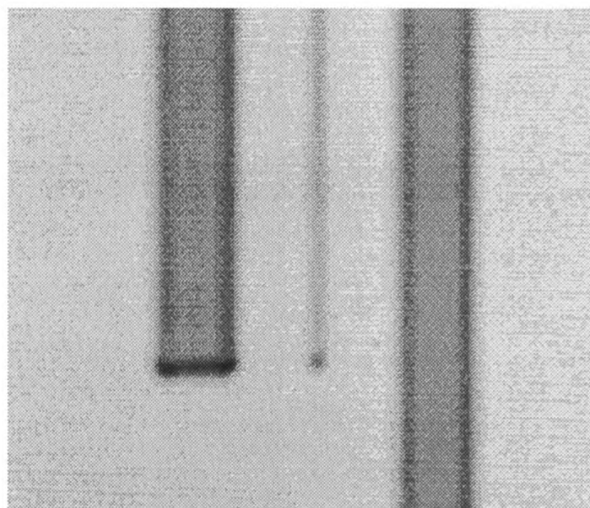

Fig. 45 Confocal image of the stripe waveguide, obtained simultaneously with Fig. 44.

The surface profiles of Fig. 43 and Fig. 44 together with the linescan of Fig. 41(b) suggest that the waveguide structure possesses a pronounced ridge around the upper edge. It is thought that this is due to a diffraction effect when the negative photoresist is exposed to the light diffracted by the photomask. In order both to confirm that this ridge is not an artifact and to demonstrate the sensitivity and resolution of our system Fig. 46 shows the surface profile obtained using data from an atomic force microscope (Park Instruments).

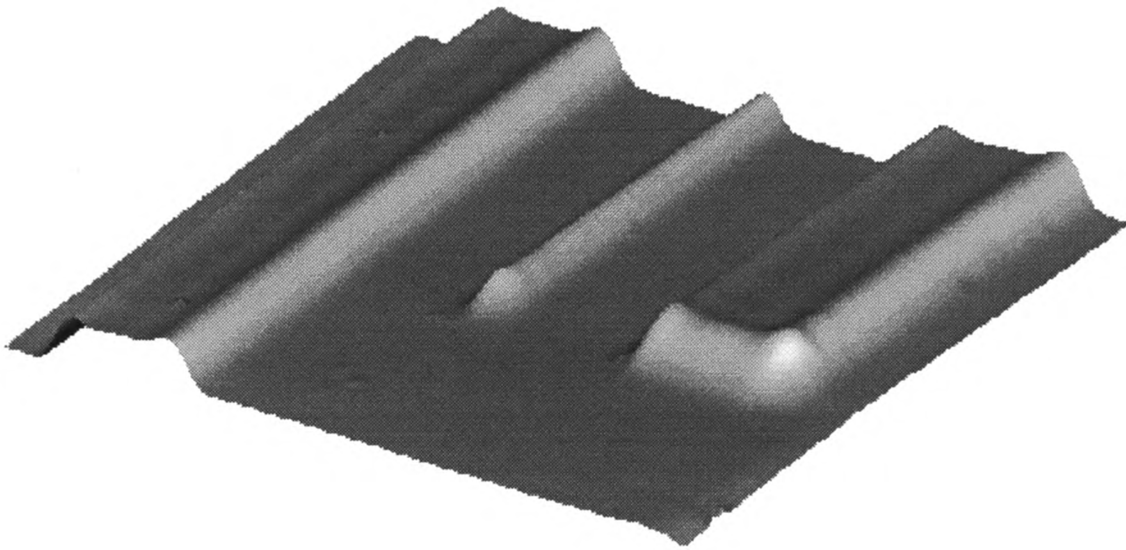

Fig. 46 Atomic Force Microscope image of the stripe waveguide.

As a further specimen we imaged a 13nm high, 8μm wide, stripe produced on the surface of a piece of lithium niobate by dry plasma etching away the surrounding area. The difference between the smooth, unetched, top surface and the rough, etched, bottom surface is clear, Fig. 47.

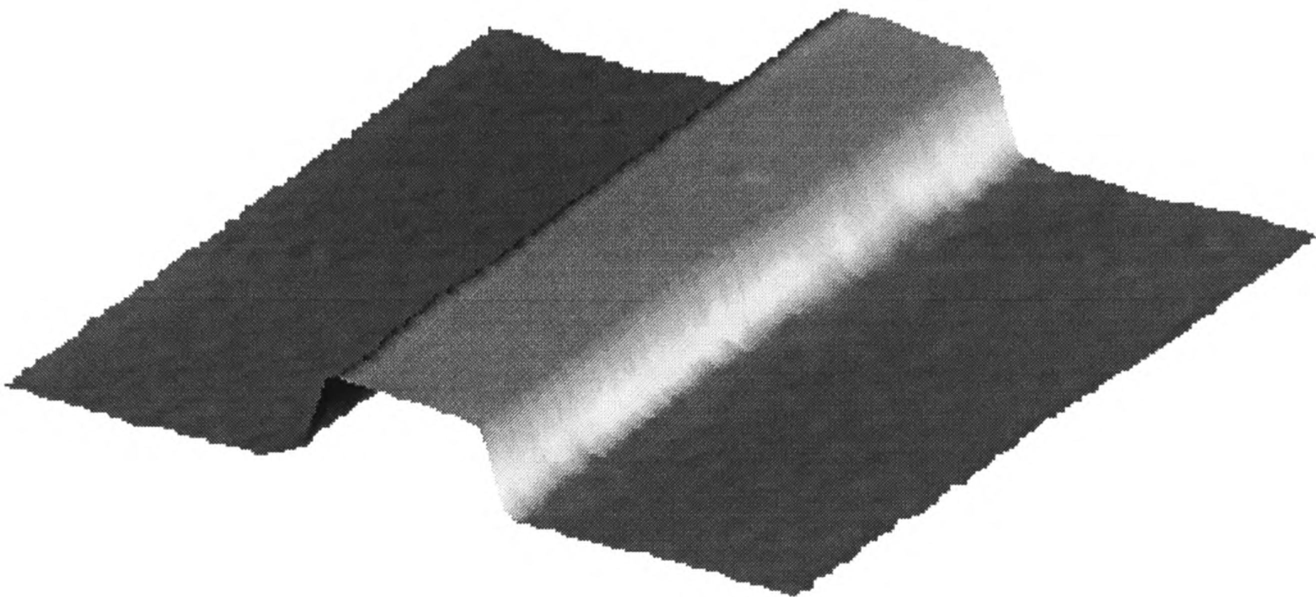

Fig. 47 The surface profile of an etched strip in Lithium Niobate. The strip is 8μm wide and 13nm high.

Our final specimen consists of the (001) surface of silicon which had been annealed in 1 mbar of H_2 for 30 minutes at 900°C [38,39]. This process results in "thermal roughening" of the surface [38]. Fig. 48 shows the surface profile. The image region is 5μm square. The height of the 'bumps' range from 5 to 7nm and their diameter is about 500nm.

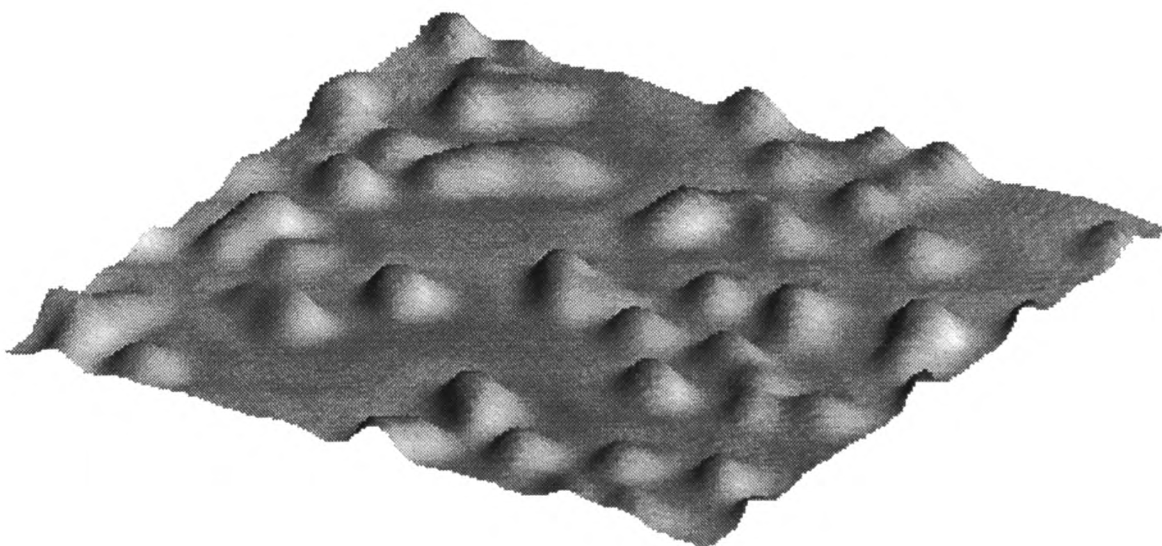

Fig. 48 The surface profile of the annealed silicon wafer. The image region is 5μm square.

A comparison Atomic Force Microscope investigation produced a similar image, shown in Fig. 49. It should be noted that this is a comparable area of the same specimen, but not exactly the same area.

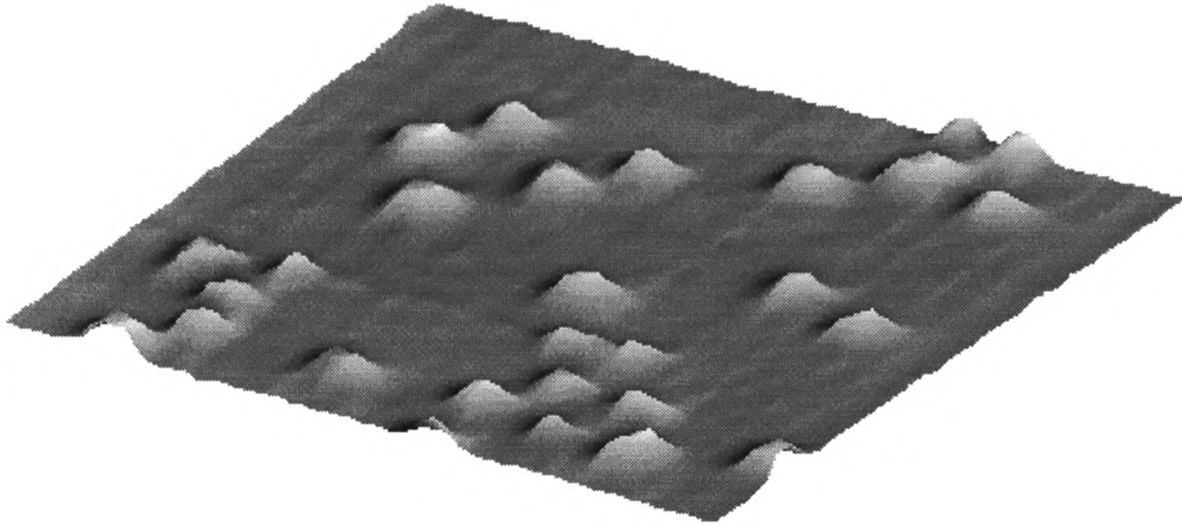

Fig. 49 AFM surface profile of a different area of the annealed silicon wafer.

6.5.5 Noise Considerations

The modulation feedback and dc feedback techniques produce similar surface profiles but do differ in their susceptibility to noise. The strongest source of noise we had to deal with was due to mechanical vibrations which are difficult to eliminate completely since our system is not a common path interferometer. Under our best daytime experimental conditions the vibration amplitude was of the order 1nm. In order to produce images of small height variation such as Fig. 47 and Fig. 48 we averaged over several images.

The next source of noise to consider is that caused by the plasma discharge in the laser tube. We measured this noise and found that the spectrum was flat around 125kHz, but that the noise increased rapidly at frequencies below 1kHz. We were therefore able to achieve higher sensitivity when the microscope was operated in the modulation feedback mode. We estimated the noise to be equivalent to 0.1nm height resolution. The ultimate sensitivity of our system is thus estimated to be $10^{-3}\,\mathrm{nm}/\sqrt{\mathrm{Hz}}$.

6.6 Conclusions

We have described a compact confocal interference microscope using feedback into a Helium–Neon laser. We established theoretically the relationship between the signal reflected from the specimen and the resulting signal within the laser cavity and showed that this is a superposition of an interference pattern on a confocal envelope caused by the spatial filtering of the laser mode. This was demonstrated experimentally. The fringe pattern of the interference term was then used in a variety of ways. In the simplest approach it was demonstrated that a confocal interference image may be obtained. However if feedback control is introduced the system becomes significantly more versatile. In the simplest, dc feedback case high resolution surface profilometry is possible. However when a lock–in technique (using modulation feedback) is used, confocal imaging is also available simultaneously. This has been demonstrated experimentally with a variety of images of different objects.

7. Profilometry by Calculation

7.1 Introduction

In the last chapter we considered a confocal interference microscope which, using a modulation feedback control technique, could simultaneously produce confocal images and surface profiles in real time. However it suffered from a number of drawbacks which mostly stem from its need for a feedback control system. The limited response speed of the system limits the sharpness and size of the edges of an object which can be adequately imaged.

We will now describe a microscope which can achieve similar results but without the need for a feedback system. Instead, the image will be calculated electronically from the raw amplitude and phase signal.

First we consider the theory behind this system and model its imaging capability. We then provide experimental confirmation of these predictions and finish by presenting interference, confocal and surface profile images of a test specimen obtained using this microscope scheme.

7.2 Theory

7.2.1 Theoretical Basis

A schematic interferometer is illustrated in Fig. 50. There a beam splitter transmits part of the beam into one arm of the interferometer and reflects the rest into the other arm, before both meet again at the detector. In this case the transmitted part is the constant reference beam and the reflected part (the object beam) is subject to variations of its optical path. These variations result in a change in the phase of the object beam, which when it interferes with the reference beam, results in a variation of the detected intensity.

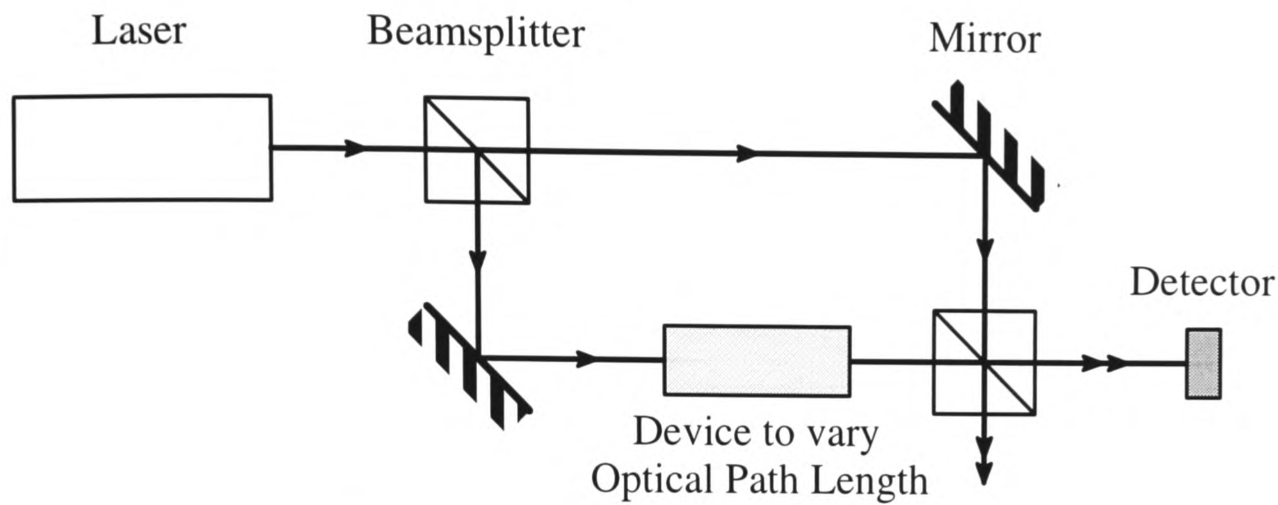

Fig. 50 Schematic diagram to illustrate the principles of interferometry.

This can be considered mathematically as follows. Let the complex amplitudes of the reference beam and the object beam be E_r and E_o respectively and the phase introduced by the device be ϕ. The resulting amplitude of the signal incident on the detector is then given by

$$E = E_r + E_o \; e^{j\phi} \tag{136}$$

The detected intensity is then given by the square of this, ie

$$I = \left| E_r + E_o \; e^{j\phi} \right|^2 \tag{137}$$

The interferometer described above is clearly very non–common path and makes the detected interference signal very vulnerable to perturbations such as mechanical vibrations or air currents which affect the two optical paths separately. Since the interferometer is intended to detect the variations in optical path length solely caused by the device in the object path it is advantageous to make the optical paths common for as much of the system as possible.

In the microscope design which we now describe (Fig. 51), the interferometer is made much more common path by using a single mode optical fibre to produce the reference beam for the interferometry. The laser beam is coupled into the fibre and index matching is used to reduce reflection. The other end of the fibre is not index matched to the microscope optics and hence part of the beam carried by the fibre is reflected back along the fibre from that end. This forms the reference beam. The object beam is reflected back from the object and is coupled back into the same fibre. Hence the wavefronts of both the object and refer-

ence beams propagate back along the fibre in the same mode and are perfectly matched when they are permitted to interfere on the photodiode detector. The detected signal is now given by

$$I = |r + U|^2, \tag{138}$$

where r denotes the amplitude of the reference beam and U is the confocal amplitude image.

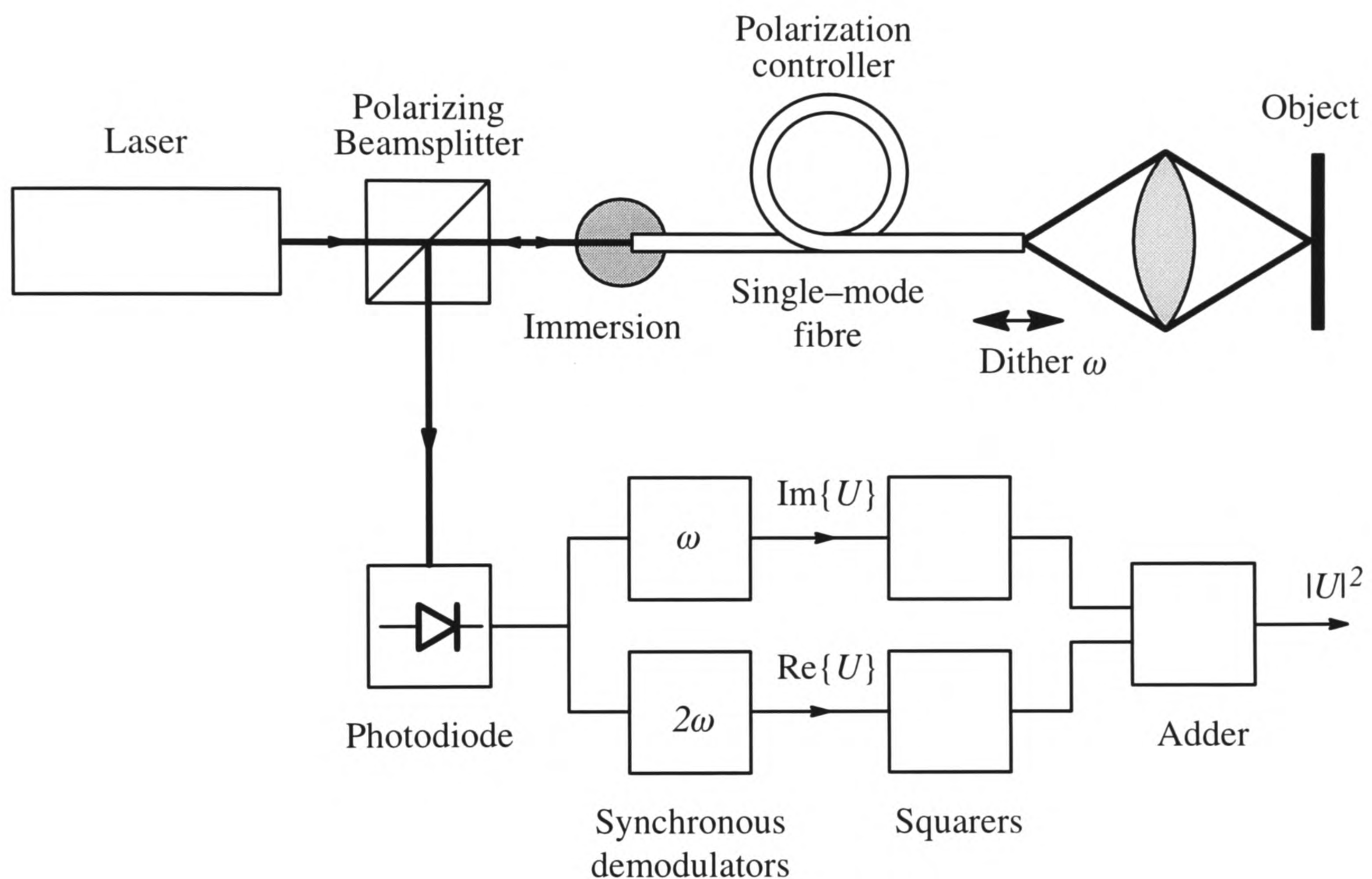

Fig. 51 Schematic diagram of the microscope and signal processing stages.

From Fig. 51 it is clear that the only non–common path part of the system is that between the fibre tip and the object, and this can be made very short. Although this system is easy to align and produces interference images of good quality it is still not possible to separate out the interference term, $2\mathrm{Re}\{Ur^*\}$. from the confocal term $|U|^2$. In order to do this we elect to dither the fibre tip by a small distance so as to introduce a time varying phase shift $\phi(t) = \phi_0 \cos\omega t$ into the object beam. Eqn (138) now takes the form

$$I = |r + U\exp j\phi(t)|^2 = r^2 + |U|^2 + 2r\left[\mathrm{Re}\{U\}\cos(\phi_0\cos\omega t) - \mathrm{Im}\{U\}\sin(\phi_0\cos\omega t)\right] \tag{139}$$

where $\mathrm{Re}\{U\}$ and $\mathrm{Im}\{U\}$ denote the real and imaginary parts of U respectively. We have also assumed, for simplicity, that r is real.

We now recall that we may expand the sine and cosine terms as [40]

$$\begin{aligned} \cos(\phi_0 \cos\omega t) &= \mathrm{J}_0(\phi_0) - 2\mathrm{J}_2(\phi_0)\cos 2\omega t + 2\mathrm{J}_4(\phi_0)\cos 4\omega t + \ldots \\ \sin(\phi_0 \cos\omega t) &= 2\mathrm{J}_1(\phi_0)\cos\omega t - 2\mathrm{J}_3(\phi_0)\cos 3\omega t + \ldots \end{aligned} \tag{140}$$

It is therefore clear that if we multiply the signal of eqn (139) by cos ωt and average the result with respect to time (in other words carry out synchronous demodulation) we obtain

$$I_1 \sim \mathrm{Im}\{U\}\ \mathrm{J}_1(\phi_0), \tag{141}$$

whereas synchronously demodulating with cos $2\omega t$ yields

$$I_2 \sim \mathrm{Re}\{U\}\ \mathrm{J}_2(\phi_0). \tag{142}$$

I_1 and I_2 are quadrature interference term images which contain all the information about the amplitude and phase of the object beam. These images may now be used in a variety of ways to produce information about, for example, the specimen surface height and roughness. Alternatively if we square and add suitably scaled versions of I_1 and I_2 we should obtain $|U|^2$, the confocal image.

We should also mention that if, instead of using a synchronous demodulation scheme on the signal of eqn (139), we were simply to employ a low pass filter such that only the dc component is passed, our image would take the form

$$I_3 = r^2 + |U|^2 + 2rU_i\ \mathrm{J}_0(\phi_0), \tag{143}$$

which, if we arrange to choose $\phi_0 \approx 2.4$ such that $\mathrm{J}_0(\phi_0) = 0$, reduces to the confocal image together with a constant offset signal which can easily be subtracted.

In order to demonstrate the effectiveness of our scheme we consider the signal which is detected as a perfect reflector is scanned through focus. Using the result derived in Chapter

2 for the normalised confocal amplitude image, U, (eqn (38)), we can calculate the full expression for eqn (138) as [41]

$$I = r^2 + \frac{1}{N^2}\left|\mathrm{sinc}\frac{1}{2}\left(u + j\frac{a}{2}\right)\right|^2 + \frac{2r}{N}\mathrm{Re}\left\{\exp\left(-2jkz\cos^2\frac{\alpha}{2}\right)\mathrm{sinc}\frac{1}{2}\left(u + j\frac{a}{2}\right)\right\} \quad (144)$$

Here, as before, z is the distance of the object from the focal plane and $u = \frac{8\pi z}{\lambda}\sin^2\frac{\alpha}{2}$. The normalisation constant is $N = \mathrm{sinch}(a/4)$, where $\mathrm{sinch}(x) = \sinh(x)/x$. r is now the relative amplitude of the reference beam compared to the confocal amplitude image.

7.2.2 Theoretical Results

If the reference beam were considerably stronger than the object beam then the second term in eqn (144) (which contains the pure confocal image of the specimen) would become insignificant. We would then be able to obtain the interference term response by simply subtracting the first term which describes constant signal due to the reference beam.

Fig. 52 shows the symmetrical form of the signal which would be measured by an ideal pinhole ($a = 0$) for the case of the reference signal being much stronger than the signal reflected from the specimen ($r \gg 1$).

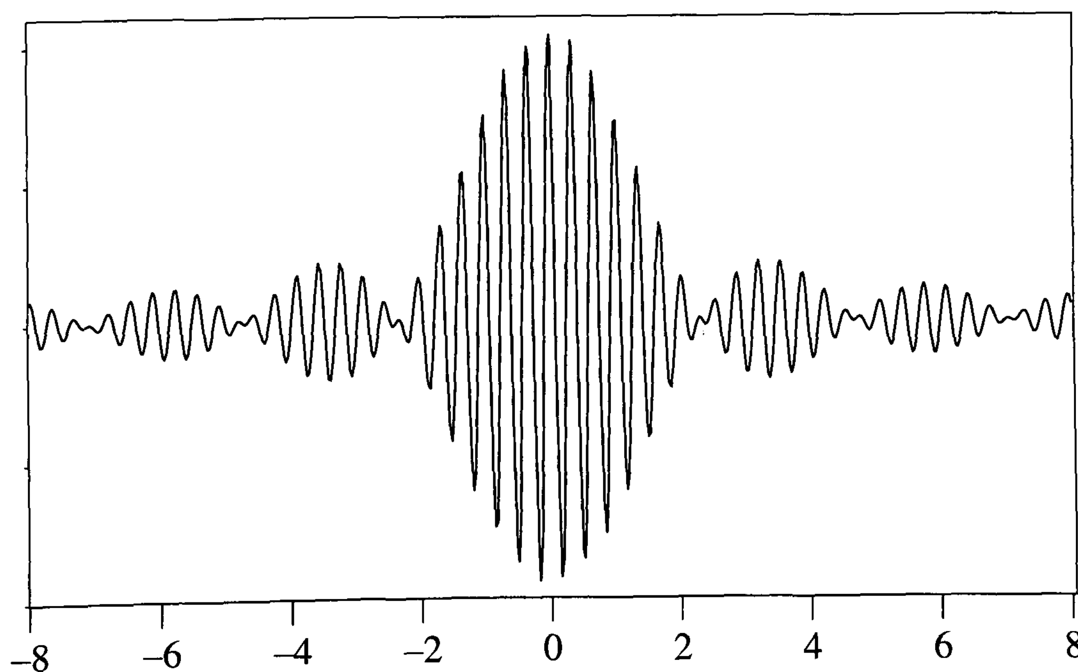

Fig. 52 Theoretical axial response for $r \gg 1$ $a = 0$ (horizontal scale is in microns).

However, this approach is undesirable since, in practice, the reference beam can be strengthened only at the expense of the object beam, thus leading to in a weak interference term. In our system the reference beam is comparable to the object beam in intensity and the measured signal takes the form of Fig. 53, which is calculated for the case of $r = 0.7$, $a = 0$.

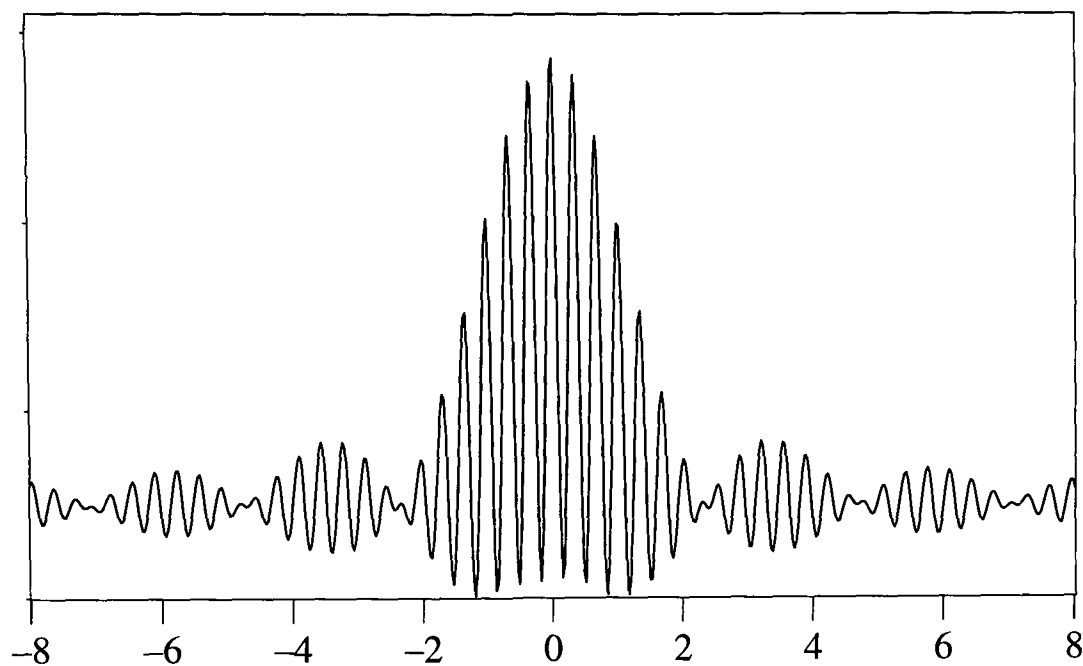

Fig. 53 Theoretical axial response for $r = 0.7$ $a = 0$ (horizontal scale is in microns).

However, for the optical system we used, the finite size of the optical fibre mode had a noticeable effect on the signal and the appropriate value for the fill factor, a, was found to be 4. When this is taken into account the predicted signal is as shown in Fig. 54.

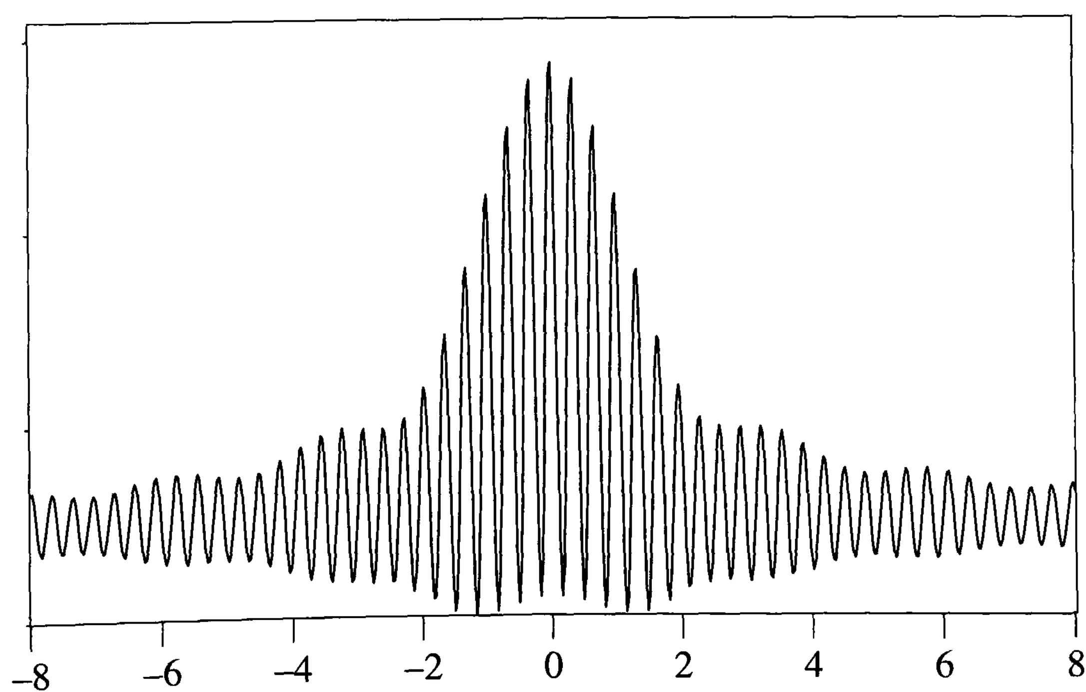

Fig. 54 Theoretical axial responses for $r = 0.7$ $a = 4$ (horizontal scale is in microns).

The synchronous demodulation scheme is able to extract the symmetrical interference term, described by the third term in eqn (144), from this response. This is shown in Fig. 55 for the values of r and a which described the actual system we used.

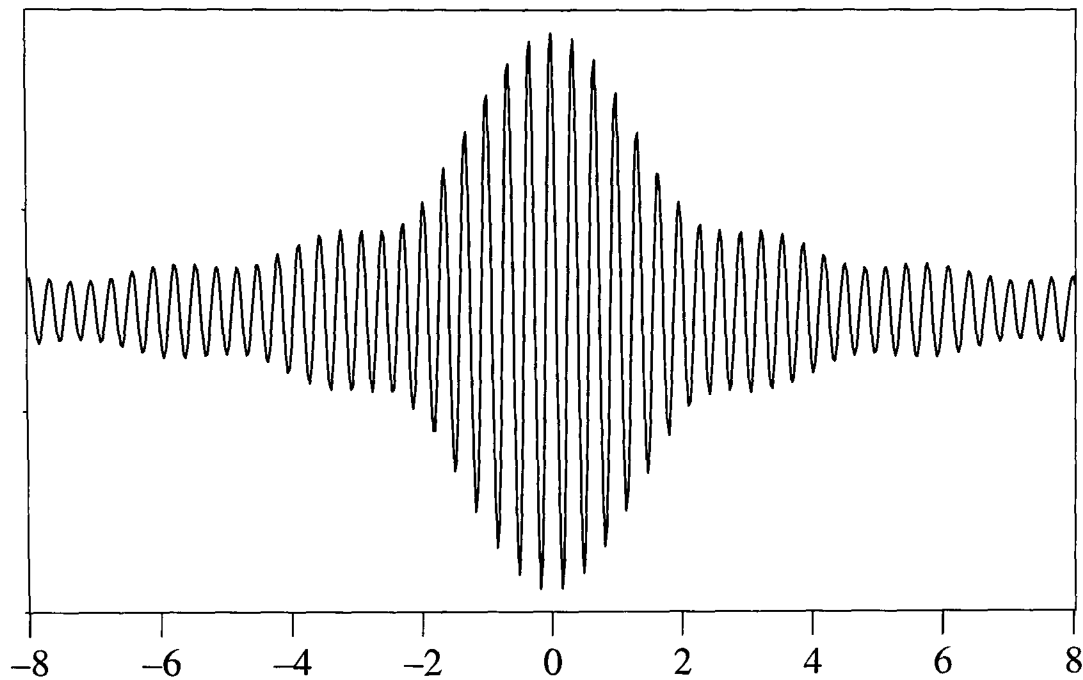

Fig. 55 Theoretical axial responses for $r = 0.7$ $a = 4$
(horizontal scale is in microns)

The axial response signals obtained by demodulating at ω and 2ω have the same form as Fig. 55 but with a $\pi/2$ phase shift between their respective interference fringes.

To obtain a confocal image, it is then a simple matter to square and add these two signals which, in the case of the axial scans shown, gives the usual $\left|\text{sinc}\frac{1}{2}\left(u + j\frac{a}{2}\right)\right|^2$ axial response of the confocal microscope.

A significant limitation of this approach is the fact that it can only image directly features which are less than $\lambda/2$ in height. Any higher and the interference pattern ceases to give a linear response by folding over to the next fringe. To overcome this 2π phase ambiguity requires the combination of the phase information from the interference term image with the optical sectioning information of the confocal image as demonstrated by Juškaitis & Wilson [42], or two–wavelength and white–light interferometry developed by Chim & Kino [43].

7.3 Experimental Technique and Results

7.3.1 Arrangement

Initially, we attempted to demonstrate our approach by using a reciprocal arrangement of the optics, such as that used in the last chapter. In that case the signal reflected from the specimen was permitted to re–enter the laser cavity and interfere with the light reflected from the cavity coupling mirror. However we found that the small feedback perturbation in the laser cavity which resulted was too great to be acceptable: it had the effect of disturbing the quadrature relationship of the demodulated signals.

The experimental arrangement we eventually elected to use is depicted in Fig. 51. In this arrangement we introduced a single mode optical fibre to provide the reference beam. The output end of the fibre was not index–matched, resulting in some internal reflection, and this acted as the reference beam. Light from a HeNe laser operating at 633 nm passed through a polarizing beam splitter and was launched into a single mode optical fibre (York SM600). An index matching solution of glycerol and water was used to prevent any back reflections from the input end of the fibre. Light was then coupled into the confocal microscope from the output end of the fibre whose tip was mounted on a piezo–electric cylinder in order to allow us to introduce a high frequency dither mechanically. A 0.5 numerical aperture objective lens was used. The confocal amplitude signal travelled back along the fibre together with the reference beam and these were finally allowed to interfere on the photodetector.

Because of the sensitivity of the laser to optical feedback in this system, it was important to minimize the reflected signal which could re–enter the laser cavity. To achieve this we used a polarization controller which consisted of a loop in the optical fibre, with adjustable radius. The loop was a means of introducing birefringence into the fibre and thus making it work as a variable phase retarder. By carefully adjusting the radius of the loop we made it act as a quarter–wave plate. We adjusted the axis of birefringence by rotating the loop until

it was at 45° to the linear polarization of the signal from the laser. Thus the signal incident on the specimen became circularly polarized. The signal which reflected from the specimen and passed back through the polarization controller in the same fibre therefore became linearly polarized orthogonally to the signal entering the controller from the laser. When a polarizing beamsplitter was used with this polarization controller, it was possible to ensure that the signal reflected from the object was reflected by the beamsplitter towards a detector, rather than transmitted back into the laser. Hence the whole arrangement (the beamsplitter and the fibre) acted as an optical isolator, minimising the feedback into the laser cavity.

Because of the need to be able to demodulate the detected signal at such a high frequency (360kHz) we had to design and build our own electronic system which could synchronously demodulate at both 180kHz and 360kHz. The designs are contained in Appendix 4.

7.3.2 Microscope Characteristics

We began by mounting a planar reflector on a piezo–electric bimorph and scanning it axially through focus. No dither was applied to the fibre tip and the axial response of Fig. 56 was achieved.

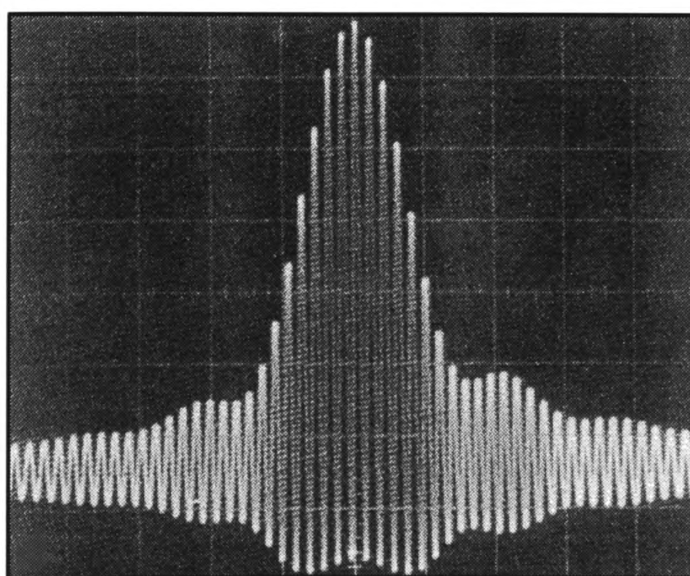

Fig. 56 Raw signal of the axial scan, obtained using 0.5NA lens. Horizontal scale: 1.5μm/div.

As discussed earlier, comparison with the theoretically modelled response of eqn (144), shown in Fig. 54, suggests that $r = 0.7$ and $a = 4$ in our experiment.

In order to obtain the real and imaginary parts of the interference term image we introduced a dither to the fibre tip by driving a piezo–electric cylinder at 180kHz which was near to its resonance. We were thereby easily able to adjust the modulation depth ϕ_0 to correspond roughly to the $J_1(\phi_0) \approx J_2(\phi_0)$ which makes the demodulated signals I_1 and I_2 comparable in size. Fig. 57 shows the result of demodulation at 180kHz where the interference term has been extracted from the complicated response of Fig. 56.

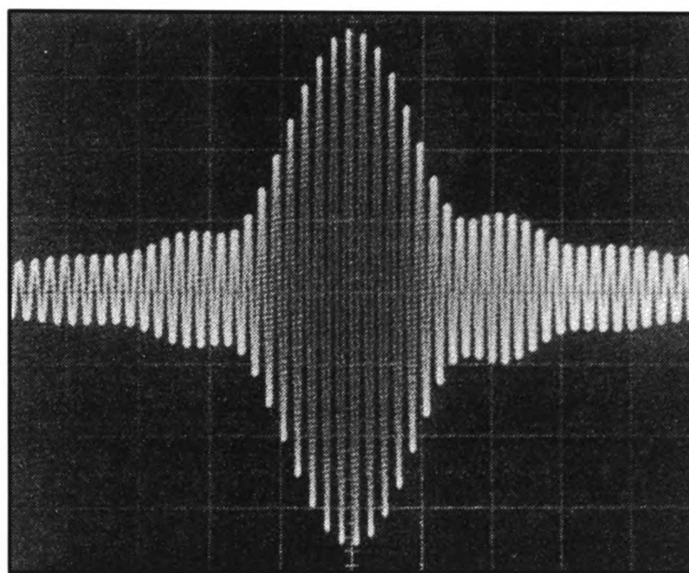

Fig. 57 Experimental axial scans using 0.5NA lens demodulated at 180kHz.
Horizontal scale: 1.5μm/div.

The theoretically modelled scan shown in Fig. 55 confirms that this is the response to be expected. The output from the 360kHz demodulator has the same form but with a $\pi/2$ phase shift in the fringe spacing. This is illustrated very clearly in Fig. 58 where we display both of the demodulated signals in the form of a Lissajous figure on an oscilloscope: the response takes the form of a spiral whose radius is proportional to the envelope of the axial response of Fig. 57. Thus the beginning of the outer point of the spiral corresponds to the focal position and the inner to the maximum axial scan position.

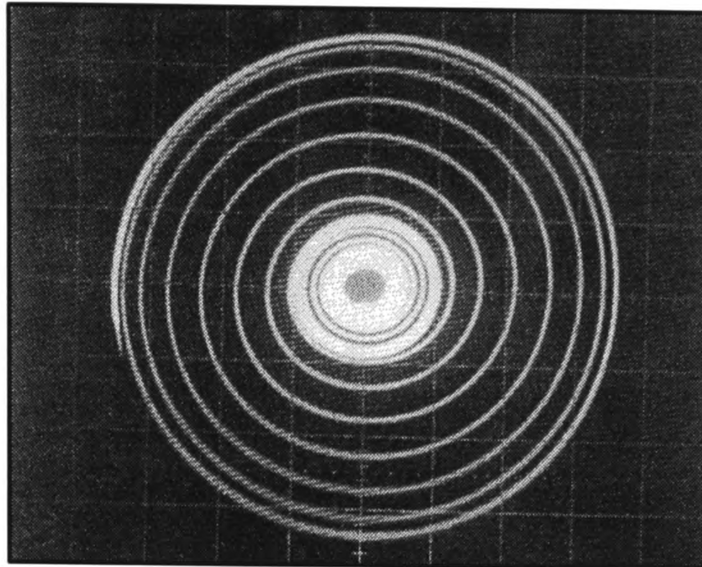

Fig. 58 x–y display of the two demodulated signals at 180 and 360kHz, proving that they are in quadrature.

Finally, by electronically squaring and adding the demodulated signals, the axial response in the more traditional form was obtained, Fig. 59(a). It was found to agree well with the theoretical prediction of $|\mathrm{sinc}(u/2 + ja/4)|^2$. In Fig. 59(b) we show the same axial response obtained by low–pass filtering (30kHz) of the photodiode signal after the modulation amplitude ϕ_0 was adjusted to give $J_0(\phi_0) = 0$, eqn (140). Both traces are very similar, as we would expect. It must be stressed, however, that although the latter technique apparently provides an easy way to obtain confocal images in the interference microscope, the phase information has been completely lost.

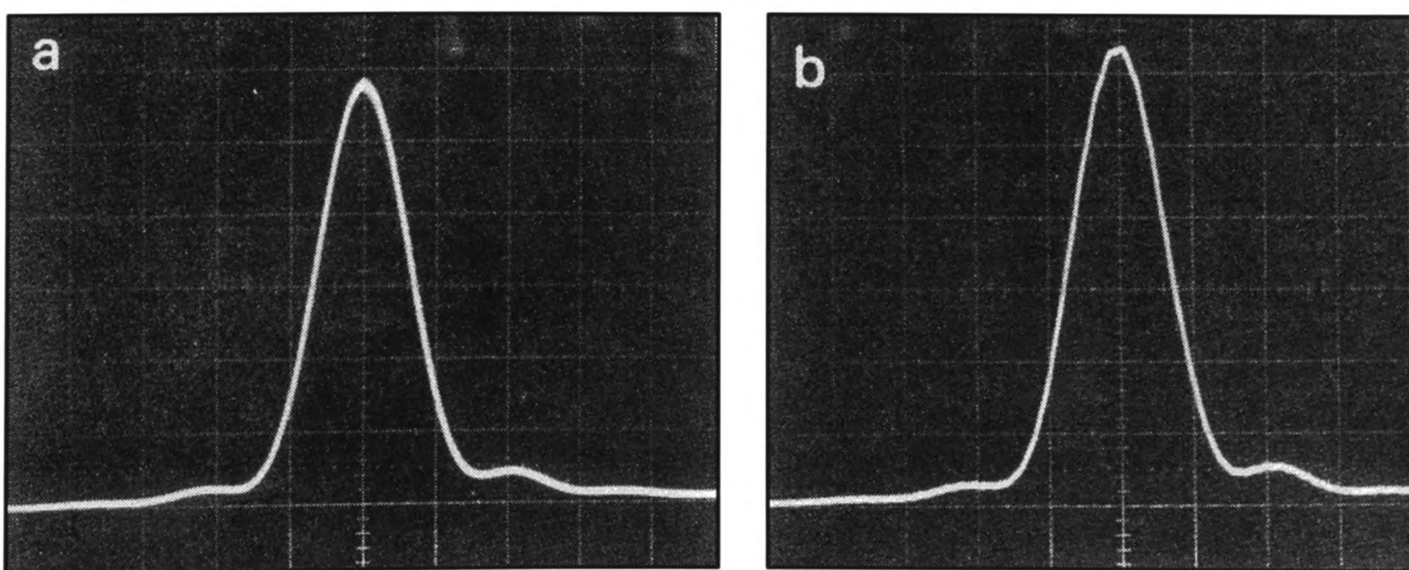

Fig. 59 Confocal axial responses obtained by
(a) squaring and adding the demodulated signals and
(b) low–pass filtering the photodiode signal.

7.3.3 Images

For imaging experiments we used a silicon test specimen (Agar Scientific S1934) containing a pattern formed by electron beam lithography. The pattern consists of a group of square lattices of silicon oxide on a silicon base. The lattice period is 10μm and we have chosen to image the edge of a lattice, showing some of the raised border.

The interference images of the specimen, obtained by demodulating the image signal at 180kHz (to obtain Im{U}) and at 360kHz (to obtain Re{U}) are shown in Fig. 60. The π/2 phase shift of the fringes between (a) and (b) is clearly visible.

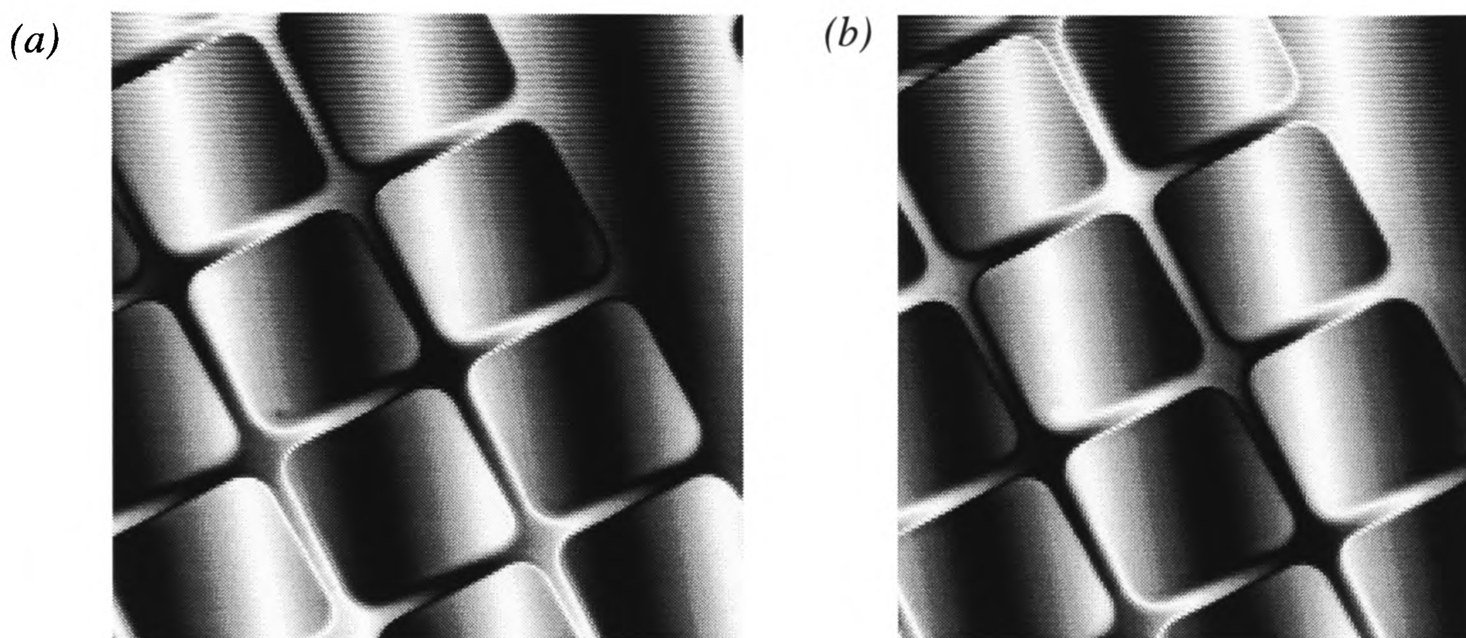

Fig. 60 Interference Images of the test specimen, pattern period is 10μm.
(a) Re{U} (b) Im{U}.

To obtain the confocal image of the specimen, it is now necessary to scale the images such that they have no constant offset and their dynamic ranges are identical. These images can then be squared and the results added together to give the confocal image, as was described earlier. Such an image is shown in Fig. 61.

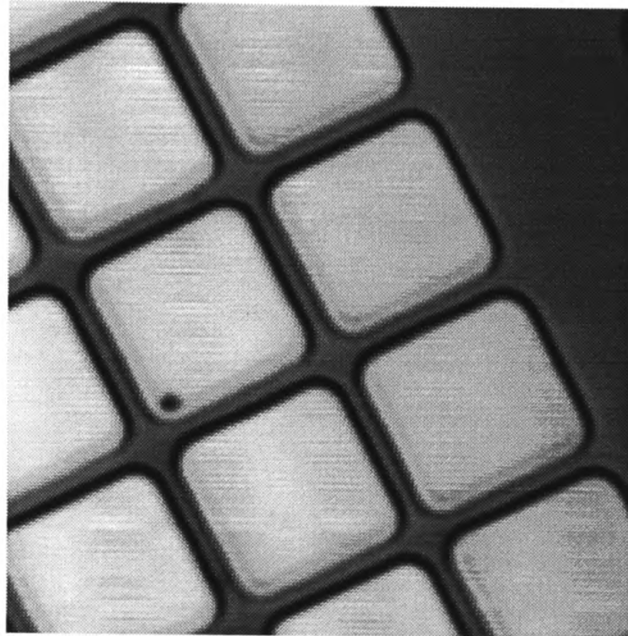

Fig. 61 Confocal Image of the test specimen, pattern period is 10μm.

The power of the interference imaging is best demonstrated by calculating the specimen's surface profile using independent readings of the amplitude and phase reflectivity. The amplitude reflectivity is obtained from the confocal image, Fig. 61. The phase term is, in turn, calculated by normalizing the demodulated signals using the confocal signal, combining the two signals into a complex reflectivity signal, eliminating the constant tilt factor and calculating the argument of the result. From this data, and with the assumption that the reflection takes place only at the specimen surface, we were able to calculate actual surface elevation of the specimen, plotted in Fig. 62. The height of the elevated pattern was found to be 115$\pm$5 nm.

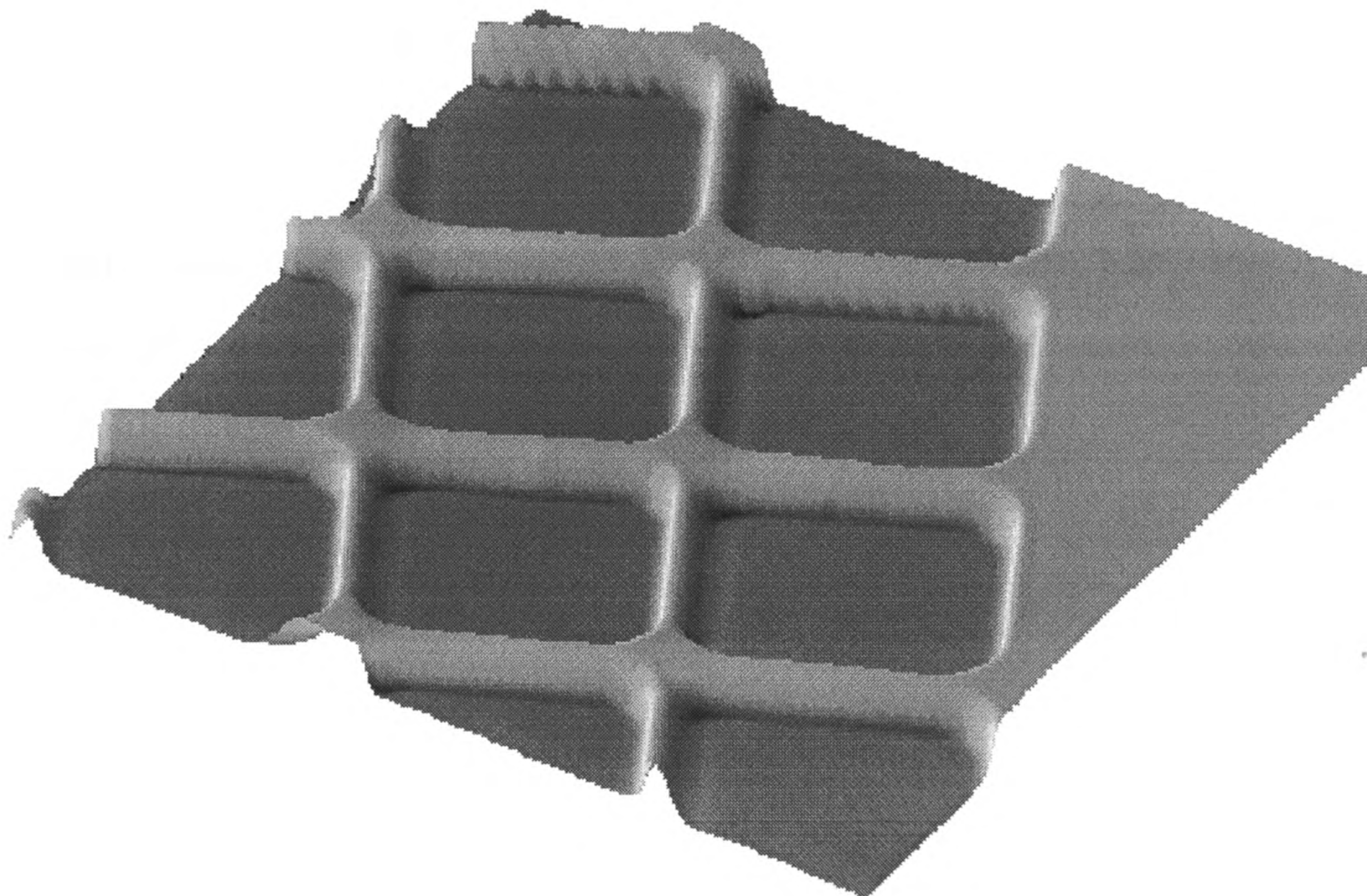

Fig. 62 Surface Profile of the same specimen.

7.4 Conclusions

In this chapter we have discussed a fibre–optic based confocal interference microscope. It retains many of the advantages of earlier microscopes presented in this thesis, such as simplified alignment due to reciprocal spatial filtering of both the reference and signal beams in the single–mode fibre. In addition, this scheme does not require a feedback control system and therefore does not suffer form the resulting stability problems. However some compactness has had to be sacrificed because of the need to minimize feedback into the laser which necessitated the re–introduction of a single mode optical fibre into the system. Also, as described, it is limited to imaging surface features which are less than $\lambda/2$ high, because of the 2π phase ambiguity resulting from the interference fringes. (This can however be overcome by using the optical sectioning information of the confocal image to remove the 2π phase ambiguity.)

The imaging was achieved using two interference signals in quadrature. Either could provide an interference image, but they could also be processed together to provide confocal or surface profile images. This was demonstrated experimentally.

8. Spatial Resolution

8.1 Introduction

A fundamental parameter of any microscope is the lateral resolution it can achieve. This can be defined as the minimum transverse distance between two objects which can just be distinguished in the image produced by the microscope. Ernst Abbe, who was the first to introduce the concept of the numerical aperture, was also the first to show that the lateral resolution of a microscope is proportional to the wavelength of the illumination and inversely proportional to the numerical aperture of the objective lens.

In the confocal microscope, however, we can consider axial or depth resolution as well as transverse or lateral resolution. We therefore briefly touch upon how depth resolution is measured and give values for the axial resolutions achieved by the microscope systems described so far. We then look at the lateral resolution of the different systems and, in particular, derive an expression for the lateral resolution of the profilometry systems at feature edges. The resolution is inherently non–linear in this case and we show that the highest resolution is achieved when the corrected height of the edge, h' ($h' = h\cos^2(\alpha/2)$, where h is the physical height of the feature), is $\lambda/4$. Experimental results are shown which support this calculation.

Finally we look at how variations in numerical aperture and detector size affect the profilometry systems.

8.2 Depth Resolution

The depth resolution of a confocal microscope can be calculated from the full–width–half–maximum (FWHM) of the axial response for a plane object, which was derived in Chapter 2 and expressed in eqn (36) as

$$I_d = \left\{ \frac{\sin\left(u/2\right)}{u/2} \right\}^2 \tag{145}$$

In Chapters 4 and 5 we saw that, providing it is not too large, the finite size of the coherent detector (a monomode optical fibre or laser) does not significantly affect the FWHM of the axial response. (Rather it slightly raises the intensity of those areas just out of focus, thus marginally reducing the depth discrimination.) We therefore do not need to include the imaginary term which models the finite detector size when calculating the FWHM of the axial response.

For the semiconductor laser systems described in Chapters 4 and 5, with the laser wavelength of 829nm and lens numerical aperture of 0.5, the depth resolution is about 2.67μ. In Chapters 6 and 7 we used a HeNe laser with wavelength 633nm and the same objective lens, which gave a confocal depth resolution of 2.04μ. However the interferometry techniques we used enabled us to achieve much higher depth resolutions of the order of nm. The sensitivities of these microscopes were, in fact, limited by the noise of the lasers being used, which was discussed in each case.

8.3 Confocal Lateral Resolution

In a confocal microscope the lateral resolution is given by the FWHM of the image of a single point object. It can be shown that the intensity distribution in the image plane which occurs when a point object is imaged by a confocal microscope with lenses which are circular and have equal numerical aperture is given by eqn (146) [8]

$$I(v) = \left(\frac{2J_1(v)}{v} \right)^4 \tag{146}$$

where v is the normalized lateral coordinate, $k\,r\sin\alpha$ (where r is the distance from the object in microns) and $J_1(v)$ is a first order Bessel function of v.

From this we can calculate that the 829nm semiconductor laser systems have lateral resolutions of 0.61μ and the confocal lateral resolutions of the 633nm HeNe laser microscopes are 0.47μ.

We now turn to consider what lateral resolution is achievable by the profilometry technique and in Section 8.4 we derive an expression for this.

8.4 Lateral Resolution for Profilometry

In order to derive an expression for the lateral resolution achievable by the profilometry techniques we have described, we revert to the Fourier imaging approach, outlined in Chapter 2. This permits us to express the confocal amplitude signal in terms of a coherent transfer function *c(m,u)* and the object spectrum (Fourier transform), *T(m)*. In particular

$$U(t,u) = \int_{-\infty}^{\infty} T(m)\ c(m,u)\ e^{jmt}\ dm \qquad (147)$$

where we have specialised to the case of a one–dimensional object, *m* is a normalised spatial frequency in the x–direction and *t* is a normalised optical co–ordinate which is related to the actual distance, *x*, via $t = k\,x \sin\alpha$. The transfer function *c(m,u)* is given by

$$c(m,u) = P(m,u) \otimes P(m,u) \qquad (148)$$

where the pupil function, *P* is given by eqn (149)

$$P(m,u) = \exp\frac{jm^2}{2}\left(u + \frac{ja}{2}\right)\exp\left(\frac{-ju}{4\sin^2\frac{\alpha}{2}}\right) \qquad |m| \le 1$$
$$= 0 \qquad \textit{otherwise} \qquad (149)$$

and the optical co–ordinate, *u*, denotes defocus, as $u = 4\ k\ z\ \sin^2\left(\frac{\alpha}{2}\right)$.

8.4.1 The Basic Theory

In order to investigate the spatial resolution of the system we elect to consider a specimen of uniform reflectivity whose height jumps by u_o optical units at $t = 0$. Our approach to modelling this object is to split it up into two objects. The defocus at the top surface is denoted by u_t and at the bottom by u_b. Thus

$$\tau(t) = u(t)\delta(u-u_b) + u(-t)\delta(u-u_t) \tag{150}$$

where $u(t)$ denotes the step function

$$\begin{aligned} u(t) &= 1 \qquad t > 0 \\ u(t) &= 0 \qquad t < 0 \end{aligned} \tag{151}$$

Thus if the microscope is focussed on the top surface, u_t, the bottom focus is automatically given by $u_b = u_t + u_o$. The Fourier transform of the object spectrum, $T(m)$, can now be calculated from eqn (150) (using the contour integral ([45] p 130)), giving

$$T(m) = \frac{1}{2}\left\{\delta(m) + \frac{1}{j\pi m}\right\}_{u_t} + \frac{1}{2}\left\{\delta(m) - \frac{1}{j\pi m}\right\}_{u_b} \tag{152}$$

After substituting eqn (152) into eqn (147) we can now write the total image as

$$U(t) = \frac{c(0,u_t) + c(0,u_b)}{2} + \frac{1}{\pi}\int_0^2 \left\{\frac{c(m,u_t) - c(m,u_b)}{m}\right\} \sin mt \, \mathrm{dm} \tag{153}$$

which, in general, has no simple solution. However if we specialise to the case when the step height is small we can make the approximation that

$$c(m,u) = \exp\left(\frac{-ju}{2\sin^2\frac{\alpha}{2}}\right)\exp\left(\frac{ju}{2}\right)c(m,0) \tag{154}$$

which direct calculation shows to be reasonable for small u. Setting $u_t = 4\ kh\sin^2\frac{\alpha}{2}$ and $u_b = 0$, we can re-write eqn (153) as

$$U(t) = \exp(-jkh')[\cos kh' + 2j\,f(t)\sin kh'] \tag{155}$$

where $h' = h\cos^2\frac{\alpha}{2}$ and h is the actual value of the step height. The spatially varying function *f(t)* is given by

$$f(t) = \frac{1}{\pi}\int_0^2 \frac{c(m,0)}{m}\sin mt\ \mathrm{dm} \tag{156}$$

where t is a normalised optical co–ordinate which is related to actual distance x, via $t = kx$ $\sin\alpha$. The function *c(m)* is the in–focus coherent transfer function which is given [8,9] by

$$c(m) = \frac{2}{\pi}\left\{\cos^{-1}\left(\frac{m}{2}\right) - \left|\frac{m}{2}\right|\sqrt{1-\left(\frac{m}{2}\right)^2}\right\} \tag{157}$$

Thus we obtain

$$\arg\{U\} = kh' - \tan^{-1}\{2f(t)\tan kh'\} \tag{158}$$

which for small kh' and noting that $|f(t)| \le 0.5$, permits us to write

$$\arg\{U\} = 2kh'\left\{\frac{1}{2} - f(t)\right\} \tag{159}$$

which is, of course, proportional to surface height, h. The spatially varying part in curly brackets is plotted in Fig. 63. The resolution, as measured by the 20%–80% width is $0.4\frac{\lambda}{\sin\alpha}$ which equals 0.3μm for HeNe light and a 0.85NA objective.

We note that the spatial resolution is improved by using a high numerical aperture objective whereas the height scale is proportional to $\cos^2\left(\frac{\alpha}{2}\right)$. However the drop in signal strength is not great, falling only by just over one half as we change from a numerical aperture of 0.5 to unity. We also observe that $\left\{\frac{1}{2} - f(t)\right\}^2$ is the image of a straight edge object in a confocal microscope [8,9].

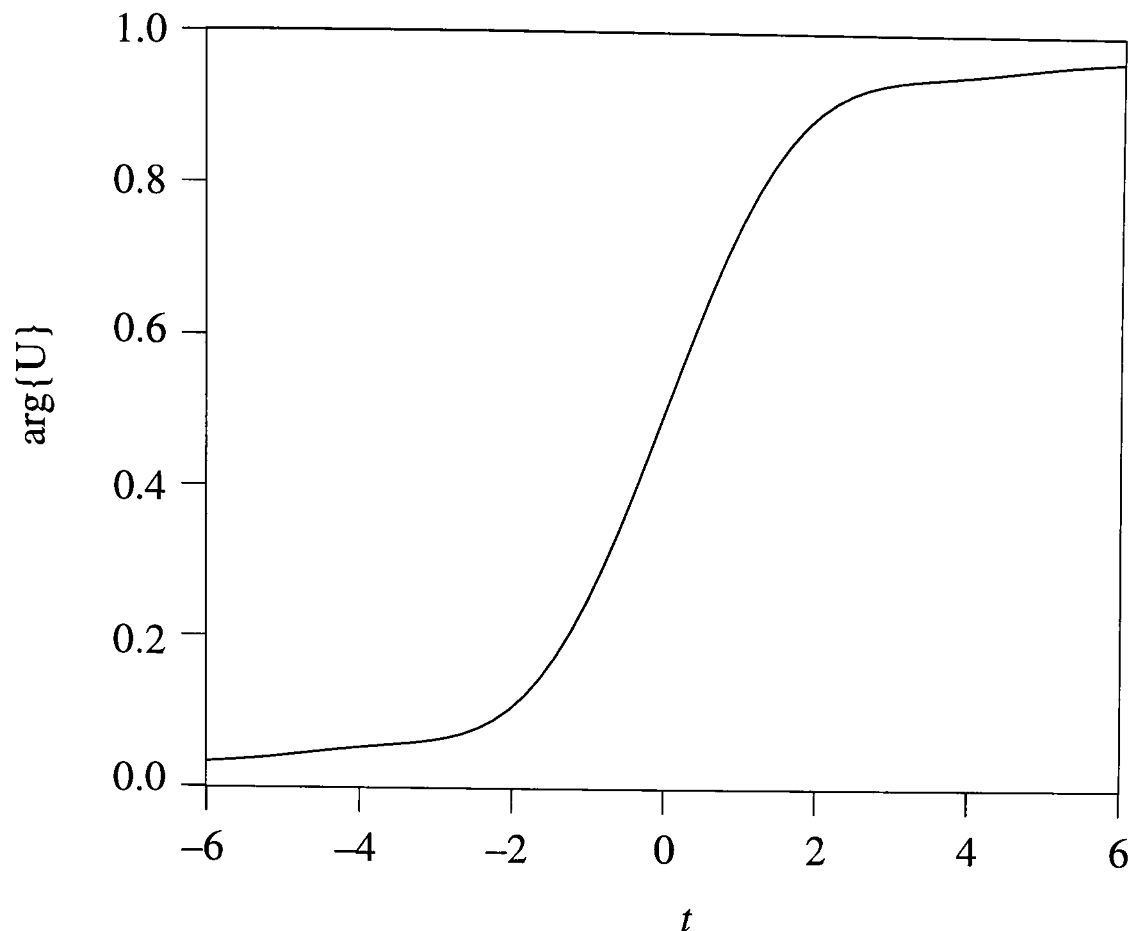

Fig. 63 The spatial variation in arg{ U } for the case of a small change in height.

8.4.2 Experimental Conclusions

The form of eqn (159) and Fig. 63 therefore predicts that surface profiles of high spatial resolution should be obtained when a feedback system is used to control the value of arg{ U } so as to set $\cos(\phi + \arg\{U\}) = 0$ or 1, as demonstrated in Chapter 6. We can also use eqn (155) and our assumptions about small step heights to set $|U(t)| \sim 1$ and write the interference image, as

$$I(t) = \cos\left\{\phi + 2kh'\left\{\frac{1}{2} - f(t)\right\}\right\} \tag{160}$$

Since kh' is small the form of this image will depend crucially on the value of ϕ. In particular, if we arrange to set $\phi = \frac{3\pi}{2}$ then it is easy to write, for small kh'

$$I(t) \sim 2kh'\left\{\frac{1}{2} - f(t)\right\} \tag{161}$$

Thus the interference image can be made to represent an uncalibrated height image. However the form of eqn (161) depended on careful choice of ϕ and a small step height. In general the image will not be so useful. Indeed some care is needed in interpreting such images

since although $\phi = \frac{3\pi}{2}$ predicts the correct profile, $\phi = \frac{\pi}{2}$ produces the opposite profile! In essence we introduce an offset such that the system response is linear in surface height, z.

8.5 The Limit of Lateral Resolution

Returning to eqn (155) we can see that there are two simple limiting forms of the expression. The first is when the step height is such that $\tan k_o h'$ is sufficiently small to permit us to write

$$\arg\{U\} = 2kh'\left\{\frac{1}{2} - f(t)\right\} \tag{162}$$

which is proportional to the step height, h, with a spatial resolution determined by $\frac{1}{2} - f(t)$. This function is plotted again in Fig. 64 (solid line), and the resolution (of $0.4\,\lambda\,/\sin\alpha$) corresponds to 0.6μm for a 0.5NA objective lens with the 788nm wavelength semiconductor laser which we used to investigate the resolution limits.

If we now consider phase steps such that kh' approaches $\frac{\pi}{2}$ then we see that $\tan kh' \rightarrow \infty$. We further recall that $f(t)$ is a smoothly varying function which tends to $-\frac{1}{2}$ as $t \rightarrow -\infty$ and $+\frac{1}{2}$ as $t \rightarrow +\infty$. This permits us to write

$$\arg\{U\} = \frac{\pi}{2}\{1 + \mathrm{sgn}(t)\} \tag{163}$$

where $\mathrm{sgn}(t) = 1$ $(t > 0)$ and -1 $(t < 0)$. This function has an extremely sharp transition at $t = 0$, and gives the impression that super–resolution may be achieved [46,47]. However this is not really the case and arises, essentially, because of the non–linear form of eqn (158).

The function of fundamental importance is the image amplitude, U, and the spatially varying part of this is $f(t)$, which does not exhibit super–resolution. Fig. 64 shows the theoretical model of the phase images for a variety of step heights where $0 < k_o h' < \frac{\pi}{2}$. It is clear that

great caution should be exercised in quantifying the resolution of such images. We further note that if we consider step heights in the region $\frac{\pi}{2} < kh' < \frac{3\pi}{2}$ then we find, eqn (158), that the phase tends to a maximum as $t \rightarrow -\infty$ and zero as $t \rightarrow +\infty$, i.e. the opposite behaviour to that shown in Fig. 64.

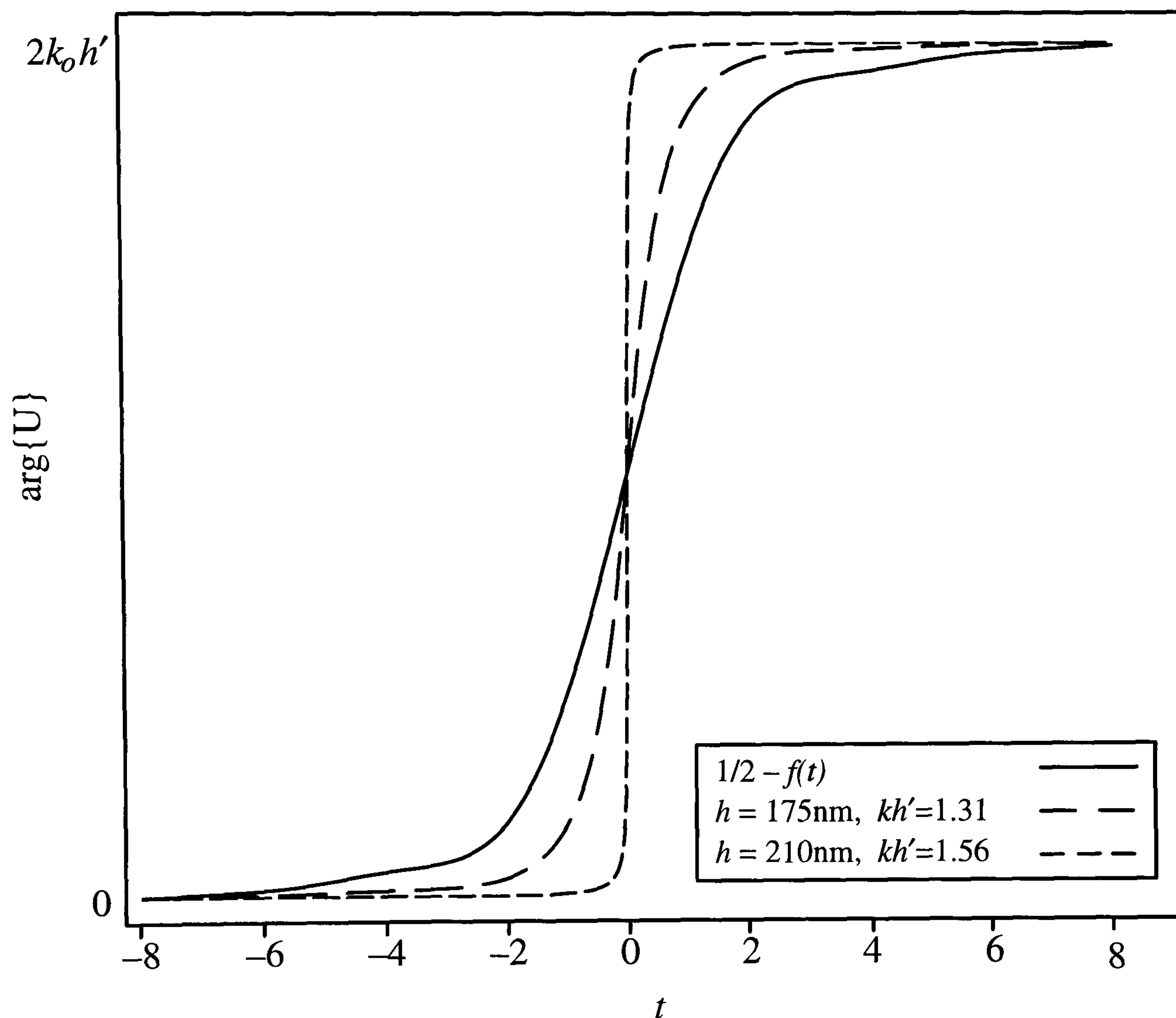

Fig. 64 The spatial variation in arg{U} for different heights of step. The responses shown are for very small step heights (solid line), 175nm and 210nm step heights.

Fig. 65 and Fig. 66 show line scans over edges of the two specimens used in the next chapter. The experimental line scans are displayed as diamonds with the theoretical fits determined by eqn (158) superimposed and showing excellent agreement in both cases. We find that the resolution, as measured between the 20 – 80% intensity values is 0.6μm for the 12nm high edge which agrees well with the limiting theoretical value (0.4 $\lambda/\sin\alpha$). The resolution in the 186nm high case on the other hand, Fig. 66, is 0.2μm. As we have already stated, we attribute this apparent 'super–resolution' to the inherently non–linear nature of phase imaging.

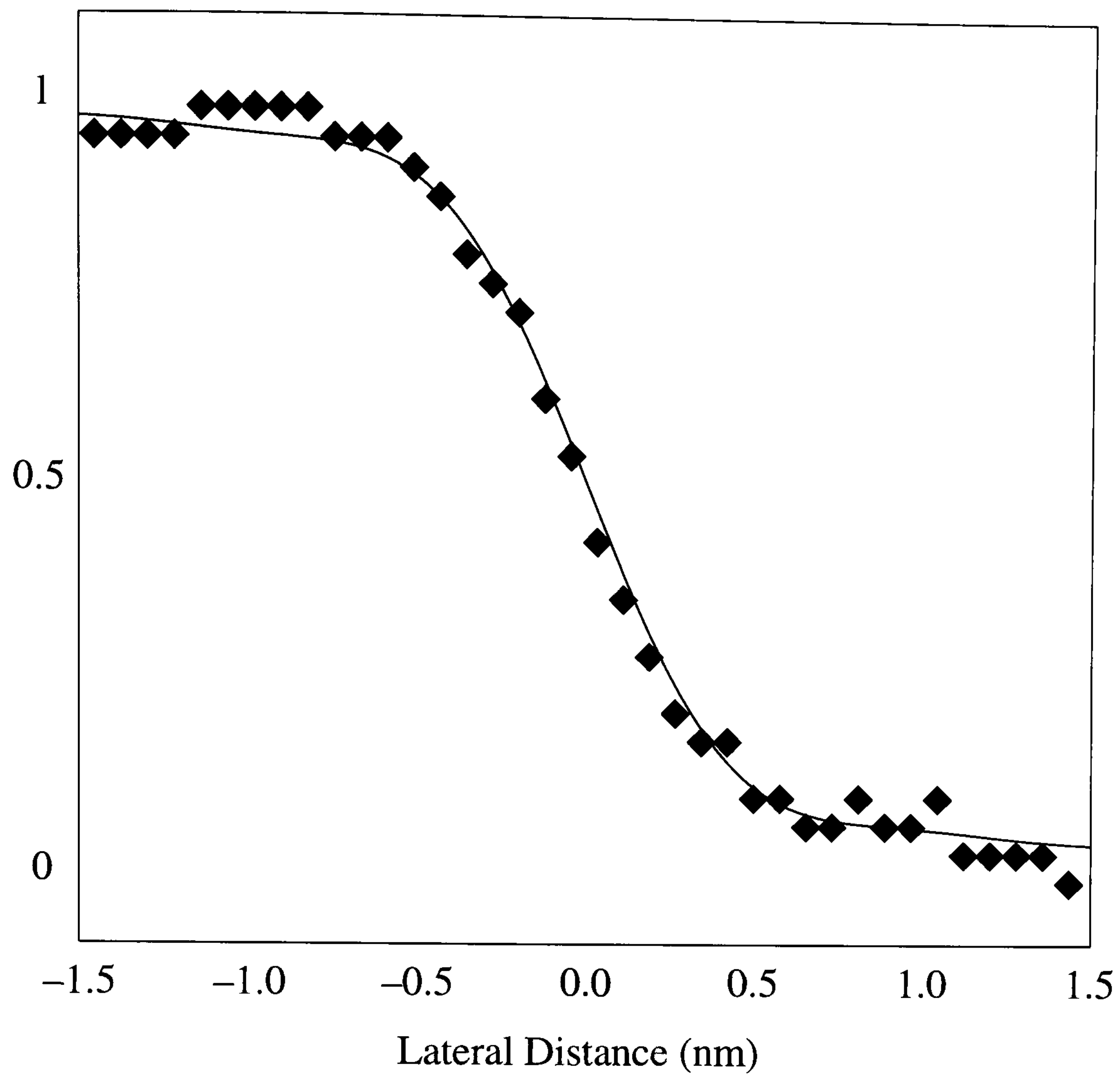

Fig. 65 Experimental and theoretical line scans across a phase edge of height 12nm ($kh' = 0.028\,\pi$).

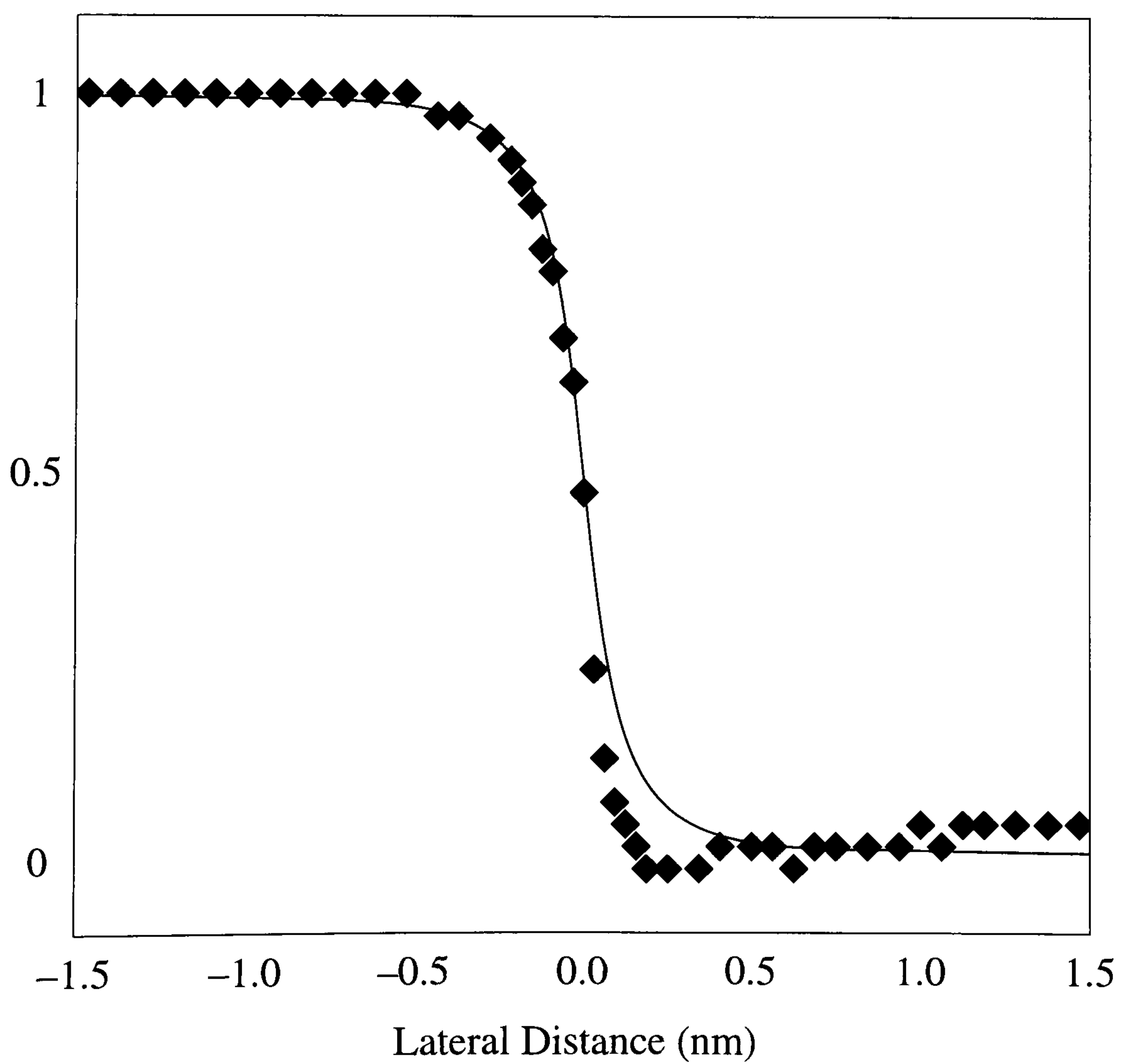

Fig. 66 Experimental and theoretical line scans across a phase edge of height 186nm ($kh' = 0.44\,\pi$).

8.6 The Effect of Numerical Aperture

To model the axial response of the microscope for a plane object we refer back to the expression derived in Chapter 6, eqn (128), for a planar reflector

$$I(u) \propto \mathrm{Re}\left\{ \exp\left(-2jkz\cos^2\frac{\alpha}{2}\right) \mathrm{sinc}\left[\frac{1}{2}\left(u + \frac{ja}{2}\right)\right]\right\} \tag{164}$$

where the numerical aperture, sin α, affects the optical axial unit u, according to $u = 4\ k\ z\ \sin^2\frac{\alpha}{2}$, as well as the fringe term.

Fig. 67 shows the experimental axial responses for a variety of numerical apertures (with the fill factor, $a = 1.2$) obtained with the experimental setup schematically illustrated in Fig. 35. Beside them are the theoretically modelled curves obtained from eqn (164). They are all normalised to unity when $kz = 0$, and are plotted for $a = 1.2$ so as to be comparable to the experimental results presented in Fig. 67.

The zero numerical aperture case is included since the fringe spacing is $\frac{\lambda}{2}$ which provides a useful calibration of our z movement. The non–zero value of a serves both to smooth out the overall envelope of the axial response and to make the fringe spacing dependent on kz. We can easily see this if we assume that a is sufficiently large, such that $\exp\ 2a \gg 1$.

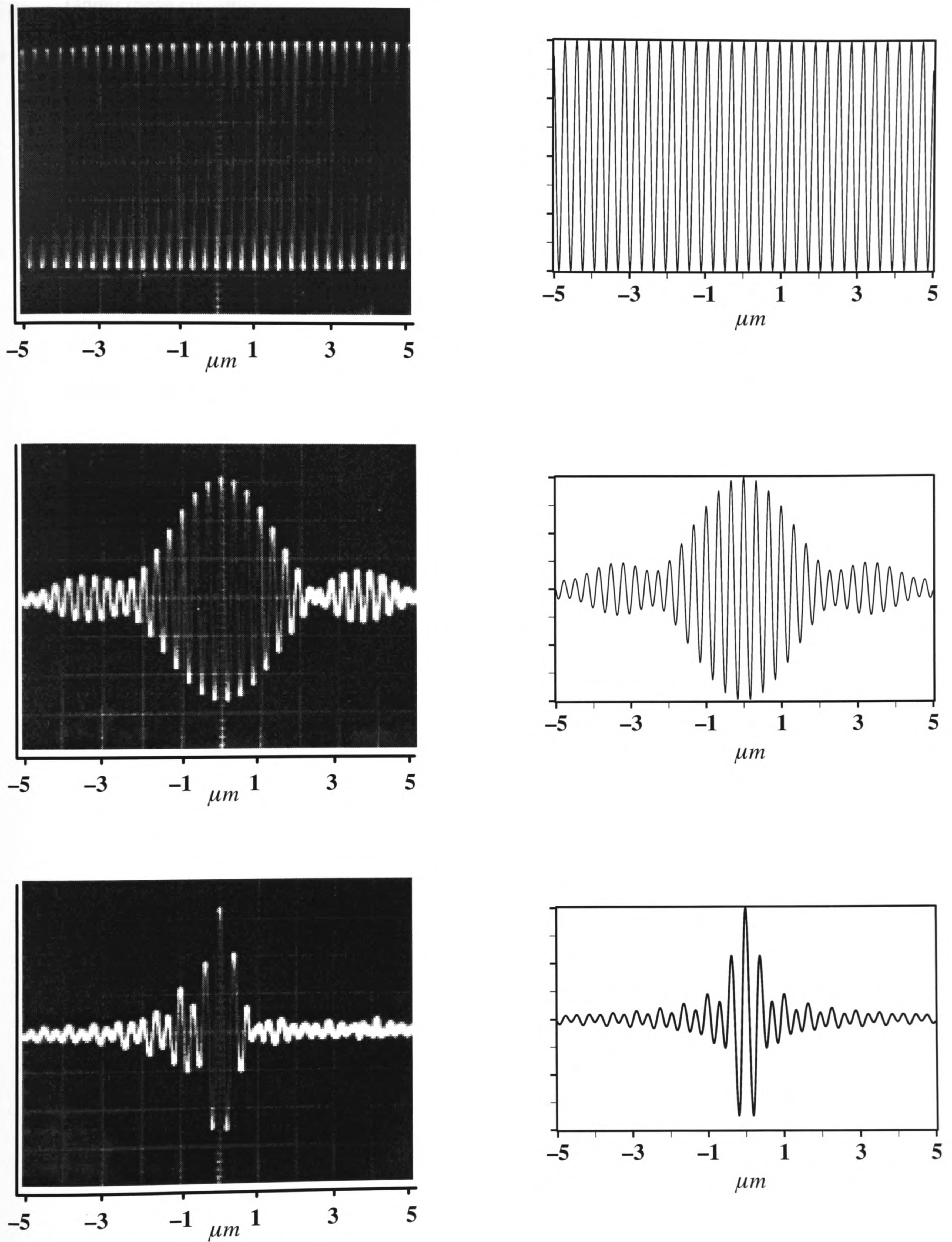

Fig. 67 Theoretical and experimental axial responses of the microscope with $a = 1.2$ and all curves are normalised to $I(0) = 1.0$. a) NA = 0 (unfocussed beam), b) NA = 0.5, c) NA = 0.85.

Under these circumstances, eqn (164) predicts that the fringe pattern, normalised to unity at $u = 0$, is given by $\cos(2kz)$ for small kz. On the other hand when $u(kz)$ becomes large the fringe pattern becomes $\sin(2kz)$ i.e. there is a $\frac{\pi}{2}$ phase shift but no change in period. The phase shift can be seen in Fig. 67 although the large a approximation is not strictly applicable in our case. We emphasise this in Fig. 68 where we plot the width of the first fringe as a function of a for a variety of values of numerical aperture. We see that at high values of numerical aperture the fringe width is particularly sensitive to the value of a. For the specific case of $a = 1.2$, which corresponds to our experimental conditions Fig. 68 suggests that the fringe spacing for the 0.5 NA objective should be 1.05 times wider than the zero NA case and 1.18 wider in the 0.85 NA case. In practice fringe spacings were found to increase by 1.03 ± 0.02 (0.5 NA) and 1.18 ± 0.02 (0.85 NA).

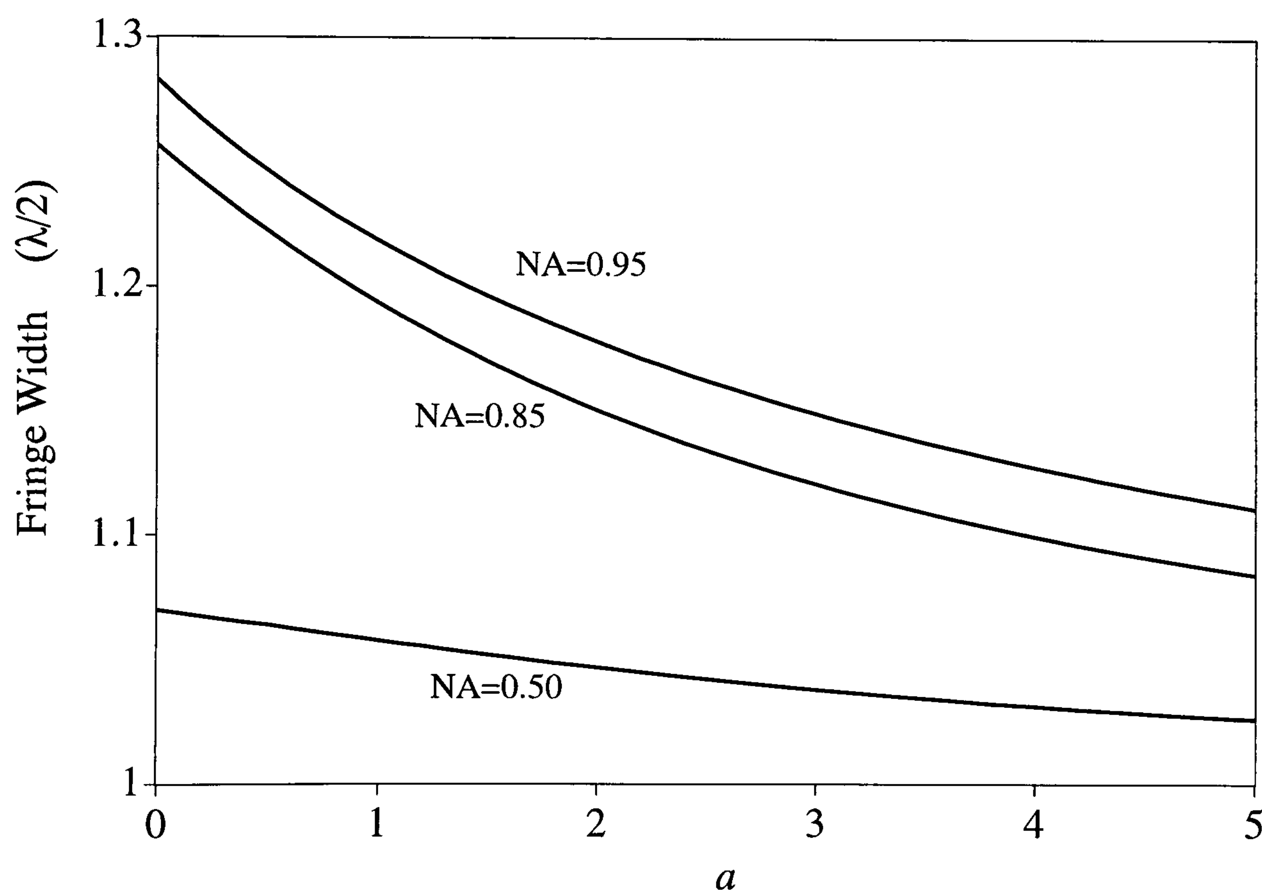

Fig. 68 The width of the first fringe of the axial response as a function of the parameter a for various values of numerical aperture.

8.7 Conclusions

Having first looked at the depth and lateral resolutions of the confocal systems which we have considered in earlier chapters, we considered in some detail the lateral resolution of the profilometry systems we have developed. We have shown that the lateral resolution which could be achieved can be expressed as $0.4\frac{\lambda}{\sin\alpha}$, and that, for small variations in height, the variation in intensity can be expressed as

$$I(t) = \cos\left\{\phi + 2kh'\left\{\frac{1}{2}-f(t)\right\}\right\} \tag{165}$$

where $f(t)$ is given by eqn (156).

We have also shown that the lateral resolution is inherently non–linear and that the gradient of the response at the edge approaches infinity when the corrected height of the edge, h' ($h' = h\cos^2(\alpha/2)$ where h is the physical height of the edge), approaches $\lambda/4$. This was confirmed experimentally.

We also considered the effect of varying the numerical aperture of the objective lens of the microscope. We showed both theoretically and experimentally that the numerical aperture strongly affects the optical sectioning ability of the system. Furthermore, we show that the numerical aperture and the finite size of the detector both affect the spacing of the fringes in an axial scan through the focus of the optical system.

9. Semiconductor Laser Confocal and Interference Microscopy

9.1 Introduction

In Chapters 6 and 7 we looked at two systems which can produce both confocal and interference images and in both cases the interference images were used to yield surface profiles of the specimens being observed. In both systems a HeNe laser was used to provide an imaging beam with sufficient coherence length to achieve interferometry, and the modulation of the relative optical path lengths between the two arms of the interferometer was achieved either by using an electro–optic modulator or by mechanically dithering the tip of an optical fibre. In this chapter we turn to consider a system which can achieve the same results but with a semiconductor laser and with an entirely different means of modulation – varying the wavelength.

As is clear in Chapters 6 and 7, it is necessary to introduce a relative phase modulation in order to extract the interference term image. As before, this may be achieved mechanically [48], which is usually slow, or electro–optically which involves the use of a bulky, high voltage, element [49,50]. However by using a semiconductor laser we can exploit the dependence of its wavelength on injection current to dither the wavelength and thus introduce the required modulation [51]. This approach removes the need for a mechanical or electro–optic dither and has the further advantage that no further optical elements need to be introduced into the system.

In this chapter we show that it is possible to use this phase modulation technique in a semiconductor laser based confocal fibre–optic interferometer. We show that it can produce images similar to those produced by the HeNe laser interferometers already described. We also demonstrate the versatility of the semiconductor laser microscope by showing that it

can achieve pure confocal imaging rather than interference imaging simply by reducing the injection current into the laser.

9.2 Theoretical Basis

The key elements of this optical system are shown in Fig. 69. As in Chapter 7, the single mode fibre serves both to launch the light into the microscope and to detect the reflected confocal field amplitude, U. Again reflection from the fibre tip provides the reference beam and both the object and reference waves propagate together back along the fibre and ultimately interfere on the photodiode detector. As a result, the only non–common path part of the of the system is that between the fibre tip and the object.

The detected signal is given by

$$I = |r + U\exp(-2jkl)|^2 \tag{166}$$

where the phase factor $\exp(-2jkl)$ has been introduced to take account of the relative phase difference between the two beams which results from the fact that the interferometer is not entirely common path.

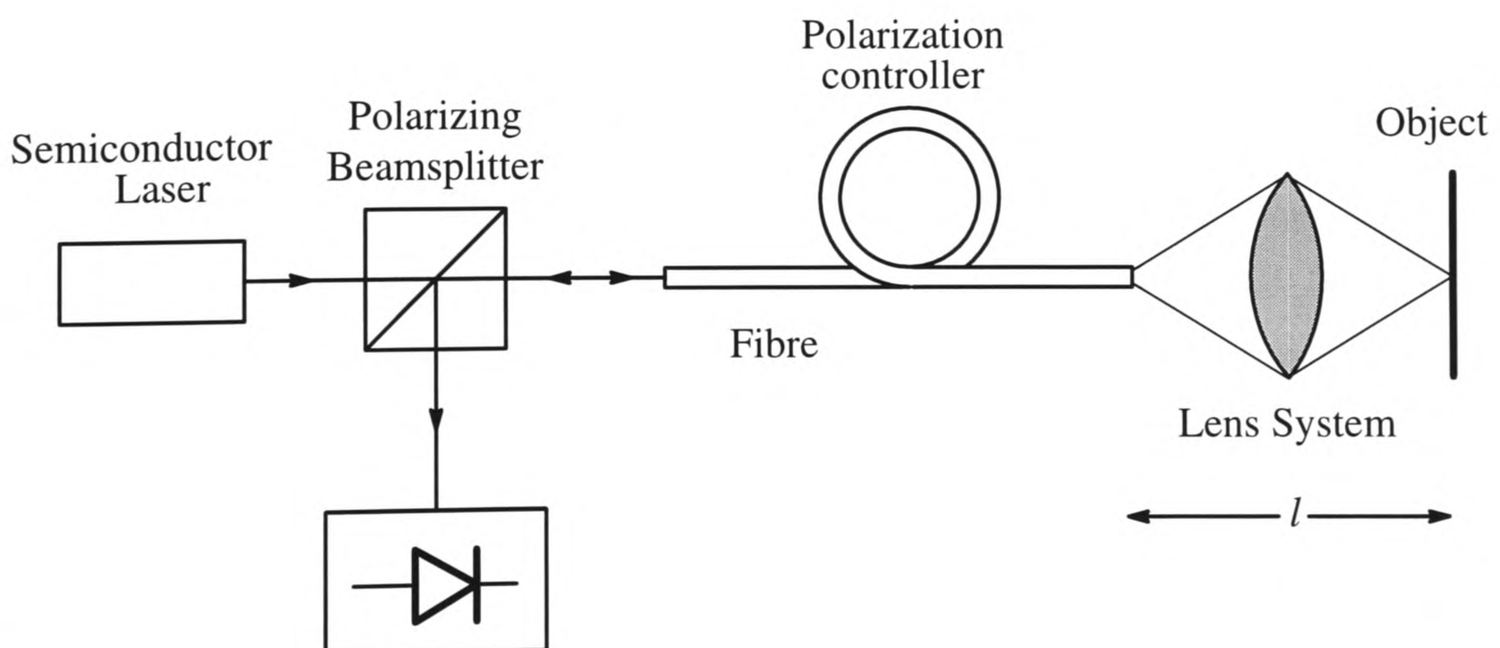

Fig. 69 Schematic Diagram of the Microscope Optics.

In order to separate out the interference term image from the confocal image $|U|^2$ and the constant background $|r|^2$ we elect to modulate the injection current of the semiconductor laser harmonically such that the wavelength is also modulated harmonically. This permits us to write

$$k = k_0 + (\Delta k)\cos\omega t \tag{167}$$

where k_o is evaluated at the nominal laser wavelength, Δk represents the modulation depth and ω is the modulation frequency. We may now rewrite eqn (166) as

$$I = |r + U' \exp{-j\phi(t)}|^2 \tag{168}$$

where $U' = U \exp(-2jk_o l)$ and the phase $\phi(t)$ is given by

$$\phi(t) = 2l\ (\Delta k)\cos\omega t \tag{169}$$

As we shall see later the actual value of Δk depends on the specific value of injection current modulation used. However it will suffice for the moment to take a typical value of, say, $2\text{x}10^{-5}\mu\text{m}^{-1}$, which, together with an optical length, l, of 16cm, shows that a phase modulation of the order of 2π radians can easily be achieved.

The confocal image field, U, is itself a function of wavelength via eqn (31) from Chapter 2.

$$U = h_{eff}^2 \otimes t \tag{170}$$

where t represents the object amplitude reflection coefficient and h_{eff} is the effective amplitude point spread function which is given by the Fourier–Bessel transform of the pupil function for the objective lens used in a reflection system

$$h \sim k \int_0^1 P(u,\varrho)\ \mathrm{J}_0(v\varrho)\ \varrho\ d\varrho \tag{171}$$

in which $P(u,\varrho)$ represents the pupil function of the lens (eqn (37)).

$$P(u,\varrho) = \exp\frac{j\varrho^2}{2}\left(u + \frac{ja}{2}\right)\exp\left(\frac{-ju}{4\sin^2\frac{\alpha}{2}}\right) \qquad |\varrho| \leq 1$$
$$= 0 \qquad \textit{otherwise} \tag{172}$$

The optical co–ordinates u and v are related to real axial co–ordinate z and radial co–ordinate r as defined before, ie

$$u = 4\ k\ z\ \sin^2\left(\frac{\alpha}{2}\right)$$
$$v = k\ r\sin\alpha \tag{173}$$

We note that for the small value of Δk ($10^{-5}\mu m^{-1}$) in comparison with k_o (= $7.97\mu m^{-1}$ for a 788nm laser) it is reasonable to replace k by k_o in the pre–multiplying factor and in the definitions of u and v. This is permissible even in the phase factor, $\exp j\frac{u\varrho^2}{2}$, since the maximum value of $\exp\left(2j(\Delta k)\varrho^2 z\ \cos\omega t\ \sin^2\frac{\alpha}{2}\right)$ is $\exp j(\Delta k)z$ for a numerical aperture of unity. We recall that z is likely to be in the micron region and so $\Delta k\ z$ will always be very small so that it is reasonable to set $\exp j(\Delta k)z = 1$.

We are now almost in a position to write an expression for the image intensity but we must first remember that modulating the injection current not only leads to a frequency modulation but also to an intensity modulation. If we include this effect in eqn (168) and eqn (169) we obtain

$$I = (1 + \beta\cos\omega t)\left|r + U'\exp\left(-j\phi_0\cos\omega t\right)\right|^2$$
$$= (1 + \beta\cos\omega t)\left(r^2 + |U|^2 + 2r\left[\mathrm{Re}\{U'\}\cos\left(\phi_0\cos\omega t\right) + \mathrm{Im}\{U'\}\sin\left(\phi_0\cos\omega t\right)\right]\right) \tag{174}$$

We have introduced β to represent the intensity modulation and $\phi_o = 2(\Delta k)l$. We have also assumed, for simplicity, that r is real.

Since our intention is to extract the interference term image from eqn (174) it is tempting to carry out synchronous demodulation. In essence this involves multiplying eqn (174) by

$\cos\omega t$ and time averaging the result. This is relatively straightforward to do using the results shown earlier in eqn (140) and leads to a signal, I_ω, of the form

$$I_\omega \sim \beta\left[|U|^2 + r^2\right] + 2r\left[2J_1(\phi_0)\,\mathrm{Im}\{U'\} + \beta\left(J_0(\phi_0) - J_2(\phi_0)\right)\mathrm{Re}\{U'\}\right] \quad (175)$$

which may be recast as

$$I_\omega \sim \beta\left[|U|^2 + r^2\right] + 2rN\,|U|\,\sin\left[\arg\{U\} - 2k_0 l + \delta\right] \quad (176)$$

where the constants N and δ are given by

$$\sqrt{4J_1^2(\phi_0) + \beta^2\left(J_0(\phi_0) - 2J_2(\phi_0)\right)^2} \quad \text{and} \quad \tan^{-1}\left\{\frac{\beta\left(J_0(\phi_0) - J_2(\phi_0)\right)}{2J_1(\phi_0)}\right\}$$

respectively.

We can see that an undesirable side effect of the intensity modulation, β, is the presence of the confocal image, $|U|^2$, along with the required interference term image. We can overcome this drawback by performing the demodulation at a frequency, 2ω. In this case we obtain

$$I_{2\omega} \sim 2J_2(\phi_0)\,\mathrm{Re}\{U'\} - \beta\left(J_1(\phi_0) - J_3(\phi_0)\right)\mathrm{Im}\{U'\} \quad (177)$$

which may be recast as

$$I_{2\omega} \sim |U|\cos\left[\arg\{U\} - 2k_0 l - \psi\right] \quad (178)$$

where the constant phase factor ψ is given by $\tan^{-1}\left\{\beta\left(J_3(\phi_0) - J_1(\phi_0)\right)/\ 2J_2(\phi_0)\right\}$. This demodulated signal now represents the pure interference term image which consists of a fringe pattern superimposed on a confocal modulus image. We note that in this case the only effect of the intensity modulation has been to introduce a constant phase shift, ψ, into the fringe pattern.

It is now possible, in principle, to extract both $|U|$ and $\arg\{U\}$ from the two demodulated signals I_ω and $I_{2\omega}$. However this is impractical because of the complicated form of I_ω as shown in eqn (176), and the need to accurately determine parameters such as β, r, ϕ_o. The alternative is to introduce some additional, controllable, phase difference, $\Delta\phi$, between the object and reference beam such that eqn (178) becomes

$$I_{2\omega} \sim |U| \cos\left[\arg\{U\} - \Delta\phi - 2k_0 l - \psi\right] \tag{179}$$

We could then use the feedback technique to set $\Delta\phi$ such that, at each picture point, the cosine term in eqn (179) remains zero or unity. In this way the variations in $\Delta\phi$ are proportional to variations in $\arg\{U\}$, since $2k_o l + \psi$ merely represents a constant phase factor which does not depend on the object. As mentioned in the introduction to this chapter, we chose to effect $\Delta\phi$ by changing the laser injection current. This leads to a small change, Δk_o, in wavevector (of the order of Δk) and hence $\Delta\phi = 2(\Delta k_o)l$.

In order to discuss the ability of the system to perform surface profilometry we begin by considering the signal from a perfect reflector. From the usual result from Chapter 2, eqn (37), we know that arg $\{U\}$ is proportional to z. Hence a feedback system which tracks variations in arg $\{U\}$ will provide a surface profile.

We have now suggested a method to obtain arg (U), so it now merely remains to obtain $|U|$. This may be achieved, in principle, from our demodulated signals or by using a more sophisticated modulation feedback technique [51]. However there are problems in practice if the specimen feature height changes too rapidly. In a semiconductor laser implementation on the other hand we can avoid these problems altogether by simply reducing the injection current to the point where the coherence length is too short to allow interference to take place between the object and reference beams. In this case eqn(166) takes the form

$$I = |r|^2 + |U|^2 \tag{180}$$

from which the confocal signal $|U|^2$ can be readily obtained.

9.3 Experimental Technique and Results

9.3.1 Experimental Details

The basis of the optical arrangement which we used is shown schematically in Fig. 69. Light from a single frequency semiconductor laser (Sharp LT021MD, 20mW operating output power, 788nm wavelength) was passed through a polarising beam splitter into a single mode optical fibre (York SM600). This was then coupled into the confocal microscope from the distal end of the fibre. Since we did not index match the output end of the fibre, the light reflected from it formed the reference beam. As mentioned earlier, the object scanning was achieved by mechanical scanning in the x and y directions whereas a piezoelectric bimorph was used for the z–scan to obtain the axial responses. A 0.5 numerical aperture Leitz objective lens was used throughout. The confocal amplitude signal travelled back along the fibre together with the reference beam and these were finally allowed to interfere on the photodetector. The purpose of the polarization controller was to ensure that the light coupled to the microscope was circularly polarized with the result that the reflected signals, after passing through the fibre, were polarized orthogonally to the laser waveform and were completely reflected by the beamsplitter towards the photodiode. The input end of the fibre was also cleaved at about 10° to reduce the effect of reflections from the fibre holder. In these ways we endeavoured both to maximize the image signal and to reduce laser feedback effects.

9.3.2 Confocal Imaging

We began by confirming that at a sufficiently low injection current the system behaved as a non–interference confocal microscope. In order to do this we mounted a planar reflector on the piezo–electric bimorph and measured the detected signal as we scanned the mirror through focus. The threshold injection current was found to be 47mA and the axial response of Fig. 70 was obtained by operating the laser with an injection current of 52mA. This value was chosen since it provided an adequate signal to noise ratio and the system did not show any interference effects. This axial scan was theoretically modelled using eqn

(38) from Chapter 2, and shown in Fig. 70 where the theoretical fit is superimposed on the experimental result.

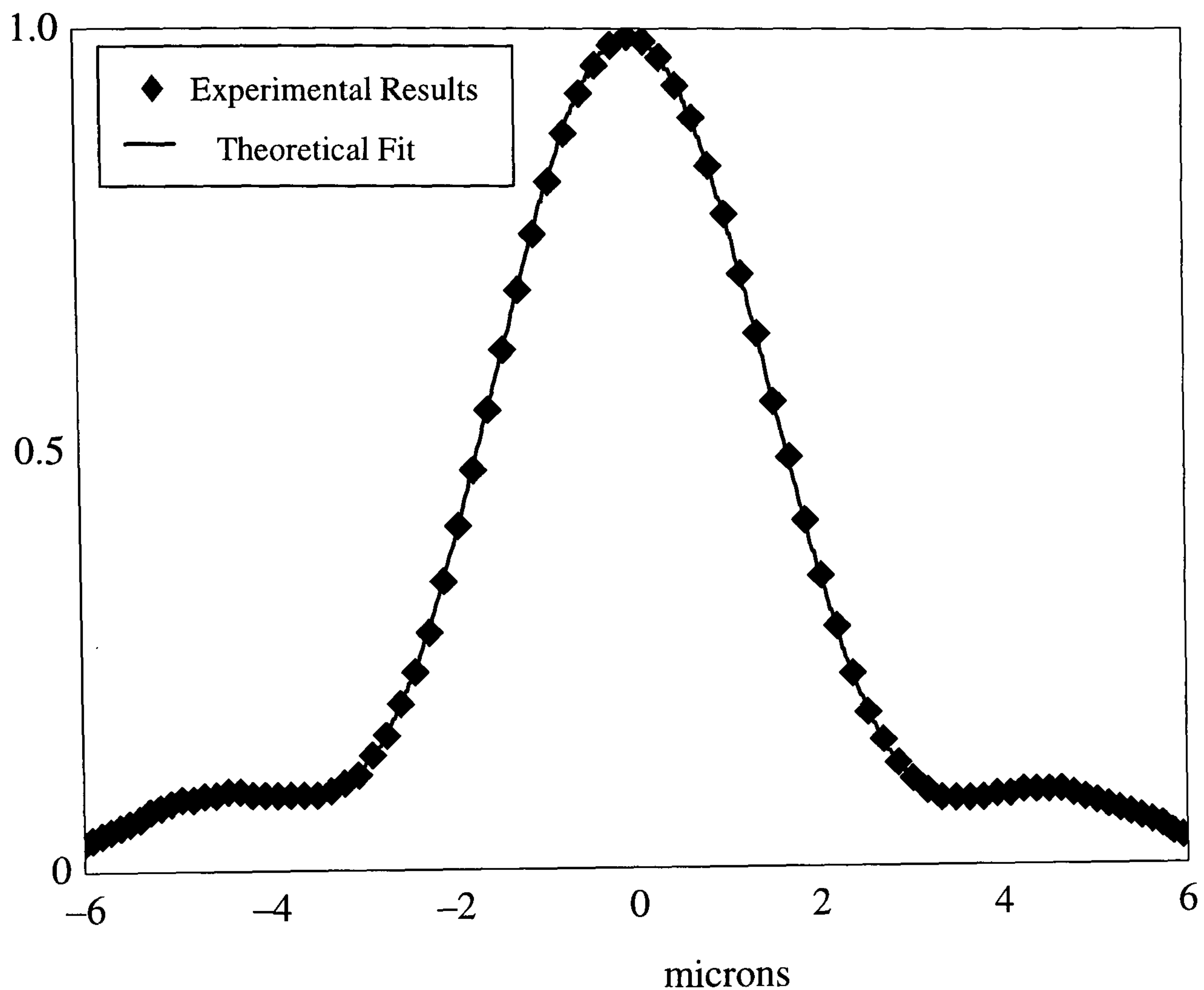

Fig. 70 The Axial response as a planar reflector is scanned through focus.

We allowed both a and the numerical aperture to be free parameters. The best fit was obtained for $a = 3.49$ and a numerical aperture of 0.47 rather than the nominal value of 0.5.

Fig. 71 shows a through–focus series of images of a portion of a microcircuit to confirm that high quality non–interference confocal images may be obtained with the system.

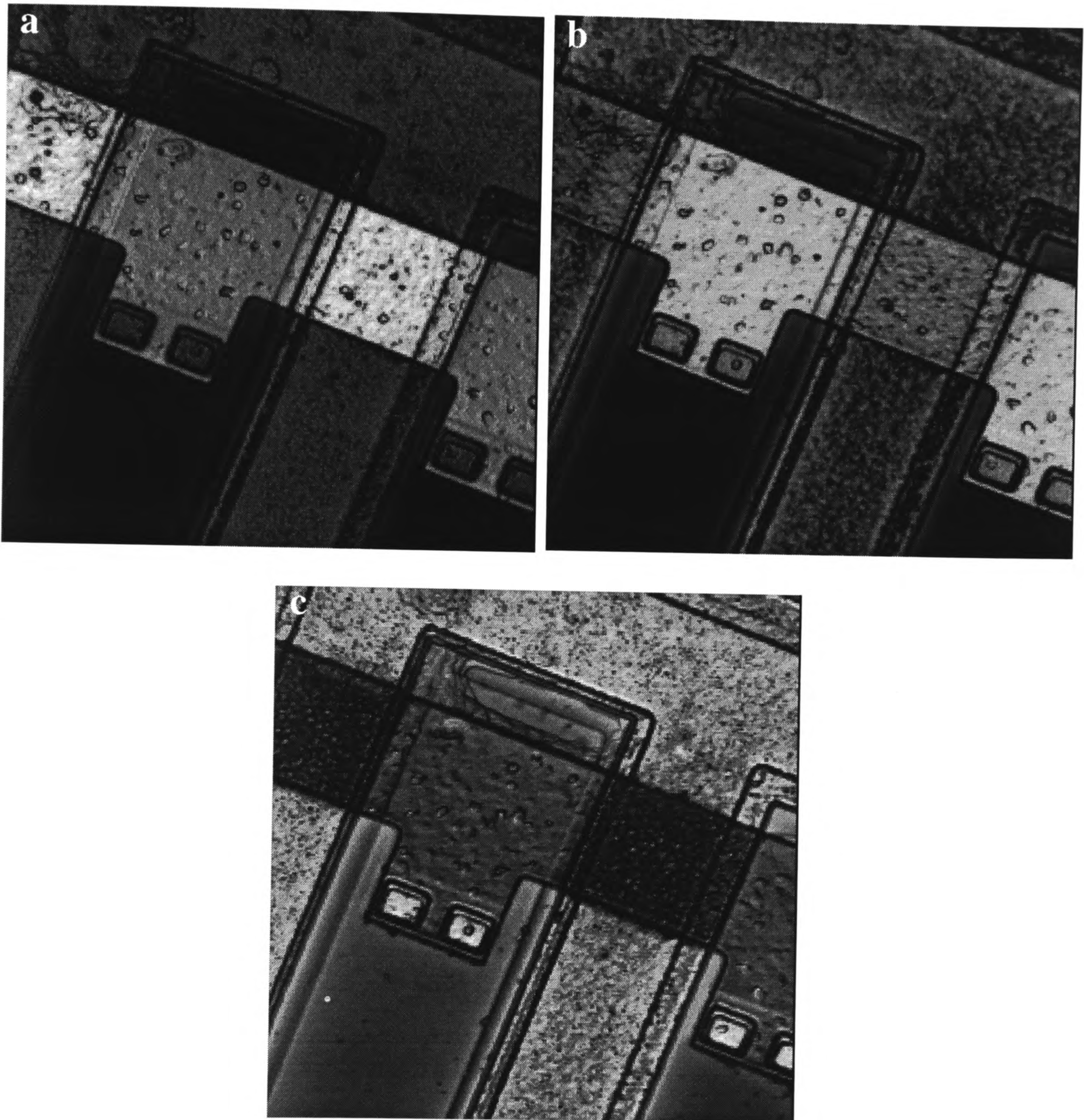

Fig. 71 Confocal images of a semiconductor chip, taken at 3 different axial positions. Relative to image (a), image (b) is axially displaced by 1.51μm and image (c) by 2.56μm in the same direction.

9.3.3 Surface Profilometry

In order to achieve interferometric phase imaging it was necessary to increase the injection current. We found a value of 69mA to be adequate although its exact value was not critical. This value also permitted us to superimpose a 200kHz modulation to provide the required phase modulation. We also found that an injection current modulation of 0.33mA led to $\Delta k \sim 2\mathrm{x}10^{-5}\,\mu\mathrm{m}^{-1}$ which translates to a phase modulation $\phi_o = 2(\Delta k)l \approx 2\pi$. We used this level of injection current modulation since it produced a sufficiently high demodulated signal, $I_{2\omega}$. The other effect of injection current modulation is that the laser intensity is also modulated. For 0.33mA modulation we measured $\beta = 0.015$.

Fig. 72 shows the axial responses demodulated at 200kHz and 400kHz together with the theoretical predictions according to eqns (176) and (178). In order to obtain agreement in the 200kHz demodulated case it was necessary to allow r, to be a free parameter. A value of $r = 0.78$ was found to be satisfactory.

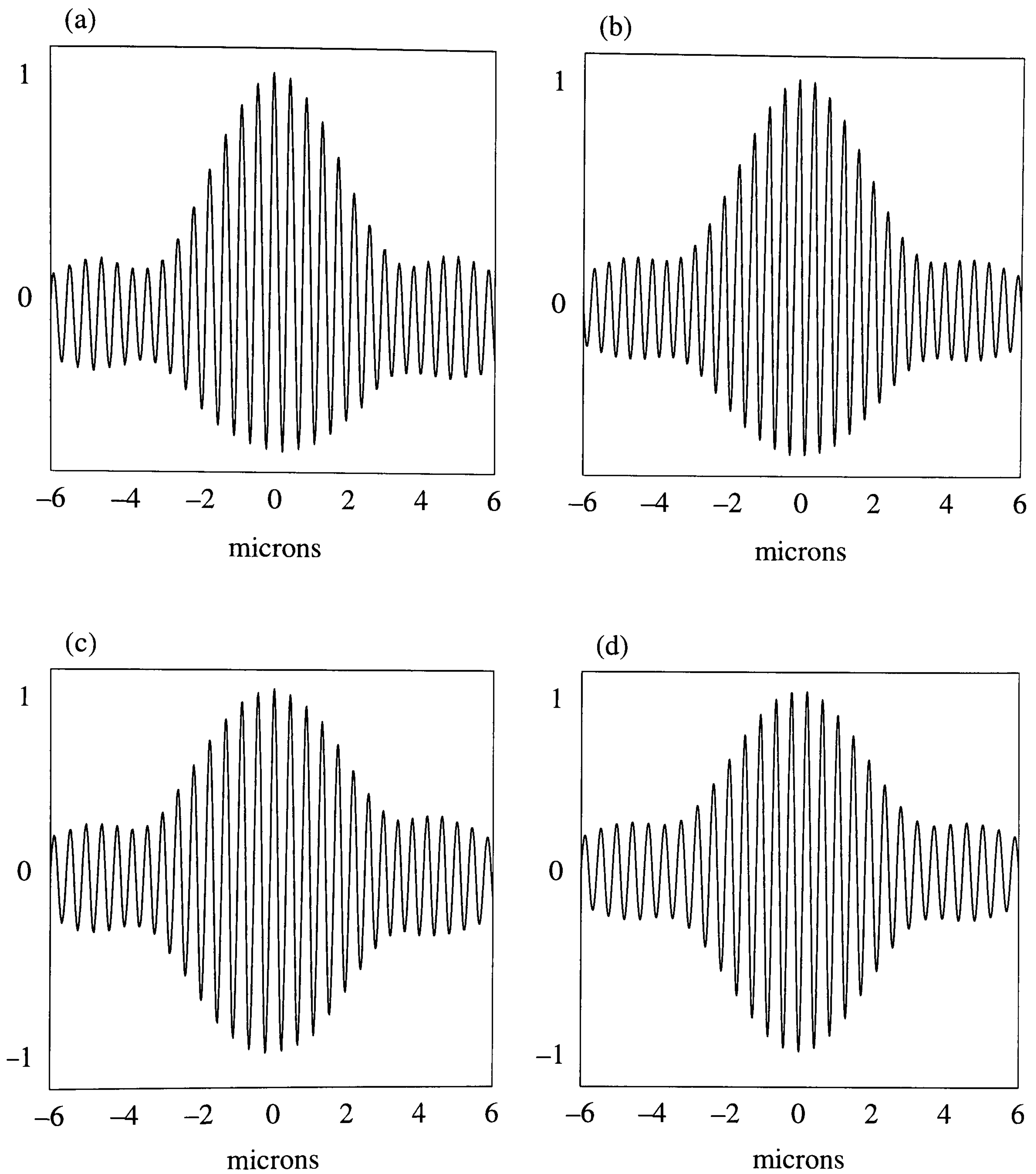

Fig. 72 The demodulated axial responses from the interference microscope, normalised such that $I(0) = 1.0$ and $a = 3.49$.

(a) and (b) are the experimental and theoretical curves for demodulation at 200kHz.

(c) and (d) are the experimental and theoretical results for demodulation at 400kHz.

In order to obtain the phase (height) image we used the 400kHz demodulated signal as an error signal in a simple proportional–plus–integral feedback loop. The feedback signal was finally applied to the injection current such that the overall action of the system was to add an extra phase, $\Delta\phi$, eqn (179), which reduced the demodulated term to zero. In this way the feedback signal represented the height profile and was available for surface profilometry, as illustrated schematically in Fig. 73.

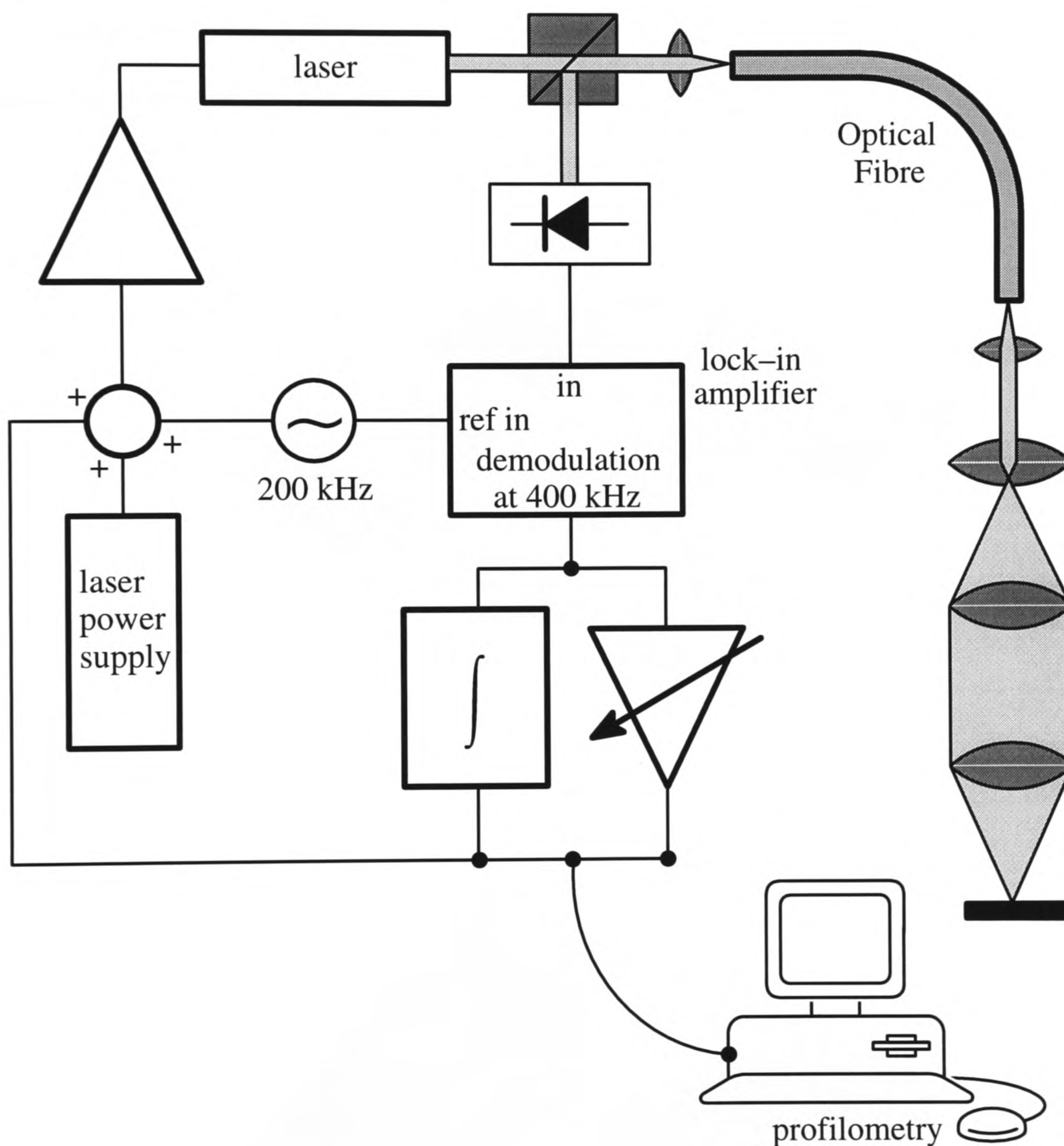

Fig. 73 A schematic diagram of the demodulation and feedback system.

We note that it is not possible to use the 200kHz demodulated signal as the error signal since the form of this signal depends on the object reflectivity and this will vary from picture

point to picture point. Thus introducing an extra phase term in a feedback to set I_ω equal to zero (in eqn (176)) will not, in general, produce a surface profile.

Fig. 74 and Fig. 75 show two examples of surface profiles obtained with this system. Fig. 74 shows a silicon test specimen (Agar Scientific S1934) containing a pattern formed by electron beam lithography. The lattice period is 10μm and the feature height is 186nm. Fig. 75, on the other hand, shows a 90μm square area of an etched aluminium pattern. The feature height is 12nm. These were the specimens which were used to obtain the experimental edge responses in Fig. 66 and Fig. 65, respectively, in Chapter 8.

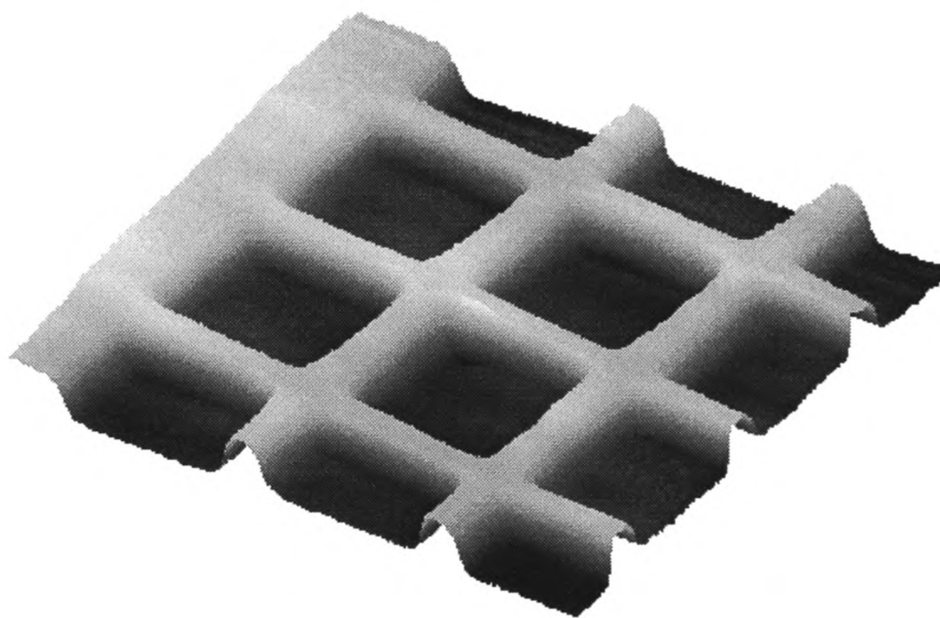

Fig. 74 The surface profile of a silicon test object. The lattice is 186nm high and has period 10μm.

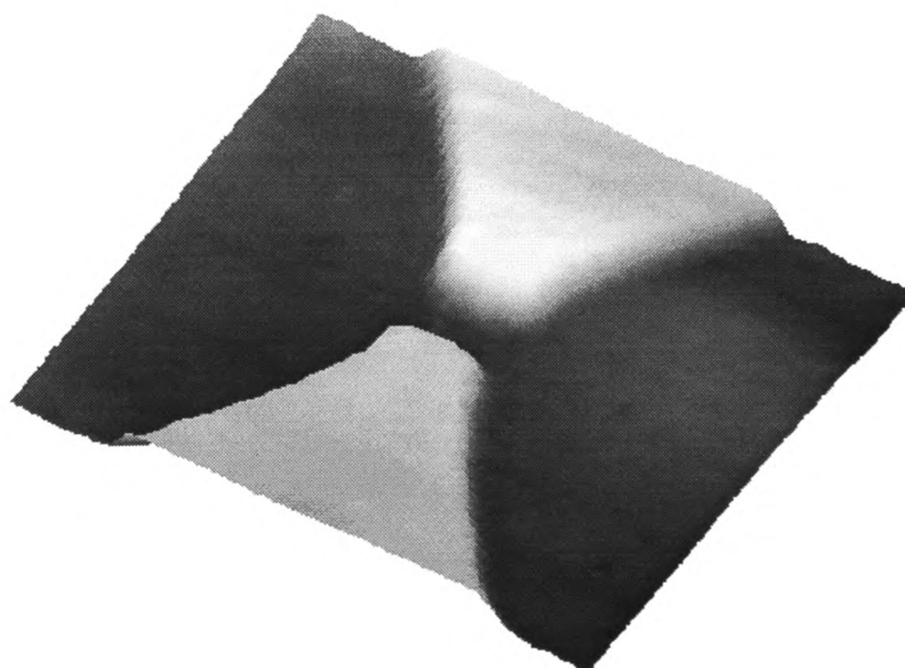

Fig. 75 The surface profile of a pattern in aluminium.
The pattern is 12nm high and the area shown is 90μm square.

9.4 Conclusions

In this chapter we have described a semiconductor laser based confocal scanning microscope which can image as a non–interference microscope when the injection current is low. On the other hand interference imaging results if the injection current is increased. A simple injection current modulation technique was introduced which permits the interference term image to be extracted from the full interference image. A feedback system was then introduced which allowed us to determine the argument (phase) of the confocal amplitude image. This phase image has been used to produce high resolution surface profiles. However care should be taken in interpreting the spatial resolution of phase images since the imaging process is necessarily non–linear as was shown in Chapter 8. This leads to apparent higher spatial resolutions at step heights near to $\lambda/4$.

We modelled the response of the microscope, and the modelled axial scans were seen to closely resemble the axial scans obtained experimentally. Finally we provided some images produced by this microscope. The series of images obtained by the confocal system clearly displayed the characteristic optical sectioning. The surface profiles obtained by the interference imaging correspond to images obtained by HeNe based microscopes described in Chapters 6 and 7, and illustrate the sensitivity of this technique to surface features with height in the order of nm.

10. Conclusions and Suggested Further Research

The confocal scanning optical microscope is a relatively recent arrival into the family of high resolution imaging techniques. In Chapter 1 it was shown that the first compound microscope was constructed in Holland some 400 years ago, about 300 years after the first eye–glasses were invented. However, it was not until the advent of reliable, high intensity illumination sources and affordable computers capable of image processing that the confocal microscope was developed into the popular, versatile instrument it is today, with an estimated annual market of $80 million.

We saw that this popularity stems principally from its optical sectioning property which ensures that confocal images only contain object detail from within the plane of focus. Also confocal imaging suffers less from scattered light in the optical system and is particularly suitable for image processing, since the image is obtained directly in serial, digital form.

In this thesis a variety of novel optical systems have been described, which are capable of confocal or interference imaging, or both. In Chapter 2 we outlined the basic optical theory required to describe the various optical systems considered in the rest of this thesis. Because many of these systems involved optical feedback into the cavity of the illuminating laser we developed suitable theories to describe the effect of this on the lasing action of both HeNe and semiconductor lasers in Chapter 3.

In Chapter 4 we showed that it is possible to significantly reduce the number of major optical components required in a reflection confocal microscope when a semiconductor laser is used as the source of illumination. The first significant innovation was the introduction of optical feedback into the laser in which the signal reflected from the object was permitted to re–enter the laser cavity. This removed the need for the beamsplitter required to divert some of the signal towards a photodetector. The linear relationship between the signal reflected from the object and the variation of the optical intensity within the semiconductor laser cavity was established by using a photodetector to monitor the optical intensity

emitted from the other laser port. We explained this theoretically and obtained confocal images which demonstrated the viability of such an imaging system.

The need for the photodetector was removed when the junction voltage across the semiconductor laser cavity was monitored and found to give comparable results. To explain these results we modelled the effect of the optical feedback on the optical field amplitude within the laser cavity and on the junction voltage. Again, we obtained confocal images which confirmed the practical capability of the system.

Further, it was shown that the optical fibre, which was originally used as a coherent detector/source in the system, could be discarded. We demonstrated that the laser mode itself could perform the same function of spatial filtering. In this way the optical arrangement became even more simple and compact.

As well as making the system more compact, such changes also simplify the design of the microscope significantly and make alignment much easier. The system also becomes more robust and easier to maintain and operate.

The confocal nature of these microscopes was established by using them to image a plane reflector while it was scanned axially. Though this was seen to be confocal, in so far as optical sectioning was demonstrated, one notable difference from the traditional axial scan was observed. It was shown that the axial response of the feedback systems was the square root of the traditional axial response. This was explained in terms of the coherent detection which resulted from the use of a laser or optical fibre as the detector.

When the semiconductor laser was replaced by a HeNe laser the results were found to be quite different. The frequency of the laser was relatively unperturbed by the signal re–entering the cavity and the result was an interference type signal with the confocal axial response superimposed. It was shown that the fringe pattern of the interference signal could be used in a variety of ways. In the simplest system a confocal interference image was obtained. However the system became more versatile when feedback was introduced to con-

trol the optical path length of the system, and it then became possible to achieve surface profilometry. We implemented a system in which the electronic feedback signal could control the phase of the wave reflected from the specimen by means of an electro–optic phase modulator. The control signal was directly related to the variation in the intensity of the signal detected from the other port of the laser. However this system was susceptible to laser noise and could not give a confocal signal.

An improved system was then devised in which a simple phase modulation technique permitted the interference term to be extracted from the full interference image. This interference term was then used to produce high resolution surface profiles. The use of a lock–in amplifier made it possible to achieve confocal imaging simultaneously with the profilometry, as well as reducing the susceptibility of the system to noise.

Although the final (modulation feedback) system was capable of real–time imaging and achieved high resolutions (of order nm) it suffered from a number of limitations. The first was the limited size of object feature which it could image adequately without needing to sacrifice resolution. As the features became steeper and higher it became significantly more difficult to keep the system response sufficiently fast that it remained locked on to them. Related to this was the difficulty of keeping the feedback system stable over a prolonged period, with a variety of specimens. Clearly, however, these limitations are electronic rather than optical in nature.

One further means of controlling the phase in a HeNe system, rather than using the electro–optic phase modulator, would be to mechanically control one of the cavity mirrors in the laser by mounting it on a piezo–electric stage. This would face many problems resulting from the stress which would be likely to be induced on the tube enclosing the cavity, probably requiring a customised cavity to be fabricated. It would also suffer from the limited speed of response possible with a mechanical system. However the distance over which it would need to scan would be very small and it would remove the need for a further optical element in the system and the problems of reflection and alignment which it brings.

To overcome the problems with the feedback control electronics a new system was devised which had the same profilometry capability but which did not require an electronic feedback system. However, to achieve this it sacrificed a true real–time imaging capability, since the image had to be calculated from the raw data. For this system to work it was important that the longitudinal cavity modes of the laser remained unperturbed and it was therefore necessary to minimize the signal which could re–enter the laser. We therefore had to re–introduce an optical fibre into the system to provide a reflection point for the reference beam which could interfere with the signal reflected from the object. However it was capable of producing both confocal images and surface profiles and was much simpler to operate than the earlier system.

The issue of the resolution achievable by these microscope systems is considered in Chapter 8. In particular, lateral resolution was considered in detail and shown to be intrinsically non–linear. As a result, specimens with vertical feature size of about a quarter of the wavelength of the laser being used are resolved much better than features of other heights.

Finally, an interference system was developed which used a semiconductor laser as the source of illumination. When a semiconductor laser was used earlier the level of feedback into the cavity was always sufficient for the internal laser dynamics to cancel out the phase information in the reflected signal. To achieve interferometry, therefore, the signal which re–entered the laser cavity was minimized and a separate detector used once again. Also the laser had to be operated within a limited range of injection current to enable interference to be observed. It was therefore necessary to re–introduce an optical fibre into the system once more, to provide a reflection point for the reference signal. To achieve profilometry, an electronic feedback control system similar to the one mentioned earlier, was used again. However this time a special property of semiconductor lasers was exploited, namely the variation of wavelength with injection current. This removed the need for a bulky, high voltage electro–optic element in the system and also increased the speed with which the system could respond to height variations, due to the high bandwidth of the laser response.

As well as the profilometry it was of course possible to obtain confocal images by either increasing the intensity of the reflected signal which could re–enter the laser cavity or adjusting the operating injection current of the laser out of the range which supported interferometry. For the results shown in this thesis the latter technique was used.

The main difficulty with this system is the requirement to reduce the intensity of the signal which can re–enter the laser cavity to such a level that it does not perturb the mode structure of the laser. However it was clearly the most versatile which was developed in the course of this research. It could take confocal images or surface profiles depending on which was most appropriate to the size of the specimen features, unlike the other systems in which the confocal images were generally by–products of the profilometry and could therefore not be obtained if the feature size was too large to permit profilometry.

The development of such a compact system opens up a number of other possibilities for further research. To make the microscope easier to use it might be possible to transfer the lateral scanning from the mechanical stage on which the specimen is held to the tip of the fibre. This would make it possible to construct a self–contained probe which could be moved from one point to another on a larger specimen. This probe would be connected to the electronics and laser by the optical fibre. It would, naturally, be necessary to ensure that the probe could be firmly attached to the specimen or the surface on which the specimen was held before scanning could begin.

Continuing earlier research, it should be possible to implement the system which did not require the feedback control loop, using a semiconductor laser instead of the HeNe laser, thus enabling a more compact system to be built. Also, it could well be valuable to investigate further the operational limitations of the semiconductor laser in interferometry to establish exactly how much optical feedback can be permitted into the laser cavity before the internal cavity modes are too perturbed. If by choosing the type of semiconductor laser carefully and selecting an optimum injection current it is possible to have a small though appreciable reflected signal admitted into the laser cavity it might be possible to combine

the junction voltage technique and the profilometry already described. This would result in a remarkably compact optical microscope which would be capable of imaging objects with vertical feature sizes as large as microns or as small as nanometres!

Appendix 1
Introduction to Fresnel Diffraction

Diffraction was defined by Sommerfeld in 1954 as 'any deviation of light rays from rectilinear paths which cannot be interpreted as reflection or refraction', but attempts to explain the phenomenon were first made over 250 years earlier by Huygens, who was one of the earliest exponents of the wave theory of light. One of the results of this theory was the principle of secondary wavelets which stated that each point on the wavefront of a light disturbance could be considered to be a new source of a "secondary" spherical disturbance. Hence the wavefront at any later instant could be found by constructing the "envelope" of the secondary wavelets. This is expressed mathematically as the Fresnel–Kirchhoff Diffraction Formula [16].

$$U(P_1) = \frac{A}{j\lambda}\int_{\Sigma}\int \frac{e^{jk(\varrho + r)}}{r\varrho}\frac{\left(\cos(\underline{n},\underline{r}) - \cos(\underline{n},\underline{\varrho})\right)}{2}dS \qquad (181)$$

where $U(P_1)$ is the optical disturbance at a point P_1, A is the normalization constant for the spherical wave (originating at point P_1) assumed to illuminate the diffracting aperture (ie $U(P') = A\frac{e^{jk\varrho}}{\varrho}$) and ϱ and r are the distances of points P_0 and P_1 from the aperture respectively as shown in Fig. 76.

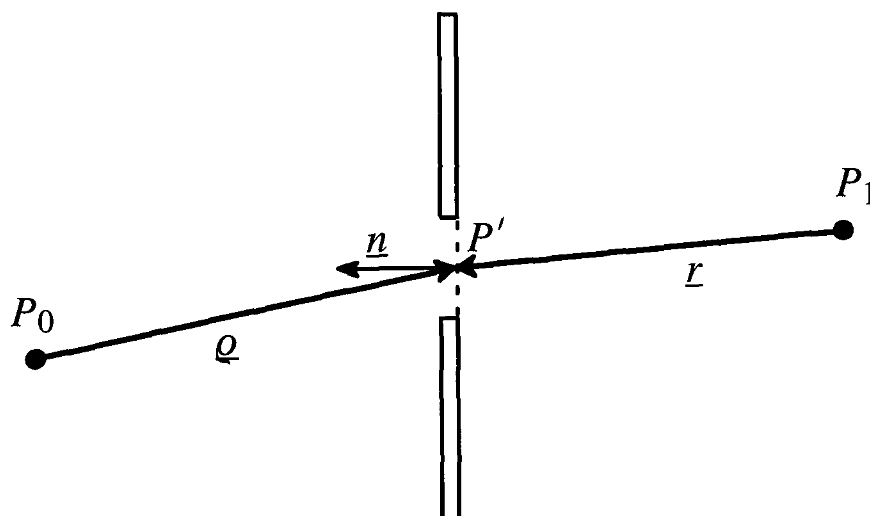

Fig. 76 Illustration of the terms used in the Fresnel–Kirchhoff Diffraction Formula.

λ is the wavelength of the illumination and the surface integral is over the area of the diffracting aperture consisting of points P'. Finally, the cosine factor is the mean of the cosines of the angles between the vector from a point in the aperture to P_0 and P_1 ($\underline{r}$ and $\underline{\varrho}$) and the normal to the aperture at that point ($\underline{n}$). This obliquity factor allows for the fact that $\underline{n}$ and $\underline{r}$ or $\underline{\varrho}$ are not always (or even usually) parallel. However in most cases the factor is roughly unity and can generally be ignored. It shows mathematically that the secondary sources do not radiate backwards. This formula has its origins in Scalar Diffraction Theory, where Greens's Theorem is applied to a Helmholtz equation and boundary conditions (from either Kirchhoff or Sommerfeld) applied to the resulting Kirchhoff Integral [16].

Rather than confine ourselves to incident spherical waves we can generalise to other waves by replacing the $A\frac{e^{jk\varrho}}{\varrho}$ factor by $u(x,y)$. The $1/r$ factor can be replaced by $1/d$, where d is the perpendicular distance from the aperture to P_1, though clearly a similar substitution cannot be made in the exponent since the errors will be multiplied by many k, giving an error of even greater than 2π in the phase! This leaves us with

$$U(P_1) = \frac{A}{j\lambda d}\iint_{\Sigma} u(x,y)\ e^{-jkr}\ \mathrm{dS} \tag{182}$$

For this integral to be evaluated, it is necessary to approximate the value of r in whichever co–ordinate system is being used.

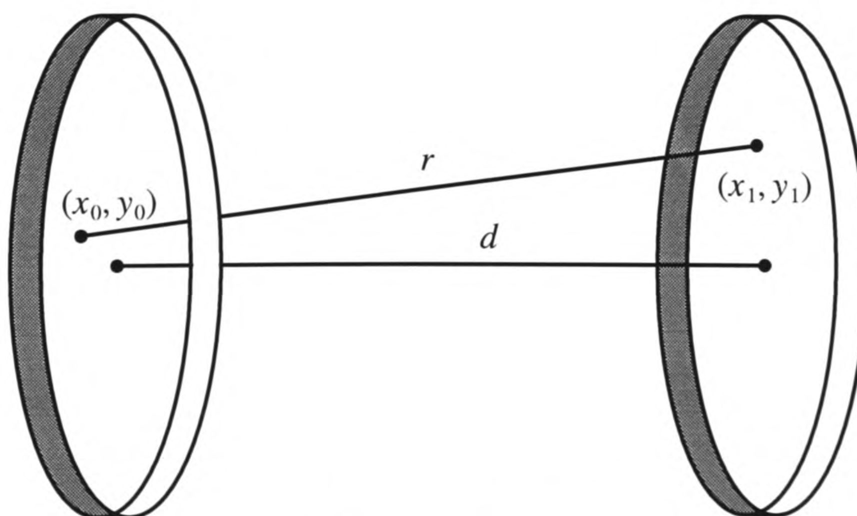

Fig. 77 The description of 2 points, (x_0,y_0) and (x_1,y_1), distance r apart, in planes separated by distance d.

From Fig. 77 it can be seen, using Pythagoras's Theorem and the binomial expansion, that

$$r = \left\{d^2 + \left(x_0 - x_1\right)^2 + \left(y_0 - y_1\right)^2\right\}^{1/2} \tag{183}$$

$$r \approx d\left\{1 + \frac{1}{2}\left(\frac{x_0 - x_1}{d}\right)^2 + \frac{1}{2}\left(\frac{y_0 - y_1}{d}\right)^2\right\} \tag{184}$$

This 'Fresnel Approximation' is valid if d is sufficiently larger than $(x_0 - x_1)$ and $(y_0 - y_1)$. In this case $\exp(-jkr)$ becomes

$$\exp(-jkd)\ \exp\left(-\frac{jk}{2d}\left\{\left(x_0 - x_1\right)^2 + \left(y_0 - y_1\right)^2\right\}\right) \tag{185}$$

Hence equation (182) can be rewritten as

$$U(P_1) = U(x_1, y_1) = \frac{e^{-jkd}}{j\lambda d}\ e^{-\frac{jk}{2d}\left\{x_1^2 + y_1^2\right\}} \int\int_{\Sigma} u(x_0, y_0)\ e^{-\frac{jk}{2d}\left\{x_0^2 + y_0^2\right\}}\ e^{\frac{jk}{d}\left\{x_0 x_1 + y_0 y_1\right\}}\ \mathrm{d}x_0 \mathrm{d}y_0 \tag{186}$$

From this it is clear that $U(x_1,y_1)$ may be found from a Fourier Transform of $u(x_0, y_0)\ e^{\frac{jk}{2d}\left\{x_0^2 + y_0^2\right\}}$, where the transform must be evaluated at frequencies $f_x = \frac{x_0}{\lambda z}$ and $f_y = \frac{y_0}{\lambda z}$ to ensure correct scaling.

Appendix 2
The Modelling of Lenses

A lens is said to be 'thin' if a ray entering at coordinates (x,y) on one face emerges at approximately the same coordinates on the opposite face, ie if there is negligible translation of the ray within the lens. Thus a thin lens delays an incident wavefront by an amount proportional to the thickness of the lens at each point. This thickness can be calculated as follows.

Consider a ray passing through the top half of a lens of constant refractive index (n) throughout its volume and whose 2 surfaces have radii of curvature r_1 and r_2 as shown in Fig. 78.

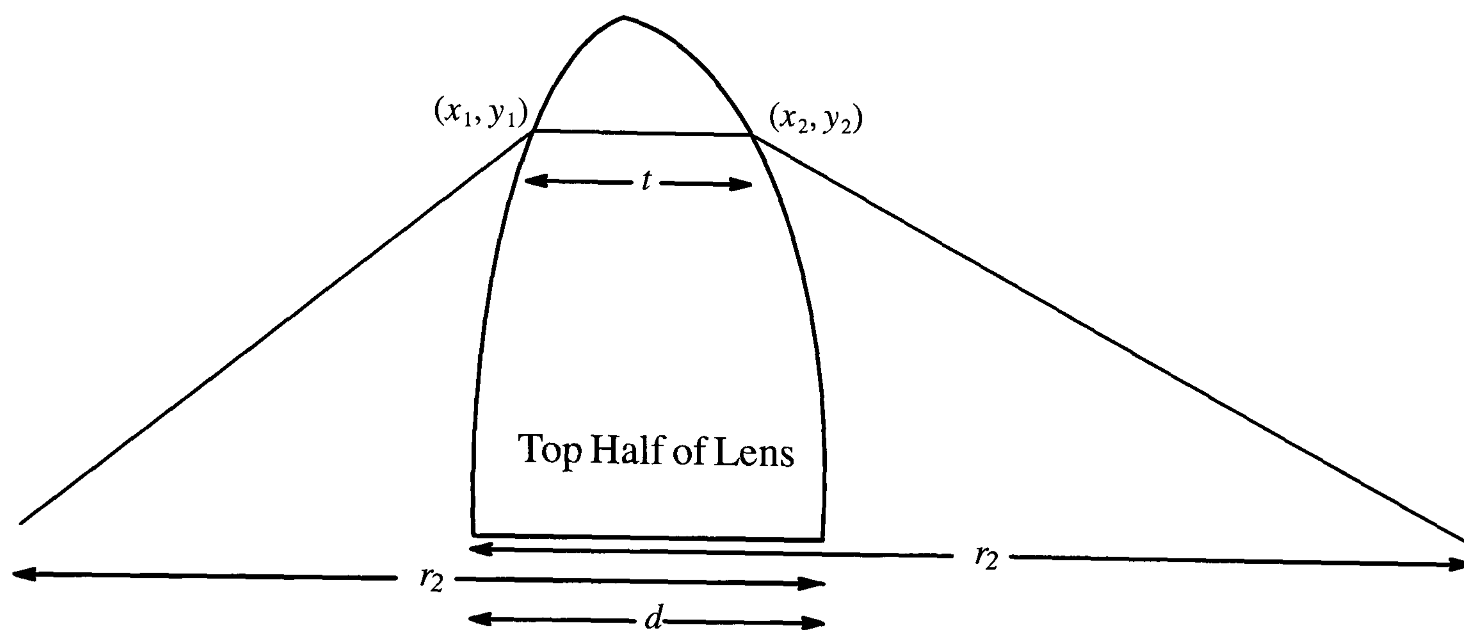

Fig. 78 Illustration of the different parameters used to model a lens.

If we assume that (x_1,y_1) and (x_2,y_2) are very close we can express t in terms of x and y, as below

$$t = \sqrt{r_1 - x_1^2 - y_1^2} - r_1 + \sqrt{r_2 - x_2^2 - y_2^2} - r_2 + d \tag{187}$$

$$= d - r_1\left\{1 - \sqrt{1 - \frac{x_1^2 + y_1^2}{r_1^2}}\right\} - r_2\left\{1 - \sqrt{1 - \frac{x_2^2 + y_2^2}{r_2^2}}\right\} \tag{188}$$

If we approximate the spherical surfaces of the lens by parabolic surfaces (the Paraxial Approximation), which is mathematically achieved by using the Binomial Approximation to the first order on the square root terms, we obtain the following expression for t.

$$t = d - \frac{x_1^2 + y_1^2}{2r_1} - \frac{x_2^2 + y_2^2}{2r_2} \tag{189}$$

Since our lens is thin, we can set $x_1, x_2 \approx x$ and $y_1, y_2 \approx y$ which simplifies eqn (189) to

$$t = d - \frac{x^2 + y^2}{2}\left(\frac{1}{r_1} + \frac{1}{r_2}\right) \tag{190}$$

Now that we have an expression for the thickness of a bi–convex lens we can calculate the total phase delay suffered by a ray passing through the lens (of maximum width d) at point (x,y).

$$\Delta\phi(x,y) = nkt(x,y) + k\left(d - t(x,y)\right) = kd + (n - 1)kt(x,y) \tag{191}$$

Substituting for t from eqn (190) gives

$$\Delta\phi(x,y) = kd + (n\text{–}1)kd - (n\text{–}1)k\frac{x^2 + y^2}{2}\left(\frac{1}{r_1} + \frac{1}{r_2}\right) \tag{192}$$

$$\Delta\phi(x,y) = nkd - \frac{k}{2f}\left(x^2 + y^2\right) \qquad \text{where } \frac{1}{f} = (n\text{–}1)\left(\frac{1}{r_1} + \frac{1}{r_2}\right) \tag{193}$$

Hence the lens has the effect of multiplying the amplitude by a factor $\tau(x,y)$, where $\tau(x,y)$ is

$$\tau(x,y) = \exp - jnkd \;\; \exp \frac{jk}{2f}\left(x^2 + y^2\right) \tag{194}$$

To complete our description of the action of a lens on a wavefront, we need to describe the diffraction effect of the aperture of the lens, and this we do either by limiting the area of integration in x, y for $\tau(x,y)$ or including a Pupil Function, $P(x,y)$, which is unity within the area of the lens and zero elsewhere. Hence a beam leaving the back of a lens U_b can now be described in terms of the beam entering the front of the lens U_f as follows.

$$U_b(x,y) = P(x,y)\;\tau(x,y)\;U_f(x,y) = P(x,y)\;\exp\frac{jk}{2f}\left(x^2 + y^2\right)\;U_f(x,y) \tag{195}$$

where we neglect the $\exp(-jnkd)$ term from $\tau(x,y)$ since it is constant for all x, y.

Appendix 3
Differential Amplifier with Offset

This circuit was used to measure the junction voltage as described in Chapter 5.

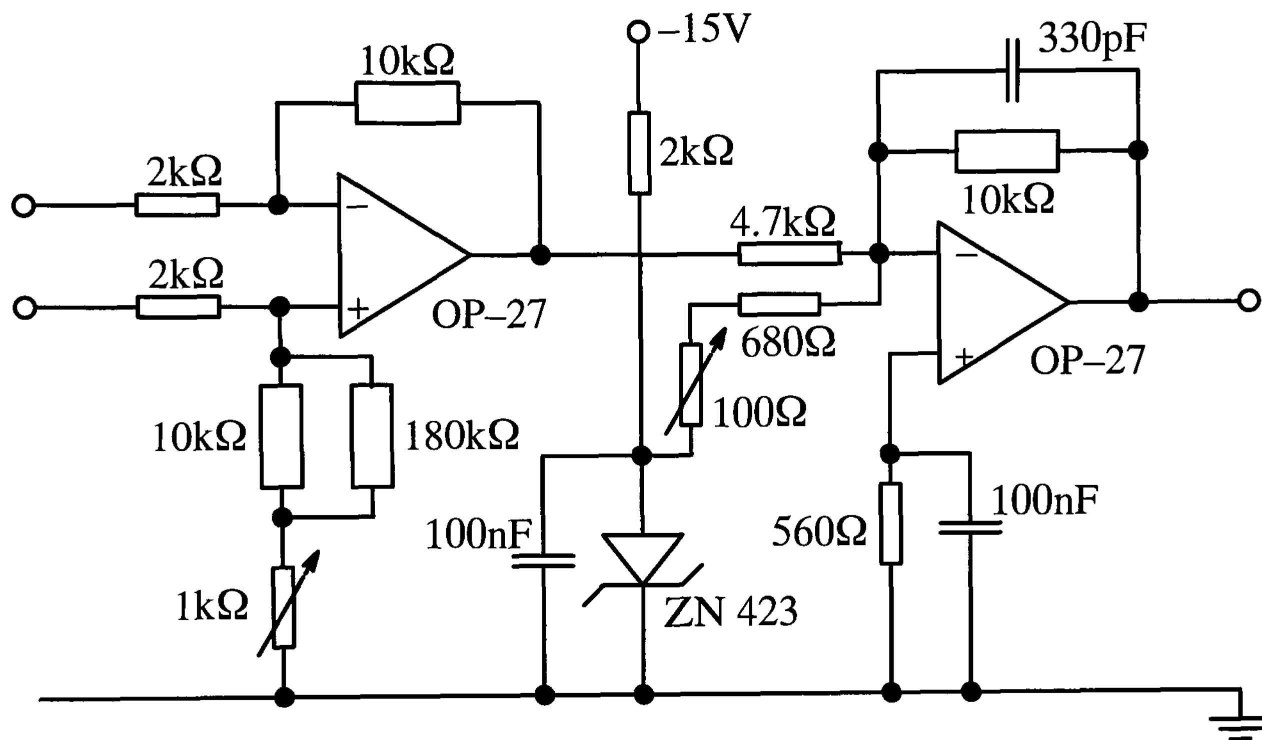

Appendix 4

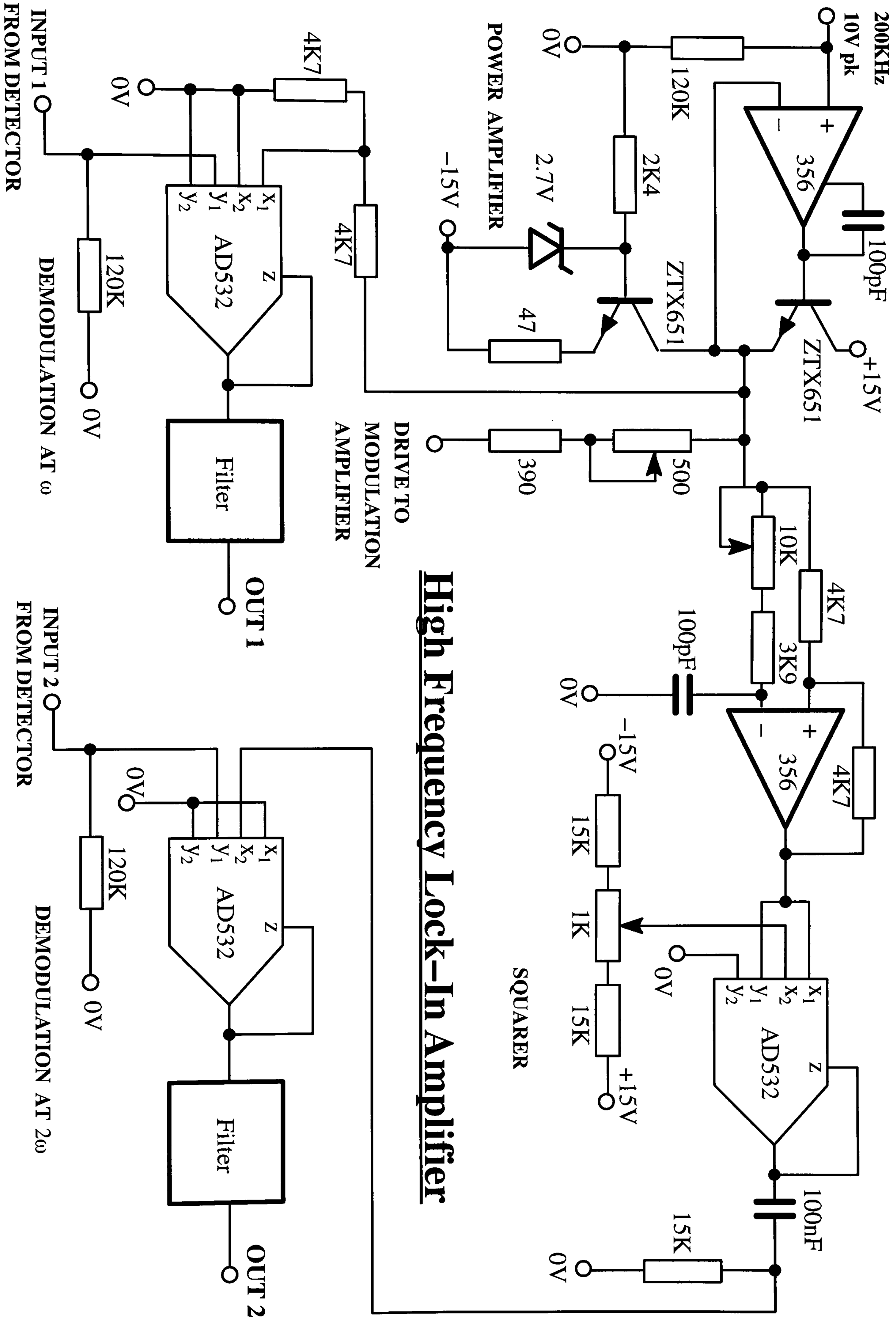

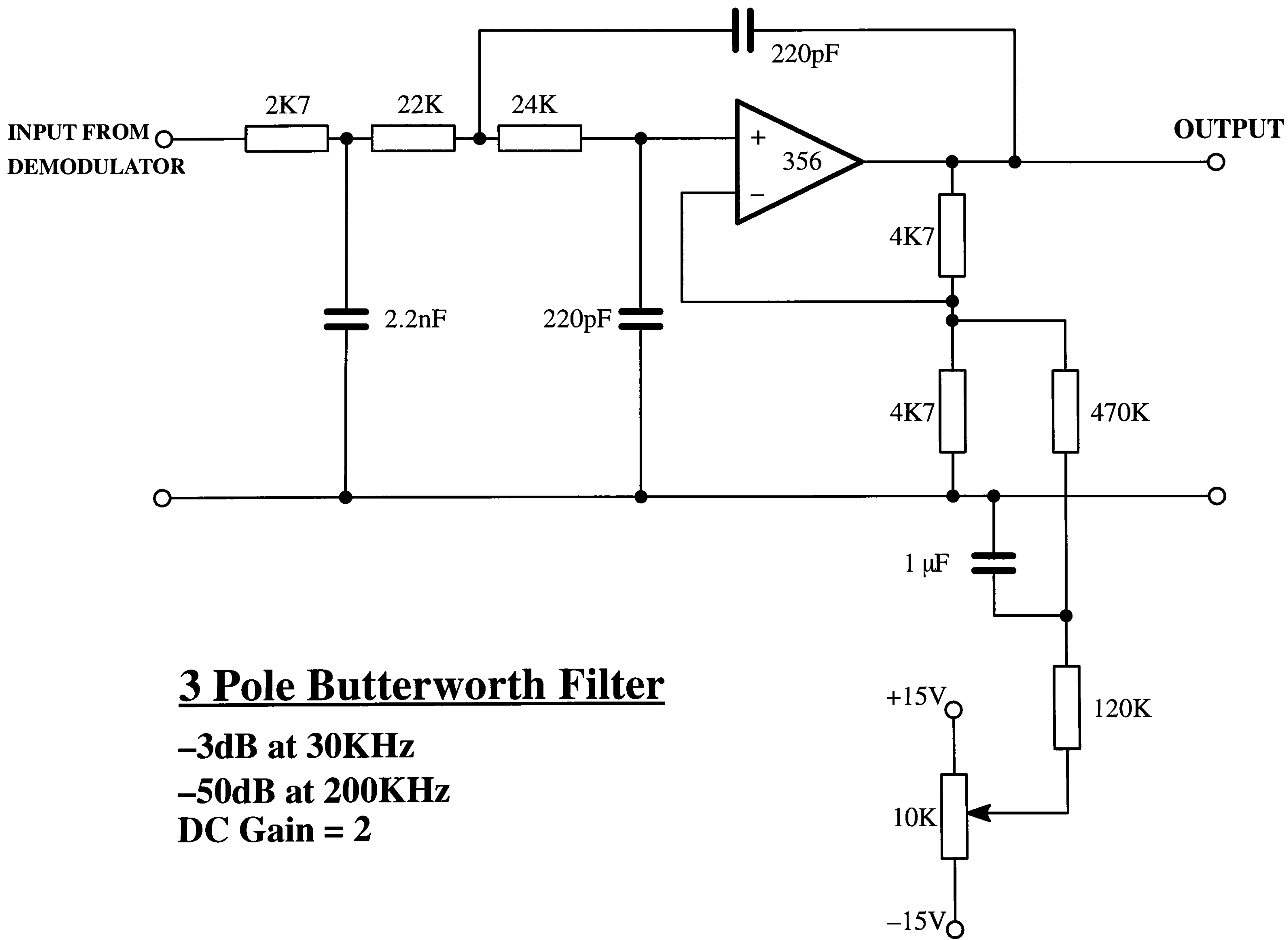
INPUT FROM
DEMODULATOR
2K7
22K
24K
220pF
2.2nF
220pF
+
356
−
4K7
4K7
470K
OUTPUT
1 µF
120K
+15V
10K
−15V
3 Pole Butterworth Filter
−3dB at 30KHz
−50dB at 200KHz
DC Gain = 2

References

1. C Singer (Ed), *Studies in the History and Method of Science*, vol 2 (Oxford University Press, 1921).

2. E Rosen, "The Invention of Eyeglasses", *Journal of the History of Medicine and Allied Sciences*, 1956.

3. J Z Young and F Roberts, "A Flying–Spot Microscope", *Nature*, vol 167, p 231, 1951.

4. E M Deeley, "An integrating microdensitometer for biological studies", *J Scient Instrum*, vol 32, pp 263–267, 1955.

5. M Minsky, U S Patent 3013467, *Microscopy Apparatus,* 19 Dec, 1961 (Filed 7 Nov, 1957).

6. A L Schawlow and C H Townes, "Infrared and Optical Masers", *Phys Rev*, vol 112, pp 1940–1949, 1958.

7. W Lukosz, "Optical systems with resolving powers exceeding the classical limit", *J Opt Soc Am*, vol 56, pp 1463–1472, 1966.

8. T Wilson (Ed), *Confocal microscopy*, (Academic Press, London, 1984).

9. T Wilson and C J R Sheppard, *Theory and Practice of Scanning Optical Microscopy*, (Academic Press, London, 1984).

10. S Kimura and T Wilson, "Confocal scanning optical microscopes using single mode fibre for signal detection", *App Opt*, vol 30, pp 2143–2150, 1991.

11. L Giniunas, R Juškaitis and S V Shatalin, "Scanning fibre–optic microscope", *Electron Lett*, vol 27, pp 724–726, 1991.

12. R Juškaitis and T Wilson, "Imaging in reciprocal fibre–optic based confocal scanning microscopes", *Optics Commun*, vol 92, pp 315–325, 1992.

13. R Juškaitis, F Reinholz and T Wilson, "Fibre–optic based confocal scanning microscopy with semiconductor laser excitation and detection", *Electron Lett*, vol 28, pp 986–987, 1992.

14. R Juškaitis, T Wilson and F Reinholz, "Spatial filtering by laser detection in confocal microscopy", *Optics Lett*, vol 18, pp 1135–1137, 1993.

15. C J Sheppard and T Wilson, "Effects of high angles of convergence on $V(z)$ in the scanning acoustic microscope", *App Phys Lett*, vol 38, pp 858–859, 1981.

16. J W Goodman, *Introduction to Fourier Optics*, (McGraw Hill, San Francisco, 1968).

17. R Lang and K Kobayashi, "External optical feedback effects on semiconductor injection laser properties", *IEEE J Quantum Electron,* vol 16, pp 347–355, 1980.

18. Charles H Henry, "Theory of the Linewidth of Semiconductor Lasers", *IEEE J Quantum Electron,* vol 18, pp 259–264, 1982.

19. Marek Osinski and Jens Buus, "Linewidth Broadening Factor in Semiconductor Lasers – An Overview", *IEEE J Quantum Electron,* vol 23, pp 9–29, 1987.

20. Joachim Sacher, Dieter Baums, Peter Panknin, Wolfgang Elsässer and Ernst O Göbel, "Intensity instabilities of semiconductor lasers under current modulation, external light injection, and delayed feedback", *Phys Rev A,* vol 45, pp 1893–1905, 1992.

21. K Petermann, *Laser Diode Modulation and Noise*, (Kluver Academic, Dordrecht, The Netherlands), 1988.

22. D Lenstra, M van Vaalen and B Jaskorzynska, "On the theory of a single–mode laser with weak optical feedback", *Physica*, vol 125C, pp 255–264, 1984.

23. G A Acket, D Lenstra, A J van Boef and B H Verbeek, "The influence of feedback intensity on longitudinal mode properties and optical noise in index–guided semiconductor lasers", *IEEE J Quantum Electron,* vol 20, pp 1163–1169, 1984.

24. N Schunk and K Petermann, "Numerical Analysis of the Feedback Regimes for a Single–Mode Semiconductor Laser with External Feedback", *IEEE J Quantum Electron,* vol 24, pp 1242–1247, 1988.

25. J Mørk, B Tromborg and J Mark, "Chaos in semiconductor lasers with optical feedback: theory and experiment", *IEEE J Quantum Electron,* vol 28, pp 93–108, 1992.

26. B Tromborg, J H Osmundsen, H Olesen, "Stability Analysis for a Semiconductor Laser in an External Cavity", *IEEE J Quantum Electron,* vol 20, pp 1023–1032, 1984.

27. H Oleson, J H Osmundsen, B Tromborg, "Nonlinear Dynamics and Spectral Behavior for an External Cavity Laser", *IEEE J Quantum Electron,* vol 22, pp 762–773, 1986.

28. R W Tkach and A R Chraplyvy, "Regimes of feedback effects in 1.5μm distributed feedback lasers", *J Lightwave Techn*, vol LT–4, pp 1655–1661.

29. A E Siegman, *Lasers*, (University Science Books, Mill Valley, California), 1986.

30. W W Rigrod, "Saturation effects in high–gain lasers", *J Appl Phys,* vol 34, pp 2602–2609, 1963.

31. A Yariv, *Quantum Electronics*, (John Wiley, New York, 1988).

32. J Katz, S Margalit, C Harderer, D Wilt and A Yariv, "The intrinsic electrical equivalent circuit of a laser diode", *IEEE J Quantum Electron*, vol 17, pp 4–7, 1981.

33. R Juškaitis, A M Mamedov, V T Potapov and S V Shatalin, "Distributed interferometric fiber sensor system", *Opt Lett*, vol 17, pp 1623–1625, 1992.

34. W M Wang, W J O Boyle, K T V Grattan and A W Palmer, "Fiber–optic Doppler velocimeter that incorporates active optical feedback from a diode laser", *Opt Lett*, vol 17, pp 819–821, 1992.

35. T Wilson and R Juškaitis, "Scanning Interference Microscopy", *Bioimaging*, vol 2, pp 36–40, 1994.

36. C J R Sheppard and T Wilson, "Fourier Imaging of phase information in scanning and conventional optical microscopes", *Phil Trans Roy Soc (Lond),* vol 295, pp 513–536, 1980.

37. G J Brakenhoff, "Imaging modes in confocal scanning light microscopy (CSLM)", *J Microscopy* vol 117, pp 233–242 , 1979.

38. A J Pidduck, D J Robbins, I M Young, A G Cullis and A S R Martin, "The Formation of Dislocations and their *In–situ* Detection During Silicon Vapour Phase Epitaxy at Reduced Temperature", *Materials Science and Engineering*, vol B4, pp 417–422, 1989.

39. A J Pidduck, R Jackson, D J Robbins, W Y Leong and M Wheeler. "Optimising Hydrophilic Wafer Cleaning for Silicon Epitaxy", *Proc Electrochemical Soc*, vol 92–12, p 453, 1992.

40. M Abramowitz and I A Stegun, *Handbook of Mathematical Functions*, (Dover, 1965).

41. T Wilson, "Image formation in two–mode fibre based confocal microscopes", *J Opt Soc Am*, vol 10, pp 1535–1543, 1993.

42. R Juškaitis and T Wilson, "Scanning interference and confocal microscopy", *J Microscopy*, vol 176, Pt 3, pp 188–194, 1994.

43. S S C Chim and G S Kino "Phase measurements using the Mirau correlation microscope", *Appl Opt*, vol 30, pp 2197–2201, 1991.

44. A B Carlson, *Communication Systems*, (McGraw Hill, 1988).

45. R N Bracewell, *The Fourier transform and its applications*, (McGraw Hill, 1978).

46. VP Tychinski, "On super–resolution of phase objects", *Optics Commun*, vol 74, p 41, 1989.

47. M Totzeck and M A Krumbugel, "Lateral resolution in the near field and for field phase images of π–phaseshifting structures", *Optics Commun*, vol 112, pp 189–200, 1994.

48. T Wilson, R Juškaitis, N P Rea and D K Hamilton, "Fibre optic interference and confocal microscopy", *Optics Commun*, vol 110, pp 1–6, 1994.

49. A Bearden, M P O'Neill, L Osborne and T L Wang, "Imaging and vibrational analysis with laser feedback interferometry", *Opt Lett*, vol 18, pp 238–240, 1993.

50. R Juškaitis, T Wilson and N P Rea, "Compact confocal interference microscopy", *Optics Commun*, vol 109, pp 167–177, 1994.

51. K Tatsuno and Y Tsunoda, "Diode laser direct modulation heterodyne interferometer", *Applied Optics*, vol 26, pp 37–40, 1987.

Publications Resulting From This Research

Fibre–Optic Based Confocal Microscopy Using Laser Detection

Optics Communications, Vol 99, pp 105–113, 1993

with R Juškaitis and T Wilson

Semiconductor Laser Confocal Microscopy

Applied Optics, Vol 33, pp 578–584, 1993

with R Juškaitis and T Wilson

Compact Confocal Interference Microscopy

Optics Communications, Vol 99, pp 105–113, 1993

with T Wilson and R Juškaitis

Fibre–Optic Interference and Confocal Microscopy

Optics Communications, Vol 110, pp 1–6, 1994

with T Wilson, R Juškaitis and D K Hamilton

Confocal Microscopy via Laser Feedback

Paper to Annual Meeting of Optical Society of America, Dallas, Texas, 1994

Semiconductor Interference and Confocal Microscopy

Optics Communications, (in press)

with T Wilson and R Juškaitis